Dissertation

submitted to the

Combined Faculties of the Natural Sciences and Mathematics

of the Ruperto-Carola-University of Heidelberg. Germany

for the degree of

Doctor of Natural Sciences

Put forward by

Ervin Kafexhiu

born in: Elbasan, Albania

Oral examination: July 3, 2013

Radiation signatures of nuclear reactions in very hot astrophysical plasmas

Referees: Prof. Felix Aharonian
Prof. Stefan Wagner

Abstract

The importance of nuclear reactions in low-density astrophysical plasmas with ion temperatures $k_BT \geq 1$ MeV has been recognized for more than thirty years. However, the lack of comprehensive data banks of relevant nuclear reactions and the limited computational power did not allow detailed theoretical studies. In this thesis, using the publicly available code TALYS, I have built a large nuclear reaction network relevant for temperatures exceeding 1 MeV. It contains about 270 nuclear species and include the calculation of γ-ray emissivity due to different nuclear reactions. The π-mesons production are also included. An approach to calculate the γ-ray spectra through $p + p \rightarrow \pi^0$ channel for an arbitrary proton distribution is also proposed.

The nuclear network is applied to two-temperature accretion disk models the so-called Advection Dominated Accretion Flows (ADAF) and Shapiro-Lightman-Eardly (SLE). The γ-rays emissivity are calculated for a wide parameter space including initial chemical composition. For a $10\,M_\odot$ black hole, both models can produce nuclear γ-ray lines luminosities as large as $L_N \sim 10^{34}$ erg s^{-1}. SLE is not an effective source of π^0 photons, whereas ADAF luminosity can be as large as $L_\pi \sim 10^{35}$ erg s^{-1}. ADAF regime is hot enough to evaporate neutrons. They can reach the companion star atmosphere and initiate secondary nuclear reactions.

Zusammenfassung

Die Bedeutung der Kernreaktionen in astrophysikalischen Plasmen mit geringer Dichte und hohen Ionentemperaturen von $k_BT \geq 1$ MeV ist schon seit mehr als 30 Jahren bekannt. Das Fehlen umfassender Datenbanken für die entsprechenden Kernreaktionen und eingeschränkte Rechenleistungen haben jedoch bisher keine detaillierten, theoretischen Untersuchungen erlaubt. Um dieses zu beheben, habe ich In dieser Arbeit unter Verwendung des öffentlich–zugänglichen Computercodes TALYS ein grosses Netzwerk an Kernreaktionen für den Temperaturbereich oberhalb 1 MeV aufgebaut. Das Netzwerk enthält 270 Kernarten und beinhaltet die Berechnung der Gammastrahlen-Emissivität für verschiedene Kernreaktionen. Die Erzeugung von π-Mesonen ist dabei ebenfalls berücksichtigt. Eine Verfahren zur Berechnung der Gammastrahlenspektren durch $p + p \rightarrow \pi^0$ Reaktionen für eine beliebige Protonenverteilung wird aufgezeigt.

Das nukleare Netzwerk wird auf bekannte Zwei– Temperaturen– Akkretionsscheibenmodelle, das sogenannte "Advection Dominated Accretion Flows" (ADAF) und das "Shapiro– Lightman–Eardly" (SLE) Modell angewandt. Dabei wird die Gammastrahlen– Emissivität für einen grossen Parameterraum und verschiedene chemische Anfangskompositionen berechnet. Für ein schwarzes Loch der Masse $10\,M_\odot$, können sich in beiden Modellen nukleare Gammastrahlenlinien mit einer Leuchtkraft von bis zu $L_N \sim 10^{34}$erg s^{-1} ergeben. SLE Scheibenmodelle sind keine bedeutende Quellen von π^0-Zerfallsphotonen; in ADAF Scheiben hingegen kann diese Leuchtkraft bis zu $L_\pi \sim 10^{35}$ erg s^{-1} betragen. ADAF Scheiben sind dabei heiss genug, um Neutronen freizusetzen. Wenn diese die Atmosphäre eine Begleitsterns erreichen, können sie zusätzliche Kernreaktionen auslösen.

Contents

List of Figures

1 Introduction

The universe – as we nowadays know – started from a very hot and dense state. This was the first time when the matter of the universe encountered temperatures $k_B T > 1$ MeV and it was the first time when nuclear reactions played a role in the chemical evolution.

According to the standard Big-Bang Nucleosynthesis (or the BBN) – which is the subject of physical cosmology that deals with the primordial abundances of elements – the light elements such as Deuterium (D), ^{3}He, ^{4}He, ^{6}Li and ^{7}Li, are synthesized during the first three minutes after the Big-Bang. The further expansion of the universe cooled the primordial plasma down and lowered its density; hence, all nuclear reactions have been frozen out. All other heavy elements are produced much later in the interior of stars (Bethe, 1939; Alpher et al., 1948; Burbidge et al., 1957)

The BBN has been successful in predicting the primordial abundances of D, ^{3}He and ^{4}He. These abundances match with the composition of very old metal-poor stars – which are believed to contain the primordial composition of elements. These observations have served to validate the standard cosmological model (see e.g. the Particle Data Group review). Despite this success, the BBN fails to predict the observed ^{6}Li and ^{7}Li abundances. This is the so-called "the Lithium problem" (see e.g. Fields, 2011). Lithium abundance may not be the only issue for the BBN because recent observations in some metal-poor stars have revealed traces of beryllium and boron which could have existed in the primordial plasma (see e.g. Primas, 2010).

In a hot plasma, the collisions of nuclei can either excite them due to inelastic processes or produce secondary nuclei in an exited state (due to nuclear reactions). Generally, nuclear interactions in a very hot plasma are accompanied by nuclear de-excitation lines. The observation of the Doppler broadened γ-ray lines would provide evidences for the nuclear reactions. In order to be detected, the γ-rays must be able to escape the production region, i.e plasma must be optically thin (transparent) for γ-rays.

The primordial plasma during the BBN was opaque, thus, it was not possible for γ-rays to move freely; the only direct information we have about the primordial nuclear reactions are the abundances of light elements.

A natural question arises: is any place in the sky where we can detect γ-ray lines and observe nuclear reactions in action? In principle low-density optically thin, hot plasmas with ion temperature exceeding 1 MeV can form near compact relativistic objects, such as accretion flows close to black holes (see e.g. Shapiro et al., 1976; Narayan and Yi, 1994; Blandford and Begelman, 1999) and in strong shock waves related, for example, to supernova explosions (see e.g. Colgate, 1975).

The most straightforward approach to study the dynamics of formation and evolution of such plasmas, is the detection of prompt γ-ray lines – product of nuclear reactions. The reason is that prompt γ-ray lines are unambiguous signatures of specific nuclei and their production rates are very sensitive to the conditions in plasma such as temperature and density. Hence, nuclear reactions can transform a given nuclei to another one giving rise to different γ-ray lines. The intensity and the width of the prompt γ-ray lines inform us about the plasma composition, temperature and density. Thus, it is of great practical importance to analyse and understand the MeV-γ-ray spectra from very hot plasma.

The evolution of chemical composition of plasma also carries information about the physical conditions. A very high temperature plasma experiences energetic collisions. They lead to destruction of heavy elements into lighter ones due to spallation reactions. If plasma lifetime is longer than the nuclear destruction time-scales then a proton–neutron (p–n) plasma is formed. The p–n plasma contains some traces of light elements which are a result of weak nucleosynthesis. If a very hot plasma has outflows, then it can spread its light elements into the surrounding and become “a contaminator”. These elements can then interact with the nuclei of the surrounding material. This will lead to secondary nuclear reactions and produce some characteristic nuclear γ-ray lines which can give us indirect clues on presence of very hot plasma.

The first attempts to assess the importance of nuclear processes in hot, thin astrophysical plasmas were made in Aharonian and Sunyaev (1984, 1987). Different astrophysical implications of nuclear reactions in hot two-temperature plasmas have been widely discussed in the literature (see e.g. Ramadurai and Rees, 1985; Gould, 1986; Vestrand, 1990; Jin, 1990; Guessoum and Kazanas, 1990; Harris and Share, 1991; Bildsten et al., 1992; Yi and Narayan, 1997; Guessoum et al., 1999; Jean and Guessoum, 2001; Guessoum and Jean, 2002; Belyanin and Derishev, 2001). These works provide estimates for the abundances of different light elements such as D, ^{6}Li, ^{7}Li, ^{9}Be, ^{11}B, etc.

The possibility that two temperature plasmas may modify the primordial (cosmological) abundances have also been discussed. Furthermore, they have estimated the γ-ray lines luminosity due to nuclear reactions.

Aharonian and Sunyaev (1984, 1987) have also suggested a mechanism for producing light elements, in particular deuterium, as an alternative to BBN. In very hot accretion flows, neutrons that are formed due to breakup reactions, can evaporate. If these neutrons manage to interact with a nearby cold surrounding material, they can be captured by hydrogen and form deuterium and a characteristic 2.22 MeV γ-ray capture spectrum.

These early works have formulated the basic theoretical description of a very hot plasmas. However the early calculations could include only a limited number of nuclei and reaction channels. The lack of data on nuclear cross-sections and the increased computational complexity of calculations as more nuclei are considered, were the main limitations. Most of these difficulties have nowadays been overcome. The introduction of on-line nuclear databases (*Evaluated Nuclear Data File (ENDF)*, n.d.; *Expermimental Nuclear Reaction Data (EXFOR/CSISRS)*, n.d.) provides easy access to experimental and theoretical data on nuclear cross-sections. There also exist publicly available computer codes which allow calculations of nuclear cross-sections and other quantities of interest. These make use of several theoretical models. Further advancements in computational power, makes it timely to conduct comprehensive studies of nuclear properties of very hot plasmas.

In this work I have developed numerical tools that allow us to perform detailed studies on the nuclear reactions and γ-ray spectra of a very hot plasma. In particular a large nuclear reaction network for temperatures $k_B T > 1$ MeV has been built. This nuclear network contains about 270 nuclear species and the most intense nuclear prompt γ-ray lines. This allows accurate treatment of the time evolution of the chemical composition and calculations of intensity of related γ-ray lines.

The π-meson production at proton-proton interaction has been also included in the nuclear network calculations. For a thermal plasma, accurate analytical fit formulas are provided for the π^0 production rate, cooling rate and γ-ray spectra. Calculations of γ-ray spectra due to π^0 production and decay have been performed also for non-fully thermalized plasmas.

The continuum radiation that come from the proton–nucleus nuclear bremsstrahlung and from capture reactions are also included. A general formula for capture reaction calculations is provided which it also considers the thermal Doppler broadening due to the thermal motion of the center of mass frame.

The nuclear network is applied to two accretion models, the Advection Dominated Accretion Flows (ADAF models) (see e.g. Narayan and Yi, 1994)

and to the Shapiro et al. (1976) model (SLE models). This has allowed detail studies of chemical composition evolution with the disk radius as well as calculation of the γ-ray emissivity spectra due to nuclear lines, continuum radiation and from the π^0 production. For a non-fully thermalized plasma, the calculation of the π^0 production γ-ray spectra it is also shown. Neutrons evaporation effect are included as well.

To conclude, this thesis provides a detailed study of the nuclear reactions in a very hot plasma, and discuss important applications for accretion flows.While theory and numerical studies – to which this thesis belongs – have made steps forward, sensitive MeV-γ-ray instruments are lagging behind. Hopefully this work can contribute to motivate further experimental studies.

Structure of the thesis

This thesis is constructed as follows:
CHAPTER 1 provides the introduction and overview.
CHAPTER 2 gives the recipe to construct a nuclear reaction network. The network is validated through many different examples toward the end of the chapter.
CHAPTER 3 a method is suggested for calculation of the γ-ray spectra due to π^0 production in a thermalized and non-fully thermalized plasma. Analytical fits are provided, too.
CHAPTER 4 considers nuclear reactions in accretion plasmas such as ADAF and SLE. The abundance evolution and γ-ray spectra are calculated for different accretion disk parameters. Upper limits are set for the γ-ray lines luminosity of the disk. The neutron, D, Li and Be abundances are calculated as a function of the disk parameters. The neutron evaporation efficiency is also calculated for ADAF model.
CHAPTER 5 provides conclusions and summary.

2 Nuclear reactions in very hot optically thin astrophysical plasmas

2.1 Introduction

Theoretical predictions on the radiation of very hot astrophysical plasmas with ion temperature $k_B\,T_i \geq 1$ MeV, motivate detail nuclear interaction studies. These very hot astrophysical plasmas are energetically able to initiate different nuclear reactions which can change its chemical composition and produce radiation that can be detected experimentally. All the relevant nuclear processes form a large nuclear reaction network. The main quantity that characterise each reaction channel is the rate which for a binary reaction $i + j \rightarrow k + ...$ is defined as (see e.g. Fowler et al., 1967)

$$\langle \sigma \upsilon \rangle_{ij}^{k}(T) = \sqrt{\frac{8}{\pi\,\mu_{ij}\,(k_B T)^3}} \int_0^\infty \sigma_{ij}^{k}(E)\,E\,\exp\left(-\frac{E}{k_{\rm B}T}\right) dE \quad \left[\mathrm{cm^3\,s^{-1}}\right]. \tag{2.1}$$

Here $\langle \sigma \upsilon \rangle_{ij}^{k}$ represents the rate averaged over the Maxwellian distribution, for a binary reaction $i + j \rightarrow k + ...$; σ_{ij}^{k} denotes the cross-section; E is the Center of Mass frame (CM) collision energy; T is the temperature; $k_{\rm B}$ is the Boltzmann constant, and μ_{ij} is the reduced mass of the interacting system $i + j$.

The main aim of this chapter is to build a nuclear reaction network to study composition and radiative processes of plasmas at temperatures $k_B\,T_i \geq 1$ MeV. With this we can solve the nuclear reaction network and calculate the γ-ray spectra due to ion interactions.

2.2 The nuclear reaction network

The calculation of the evolution of the nuclear abundances and the γ-ray line emission in low density, high temperature plasmas, requires the use of a comprehensive nuclear network. This network should take into account all relevant nuclear reactions that may occur in a hot plasma with $T \geq 1$ MeV.

There is an extensive literature dedicated the issue of how to build and solve nuclear networks (e.g. see Fowler et al., 1967; Hix and Thielemann, 1999). Nowadays, all this knowledge is compressed and very easy to access through on-line nuclear databases for astrophysical applications, such as *JINA Reaclib* (Cyburt et al., 2010), *NucAstroData* (Rauscher, 2006), *BRUSLIB*, *NetGen* and *NACRE II* (Jorissen and Goriely, 2001; Aikawa et al., 2005; Xu et al., 2013) and many more. There also exists many computer programs which store, manage and solve the networks, such as *libnuceq* and *libnucnet*.[1]

However, all these nuclear networks are designed for scenarios such as big-bang nucleosynthesis, core collapse supernova, stellar interiors, etc. Generally, they are valid for temperatures $T \leq 10^{10}$ K. Thus, to describe nuclear reactions for astrophysical plasmas with $T > 10^{10}$ K (or $k_B T \geq 1$ MeV), it is necessary to extend the aforementioned works.

Our main purpose here is to describe the evolution of the abundance of nuclear species and the γ-ray emission of a very hot, low density and optically thin astrophysical plasma. To further simplify the problem, we assume the following conditions hold:

1. All nuclei are instantaneously thermalized, and their velocity distributions are described by Maxwellian distribution.

2. All target nuclei interact in their ground state.

3. The plasma physical conditions and initial composition are such that photodisintegration and heavy nuclei reactions can be neglected.

These assumptions simplify the nuclear reaction network. The first assumption reduces the rate calculation formula to the eq. (2.1). The second assumption frees us to account for the nucleus excited states in the rate calculation. The last assumption reduces the number of reactions we should include into the nuclear network.

The assumption about instant thermalization may not be fully satisfy in nature because plasma may not be able to fully develop a Maxwellian distribution. The reason could be that the physical time-scales involved such as plasma lifetime are shorter than the thermalization time. Nevertheless, a plasma with a Maxwellian-like core distribution function and average energy $\langle E \rangle \sim k_B T \approx 10$ MeV is able to cover the most important energy interval of the nuclear cross-sections; therefore, the reaction rate will not depend on the tail of the distribution function. Thus, it is reasonable to calculate the rate for a Maxwellian distribution plasma.

[1] See the nuclear astrophysics group at Clemson University (http://www.webnucleo.org/home/modules/).

In a high temperature plasma, different isomeric states of a given nucleus may be in thermal equilibrium. Therefore, to obtain the reaction rate, one should sum the contributions of all isomers (see Woosley et al., 1978; Rauscher and Thielemann, 2000; Rauscher, 2011). A low density plasma such as the case for very hot accretion flows the excitation time is much longer than the de-excitation one. A typical number density for such accretion flows is $n \lesssim 10^{18}\,\mathrm{cm}^{-3}$, whereas a typical excitation rate is $\langle\sigma\upsilon\rangle < 10^{-14}\ \mathrm{cm}^3\,\mathrm{s}^{-1}$; hence, the excitation time-scale will be $\tau_{ex} = (n\,\langle\sigma\upsilon\rangle)^{-1} \gtrsim 10^{-4}$ s. On the other hand the de-excitation time-scale is typically $\tau_{ex} \lesssim 10^{-12}$ s. Therefore, nuclei cannot reach thermodynamic equilibrium and they will interact in their ground state.

Under the above assumptions, and since we are interested in low density plasmas, only the binary interactions contribute to the chain of nuclear reactions. The next section is devoted to justify the third assumption as well as to specify the most relevant binary nuclear reactions that play the main role in the plasma chemical composition evolution.

2.2.1 The nuclear reactions

Most of the astrophysical conditions – such as accretion flows – have an initial chemical composition similar to a solar one. For such compositions the Hydrogen (^{1}H or p) and Helium (^{4}He or α) are the most abundant elements making about 98 % of the plasma's mass. Other elements abundances – such as ^{16}O, ^{12}C, ^{14}N etc – will have less than 2 % of the plasma's mass (see e.g. Suess and Urey, 1956; Anders and Grevesse, 1989). In rarer cases plasma could be composed differently, and some elements heavier than ^{4}He may be much more abundant compare to a solar composition. The applicability of these cases will be discussed separately.

For studying purposes, let we divide the nuclear reactions into three groups. The first group involve the reactions between hydrogen and helium, the second one involves the reactions of hydrogen and helium with elements heavier than ^{4}He and the last group involves the reactions between elements heavier than ^{4}He. Based on the initial abundances, the most relevant reactions of the first group are $p+\alpha$, $\alpha+\alpha$ and $p+p$ inelastic collisions. During the plasma chemical evolution, isotopes such as D (^{2}H), T (^{3}H) and ^{3}He become abundant. As a result the reactions such as $p+D$, $p+T$, $p+{}^3$He, $\alpha+D$, $\alpha+T$ and $\alpha+{}^3$He become important and thus must be included in the nuclear network. A full description of these reactions cross-sections and their corresponding channels are shown in tables 2.1 and 2.2. The most important nuclear reactions in the second group are those between p and α with elements heavier than ^{4}He. Because the heavy elements make up less

than 2 % of the plasma's mass composition, the reaction of the third group will be negligible.

Neutrons (n) are unstable particles with mean lifetime $\tau_n = 880.1 \pm 1.1$ s (Beringer et al., 2012, (PDG)). They are not initially present in the plasma. However, during the plasma evolution the heavy nuclei spallation processes as well as $p + p$ inelastic interactions at high temperatures, produce many neutrons. These neutrons quickly become abundant such that their number density ratio with respect to protons can be as large as $n_n/n_p \leq 0.1$ depending on the plasma temperature. Therefore, neutron reactions with other particles can become as important as p and α reactions. Hence, all neutron reactions are included in the nuclear reaction network.

To summarize, the most important nuclear reactions are the binary reactions where at least one of the particles is a n, a p or an α-particle. All other possible nuclear reactions will be negligible. As it is shown in the appendix A, all discarded reactions for a solar composition plasma do not contribute more than 0.4 % of the dominant reaction channels. In case of high metallicity plasma the solution can still be reasonably accurate if $n_{\mathcal{A}}/n_p \lesssim 10^{-1}$ – $\mathcal{A}$ is an element heavier than ^{4}He. However, the solution accuracy for this case will drop to 7 %.

Although the nuclear reaction rates for p, n and α projectiles can be simply calculated from the local conditions of the plasma – such as ion temperature and density – this is not the case for the interactions of photons with nuclei. The γ-interaction reaction rates not only depend on local parameters, but also on the number density of photons, which itself depends on the optical depth of the plasma. Furthermore, the optical depth is also a function of "non-local" variables such as the electron number density and size of the object (plasma).

The γ-rays are produced and transported inside the plasma. Hot two-temperature plasmas radiate X-rays and γ-rays through interactions of both components of the plasma. The dominant radiative cooling channels for ions are the excitation of nuclei with production of prompt γ-ray lines such as ^{12}C(4.44 MeV) or ^{16}O(6.13 MeV) and ^{16}O(6.92 MeV) lines, the γ-radiation released at $p - n$ capture, as well as $p - n$ bremsstrahlung. For very high temperature plasmas an additional radiative component come from the $p + p$ inelastic collisions that produce π^0 which quickly decay to two photons. The electronic component radiates more efficiently, predominantly through thermal bremsstrahlung, and in the case of large optical depth, is cooled due to comptonization.

Because the photon number density depends on the optical depth of the plasma, the effect of the photodisintegration of nuclei cannot be estimated without considering the plasma as a whole. The importance of this effect

must be checked for each specific problem. As it is illustrated in appendix B the effect of the photodisintegration on ^{16}O and D nuclei – for the case of a spherically symmetric and optically thin plasma – is negligible. The photodisintegration of all radiative components do not make more than 0.1 % of the dominant nuclear reactions. It is shown in the appendix B that even if the electron temperature is comparable with the ion temperature, the effect of photodisintegration on the evolution of the plasma can still be safely neglected. However, this might not be the case for an optically thick plasma, or for the case where nuclear statistical equilibrium is reached.

We conclude here by noting that if heavy nuclei reactions are initially negligible, they will always be so. The reason is that nuclear spallation reactions will destroy all heavy nuclei during the plasma evolution.

2.2.2 The nuclear reaction cross-sections

Nuclear reaction rates are the main ingredient of a nuclear network. Knowing them precisely, allows us to make accurate predictions. To calculate the Maxwellian averaged rate of a nuclear reaction, we must know the reaction cross-section. Typically, a nuclear reaction cross-section peaks from few MeV/nucleon to few-tens of MeV/nucleon. Thus, for a plasma with $k_B T > 1$ MeV the most important projectile energy window is within $E < 200$ MeV/nucleon. At such high energies nuclear reaction mechanisms such as direct, pick-up and pre-compound become important. The recently established, publicly available TALYS code (A.J. Koning and Duijvestijn, 2007), has incorporated all these mechanisms and is thus ideal to use. The TALYS code is attractive because it has the following features:

i. it offers a projectile energy range 1 keV-250 MeV or higher because it includes pre-equilibrium reactions,

ii. it incorporates modern nuclear models for the optical model, level densities, direct reactions, compound reactions, pre-equilibrium reactions,

iii. it can treat γ, n, p, D, T, ^{3}He, and α-particles as both projectiles and ejectiles,

iv. target mass numbers can be between $A = 12$ and $A = 339$. The code can also calculate cross-section for targets with mass number in the range $A = 6 - 12$, but the results may not be as accurate.

Very hot and optically thin astrophysical plasmas can reach ion temperatures of order $T_i \sim 10^{12}$ K (~ 100 MeV). To calculate the Maxwellian average rate $\langle \sigma \upsilon \rangle$ at such high temperatures with an accuracy better than 5 %, we

Table 2.1: Isotopes of Hydrogen reaction cross-sections

Reaction	Description
p(n, γ)D	Data from *JENDL High Energy File 2007 (JENDL/HE-2007)* (n.d.) valid for projectile energy up to 3 GeV.
D(n, 2n)p D(n, γ)T D(p, np)p D(p, γ)^{3}He D(α, np)^{4}He	Data from ENDF/B-VII.0 (*Evaluated Nuclear Data File (ENDF)*, n.d.) valid for projectile energy up to 150 MeV.
T(n, 2n)D T(p, n)^{3}He T(p, D)D	Data from ENDF/B-VII.1 evaluations (*Evaluated Nuclear Data File (ENDF)*, n.d.) valid for projectile energy up to 20 MeV.
T(n, 3n)p	Data from JEFF-3.1 evaluations (*The Joint Evaluated Fission and Fusion File (JEFF) OECD/NEA Data Bank*, n.d.), valid for projectile energy up to 20 MeV.
T(p, γ)^{4}He	For this reaction no theoretical evaluations have been found; therefore the experimental data from (*Expermimental Nuclear Reaction Data (EXFOR/CSISRS)*, n.d.) were used. From 10-100 keV in CM-system, data were taken from Canon et al. (2002). For 8.34 and 13.6 MeV data from Calarco et al. (1983).
T(α, n)^{6}Li	Again no evaluations, data were extracted by Spiger and Tombrello (1967). These data are valid up to 18 MeV.

should extend the projectile energy window up to 450 MeV – as it is estimated in appendix C. For this reason I have extrapolated all TALY's cross-sections from 250 to 450 MeV as $\sigma \sim E^{-1}$ – similar to geometrical cross-section.

In this work we will use TALYS to calculate the cross-sections for reactions involving elements from ^{6}Li to ^{70}Zn. For targets with $A \leq 6$ (i.e. n, p, D, T, ^{3}He, ^{4}He), the cross-sections are collected from theoretical evaluations; when no evaluations were available experimental data are used instead. Both evaluations and experimental data points were taken from the publicly available databases (*Evaluated Nuclear Data File (ENDF)*, n.d.; *Expermimental Nuclear Reaction Data (EXFOR/CSISRS)*, n.d.).

It must be mentioned here that using evaluations or experimental data from different sources introduce additional uncertainties. Some evaluations do not exceed projectile energies of 20 MeV. In these cases, the cross-section is extrapolated in the high energy region as $\sigma \sim E^{-1}$. Tables 2.1 and 2.2 list all reactions with $A \leq 6$ that are taken into account here. The fig. 2.1 shows some important cross-sections.

Table 2.2: Isotopes of Helium reaction cross-sections

Reaction	Description
^{3}He(n, p)T ^{3}He(n, D)D ^{3}He(n, γ)^{4}He ^{3}He(p, 2p)D	Evaluations from ENDF/B-VII.0 (*Evaluated Nuclear Data File (ENDF)*, n.d.), which are valid up to 20 MeV.
^{3}He(α, γ)^{7}Be	No evaluations. Experimental data in the interval 0.02-3.13 MeV collected by different authors (experiments from 2008-2009). Consult the EXFOR Database (*Expermimental Nuclear Reaction Data (EXFOR/CSISRS)*, n.d.).
^{4}He(n, D)T	Data around 22 MeV from Shamu and Jenkin (1964), and one point at 50MeV differential cross sections from Sagle, Bonner, Brady, King, McNaughton, Romero and Ullmann (1991).
^{4}He(p, D)^{3}He	Experimental data for 31 MeV from Bunch et al. (1964) for 32 MeV, 40 MeV, 50 MeV and 52.5 MeV from Sagle, Bonner, Brady, King and Romero (1991) for 85 MeV from Votta et al. (1974) and for 200 MeV and higher from Alons et al. (1986).
^{4}He(α, p)^{7}Li ^{4}He(α, n)^{7}Be ^{4}He(α, 2p)^{6}He ^{4}He(α, np)^{6}Li ^{4}He(α, D)^{6}Li	Data taken from King et al. (1977) for energies between threshold and 50 MeV. For energies higher than 60 MeV, measurements from Glagola et al. (1982) and fits from Mercer et al. (2001) were used. In the work of King et al. (1977), there are also data for the excited-state cross section of ^{7}Li(0.478) production γ-ray line.

The π-mesons production cross-section

At very high temperatures, $p + p$ inelastic collisions are able to produce π-mesons. The main $p + p$ reactions are

$$pp \rightarrow pp\pi^0; \;\; pp \rightarrow pn\pi^+; \;\; pp \rightarrow D\pi^+; \;\; pp \rightarrow \pi^- ...$$

Thus, a very hot, pure proton plasma will quickly convert protons to neutrons and some deuterium. As a result, the interactions of neutrons that produce π-meson should be taken into account, too. The neutron reactions are:

$$np \rightarrow np\pi^0; \;\; np \rightarrow pp\pi^-; \;\; np \rightarrow nn\pi^+; \;\; np \rightarrow D\pi^0$$

$$nn \rightarrow np\pi^-; \;\; nn \rightarrow nn\pi^0; \;\; nn \rightarrow D\pi^-$$

The neutron reaction cross-sections can be related with proton ones through the isospin symmetry (see e.g. Rosenfeld, 1954; Gell-Mann and Watson, 1954).

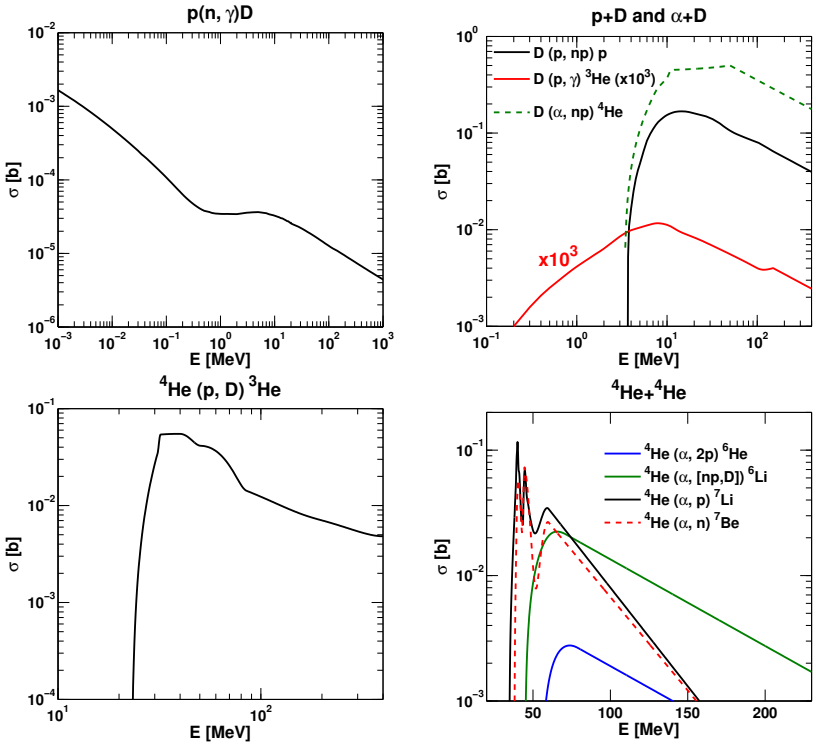

Figure 2.1: Some nuclear reaction cross-sections for some important reactions of hydrogen and helium isotopes

The cross-sections of reactions that will influence p and n abundances are related as follows:

$$\sigma(nn \to np\pi^-) = \sigma(pp \to pn\pi^+) \tag{2.2}$$

$$\sigma(nn \to D\pi^-) = 2\,\sigma(np \to D\pi^0) = \sigma(pp \to D\pi^+) \tag{2.3}$$

The $\sigma(pp \to pn\pi^+)$ and $\sigma(pp \to D\pi^+)$ are well measured experimentally see fig. 2.2 (see e.g. Machner and Haidenbauer, 1999).

Dermer (1986) has suggested the following cross-sections fits:

$$\sigma(pp \to pn\pi^+) = \begin{cases} 0 & : 0 < p_p \leq 0.79621\ GeV/c \\ 0.95\eta^4 + 0.099\eta^6 + 0.204\eta^8 & : 0.79621 < p_p \leq 0.95\ GeV/c \\ 0.67\eta^{4.7} + 0.3 & : 0.95 < p_p \leq 1.29\ GeV/c \\ 22.0(p_p - 1.27)^{0.15} & : 1.29 < p_p \leq 4.0\ GeV/c \end{cases} \tag{2.4}$$

$$\sigma(pp \to D\pi^+) = \begin{cases} 0 & : 0 < E_k \leq 0.28755\ GeV \\ 0.18\eta + 0.95\eta^3 - 0.016\eta^9 & : 0.28755 < E_k \leq 0.65\ GeV \\ 0.56\,E_k^{-3.9} & : 0.65 < E_k \leq 1.43\ GeV \\ 0.34\,E_k^{-2.5} & : E_k \geq 1.43\ GeV \end{cases} \tag{2.5}$$

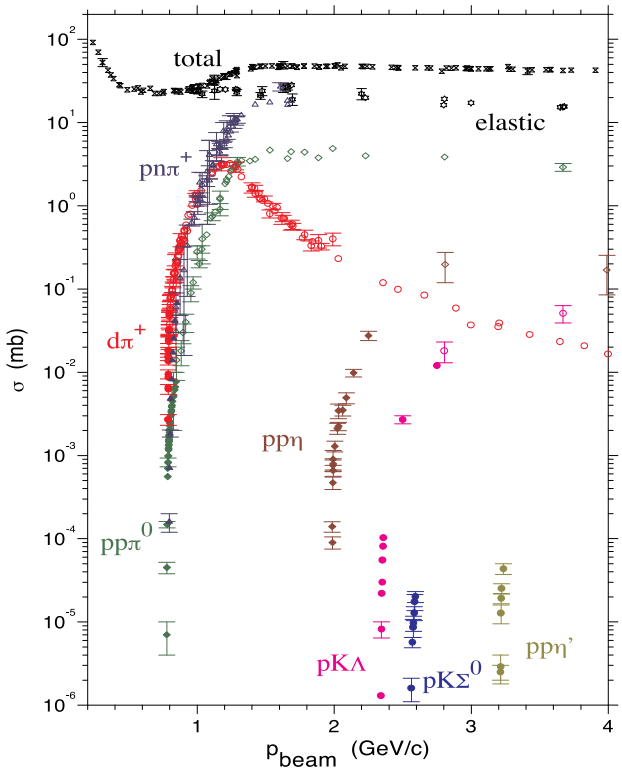

Figure 2.2: The cross-sections for different $p + p$ interaction channels as a function of collision momenta. The elastic and total cross-sections are shown as well. The figure is taken from Machner and Haidenbauer (1999).

Both cross-sections are in millibarn (mb). The $\eta = p_\pi^{max}/m_\pi c$, p_π^{max} and m_π are the maximum π^+ momentum and mass, respectively. $s = 2m_p c^2(E_p + m_p c^2)$ is the full center of mass energy, m_p is the proton mass and $E_p = \sqrt{p_p^2 c^2 + m_p^2 c^4}$ is the full proton collision energy and p_p is the collision momenta. The parameter η is:

$$\eta = \frac{\sqrt{(s - m_\pi^2 c^4 - 4m_p^2 c^4)^2 - 16 m_\pi^2 m_p^2 c^8}}{2m_\pi c^2 \sqrt{s}} \tag{2.6}$$

2.2.3 Constructing the nuclear network

First of all the reaction network should in principle satisfy a "closure condition": the reaction products of all nuclei in the network must be also part of the same network. In practice we select the most relevant reactions/channels, which implies that the closure condition holds only approximately. We can fix the accuracy up to which the closure condition is satisfied by introducing a threshold value for the Maxwellian average rate ($\langle\sigma\upsilon\rangle$). Every channel with a Maxwellian average rate smaller than the threshold is ignored. Changing the value of the threshold changes the number of reaction

channels in consideration, therefore this parameter plays a crucial role in the accuracy of the solution, the calculation time, the dimension of the network, etc.

To calculate the cross-sections and the Maxwellian average rates for the reactions of nuclei from ^{6}Li to ^{70}Zn, the following algorithm is constructed. First of all we introduce a first generation of nuclei which is chosen to be the solar composition of nuclei from ^{6}Li to ^{70}Zn. Then by using TALYS code for n, p and α-particle projectiles and the first generation of nuclei targets, all the reaction cross-sections for each channel and γ-ray line are calculated. Then using these cross-sections the Maxwellian average rate is calculated according to eq. (2.1). At $T = 1$ MeV the largest reaction rates are of the order of $\langle\sigma\upsilon\rangle_{ij}^k \sim 10^{-16} - 10^{-15}$ cm^3 s^{-1}. By choosing a threshold value $R^{\rm th} = 10^{-19}$ cm^3 s^{-1}, we ensure that the contribution of the dismissed reactions would be no more than 0.1%.

From the selected channels new targets may appear. They are potentially created in the plasma due to the reactions of the previous generation of nuclei, and they enter in calculations as a second target generation. After that the previous procedure is repeated for the new targets, i.e. calculating the cross-sections, the reaction rates, and the selection of the relevant channels according to the chosen threshold value. The new channels may still introduce a third generation of new nuclei. We have to apply the algorithm until there is no generation of new nuclear species. The network is then closed up to the accuracy given by $R^{\rm th}$.

The Maxwellian average rates for the isotopes of hydrogen and helium are calculated separately from the above algorithm. They are then added to the large nuclear network.

To save the calculation time, the Maxwellian average rates $\langle\sigma\upsilon\rangle_{ij}^k$ are fitted as a function of temperature using the parametrization suggested in Thielemann et al. (1986); Rauscher and Thielemann (2000) :

$$\langle\sigma\upsilon\rangle_{ij}^k = \exp(a_1 + a_2\,T^{-1} + a_3\,T^{-\frac{1}{3}} + a_4\,T^{\frac{1}{3}} + a_5\,T + a_6\,T^{\frac{5}{3}} + a_7\,\log T). \qquad (2.7)$$

The fit is valid for $T \in [0.1,\ 200]$ MeV. The goodness of the fit is estimated for the seven parameters using the χ^2 method. In the mentioned temperature range the majority of the rates have a residual fluctuation less than 20%.

2.3 Gamma-ray emission

High temperature and low density plasma have a characteristic γ-ray spectrum component that results from nuclear processes. The most important nuclear processes are the ones that produce prompt γ-ray lines, $p-n$ capture and bremsstrahlung (see e.g. Aharonian and Sunyaev, 1984). At very high

temperatures ($k_B\,T > 20$ MeV) the π^0 production start to become important; thus an additional component of the γ-ray spectra appears.

The MeV-range γ-ray spectra are composed by nuclear lines component – result of nuclear de-excitation into different isomeric states – as well as a continuum component made of the nuclear bremsstrahlung and nuclear reactions such as the capture reactions ^{1}H(n,γ)D, D(n,γ)T, D$(p,\gamma)^3$He, and T$(p,\gamma)^4$He, etc.

Let the Φ_γ be the gamma-ray emissivity. If $\dot{n}_\gamma$ is the number of γ-rays emitted per unit time and volume at energy E_γ, then the emissivity can be written as:

$$\Phi_\gamma(E_\gamma) = E_\gamma \, \frac{d\dot{n}_\gamma(E_\gamma)}{dE_\gamma} \;\; \mathrm{cm}^{-3}\,\mathrm{s}^{-1}. \tag{2.8}$$

2.3.1 Nuclear γ-ray lines emissivity

In a thermal plasma the excited nuclei have a Maxwellian velocity distribution, therefore the emitted γ-ray lines will be Doppler-broadened. The Doppler broadening (Γ_D) of a γ-ray line with a central energy E^0_γ emitted by a nuclei of mass m in a plasma at temperature T is

$$\Gamma_D = \sqrt{\frac{8\ln(2)\,k_B T}{mc^2}}\; E^0_\gamma\,. \tag{2.9}$$

In a high-temperature plasma Γ_D is much larger than the natural width Γ_0 for almost all the strongest lines. For such condition the nuclear line broadening profile is a Gaussian profile. If the energy of the photon emitted by the nucleus at rest is E^0_γ, and if $\dot{n}_\gamma$ is the number of photons with energy E^0_γ that are emitted per unit time and volume, then the emissivity can be written as

$$\Phi^l_\gamma(E_\gamma) = \frac{E^0_\gamma\,\dot{n}_\gamma}{\sqrt{2\pi\sigma^2_G}} \;\exp\left[-\frac{(E_\gamma - E^0_\gamma)^2}{2\sigma^2_G}\right], \tag{2.10}$$

where the Gaussian broadening σ_G is

$$\sigma_G = \sqrt{\frac{k_B T}{mc^2}}\; E^0_\gamma\,.$$

2.3.2 Gamma-ray emissivity of capture reactions

The γ-rays emissivity of a capture reaction $1 + 2 \rightarrow 3 + \gamma$, such as for instance the $n + p \rightarrow \mathrm{D} + \gamma$, is given by eq. (2.11) and eq. (2.12). The formula is derived in appendix D.

$$\Phi^c_\gamma(E_\gamma, T) = n_1\, n_2 \times \left(\frac{2\,m_3\,c}{\pi\,(m_1 m_2)^{1/2}\,(k_B T)^2}\right) E_\gamma \times \mathcal{I}(E_\gamma, T) \tag{2.11}$$

where

$$\mathcal{I}(E_\gamma, T) = \int dE \, \frac{E\,(E+Q)\,\sigma(E)}{E_\gamma^2} \times \\ \times \exp\left(-\frac{m_3^2\,c^2}{2(m_1+m_2)\,k_B T} \left(1 - \frac{E+Q}{E_\gamma}\right)^2 - \frac{E}{k_B T} \right) \tag{2.12}$$

Here n_1 and n_2 are the number densities of species 1 and 2. The m_1, m_2 and m_3 are the masses of particles 1, 2 and 3. The E_γ is the γ-ray energy in the LAB-frame, E is the collision energy in the center-of-mass frame, and $\sigma(E)$ and Q are the cross-section and the Q-value of the reaction, respectively.

The recoil of nuclei 3 is neglected in Eq.(2.11), i.e. terms $\propto E_\gamma/2m_3c^2$ are not included. The energy of the interacting particles is $\sim k_B\,T$, so most of the photons will be produced with an energy of the order of $E_\gamma \sim Q + k_B\,T$; thus $(Q + k_B\,T)/m_3 < 10^{-2}$ and the approximation is justified.

2.3.3 Gamma-ray emissivity of nuclear bremsstrahlung

Nuclear Bremsstrahlung involves electrodynamics and nuclear physics. There are different phenomenological treatment of nuclear bremsstrahlung in the literature. They involve classical, semi-classical and quantum treatment.

Edgington and Rose (1966) have found experimentally that the nuclear bremsstrahlung spectra from $p + {}^{A}_{Z}X$ interaction – where Z and A are the the nucleus X charge and mass, respectively – follows the law:

$$\frac{d\sigma_{p\mathcal{X}}}{dE_\gamma} = \frac{(A-Z)}{A^{1/3}} \times \frac{d\sigma_{pn}}{dE_\gamma} \tag{2.13}$$

where the $d\sigma_{pn}/dE_\gamma$ is the proton-neutron bremsstrahlung differential cross-section.

The application of p-n capture and nuclear bremsstrahlung radiation in a very hot proton-neutron plasma is described in Aharonian and Sunyaev (1984). For a very hot accretion plasma where nuclei are not fully destroyed the effect in eq. (2.13) should be taken into account.

There exist an extensive literature of how to calculate the p-n and p-p bremsstrahlung differential cross-sections (see e.g. Ashkin and Marshak, 1949*a*,*b*; Aharonian and Sunyaev, 1984; Bauer, Bertsch, Cassing and Mosel, 1986; Bauer, Cassing, Mosel, Tohyama and Cusson, 1986; Remington et al., 1987; Njock et al., 1988; Nifenecker and Pinston, 1989). Here, we will use the p-n bremsstrahlung semi-classical formula from Aharonian and Sunyaev (1984) because their differential cross-section describes reasonably well the experimental data:

$$\frac{d\sigma_{np}}{dE_\gamma} \simeq \frac{2\,\alpha}{3\,\pi\,E_\gamma} \sqrt{1 - \frac{E_\gamma}{E}} \; \frac{(2E - E_\gamma)}{m_p\,c^2} \; \sigma_{np}^{el}(E) \tag{2.14}$$

Here E is the collision energy, and E_γ is the photon energy; α is the fine structure constant and the σ^{el}_{np} is the elastic p-n scattering which is taken from *JENDL High Energy File 2007 (JENDL/HE-2007)* (n.d.). The m_p is the proton mass.

In fig. 2.3 are compared the differential cross-section models from Ashkin and Marshak (1949*a*); Aharonian and Sunyaev (1984) and Bauer, Bertsch, Cassing and Mosel (1986) at the laboratory frame projectile energy E_L = 100 MeV.

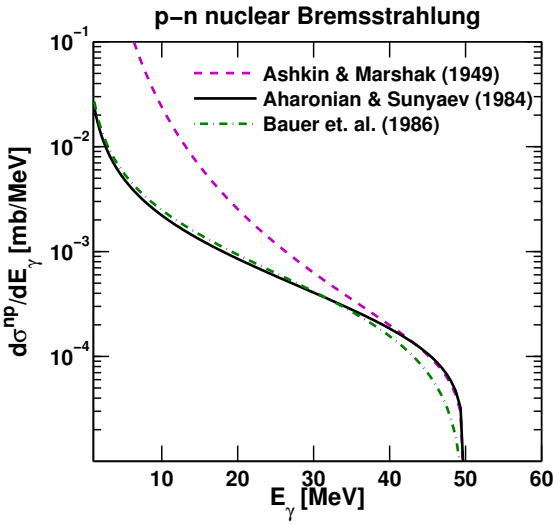

Figure 2.3: Comparison of the p–n bremsstrahlung differential cross-section at the projectile energy E_L = 100 MeV from Ashkin and Marshak (1949*a*); Aharonian and Sunyaev (1984); Bauer, Bertsch, Cassing and Mosel (1986) .

By inserting the differential cross-section of eq. (2.14) in the eq. (2.1), we obtain the photo-production rate per photon energy interval due to p-n interactions:

$$\frac{dR^b_{np}}{dE_\gamma}(E_\gamma) = \sqrt{\frac{16}{\pi\, m_p\, (k_B T)^3}} \int_0^\infty \frac{d\sigma_{np}}{dE_\gamma}(E_\gamma, E) \times E\, \exp\left(-\frac{E}{k_B T}\right) dE \tag{2.15}$$

Using eq. (2.13) we obtain the nuclear bremsstrahlung emissivity for all reactions $p + ^A_Z X$:

$$\Phi^b_\gamma(E_\gamma) = n_p^2 \times \left(\sum_i \frac{(A_i - Z_i)}{A_i^{1/3}} \left(\frac{n_{x_i}}{n_p}\right)\right) \times \left(E_\gamma \times \frac{dR^b_{np}}{dE_\gamma}(E_\gamma)\right) \tag{2.16}$$

The n_p and n_x are the number densities of protons and nucleus X, respectively.

2.4 The solution of the nuclear network

The Maxwellian average rates $\langle\sigma\upsilon\rangle_{ij}^{k}$ – that we calculated in the previous section – enter into the kinetic equations of the plasma chemical evolution (see e.g. Woosley et al., 1978). If we define the mass fraction abundance of the element i as $X^i = A_i\, n^i/\varrho_u$, where A_i is the mass number, n^i is the number density and $\varrho_u \equiv \sum_l A_l\, n^l$ the nucleon number density[2], then the kinetic equation reads:

$$\dot{X}^k = \sum_{i}^{n,p,\alpha} \sum_{j}^{N} \frac{\varrho_u}{1+\delta_{ij}} \left(\frac{A_k}{A_i\, A_j}\right) \langle\sigma\upsilon\rangle_{ij}^{k}\; X^i\, X^j. \tag{2.17}$$

The index i runs over the three projectiles n, p and α; whereas the index j runs over all elements of the network – here the number of nuclei that are taken into account is about 270 and they cover elements from n and p to ^{70}Zn. Note that the sum in eq. (2.17) includes both, positive and negative terms. Negative terms include processes that destroy the nucleus k.

To solve the nuclear reaction network means to solve the system of differential equations in eq. (2.17), for every specie in the network. Due to relatively large number of nuclear species, the system of differential equations is too complicated to be solved analytically; thus, it must be solved numerically. The differential equations in eq. (2.17) are stiff ones; hence, I use the Matlab®'s *"ode15s"* numerical solver. This numerical solver is an implementation of the Klopfenstein-Shampine family of Numerical Differentiation Formulas (NDF) of orders 1 to 5 (*MathWorks Inc. (Matlab R2009b)*, n.d.)

The numerical solver does not always guarantee a physically meaningful solution, thus some constraints are included to be checked in every solution step. The constraints originate from conserved quantities such as the number of nucleons (or baryon number conservation), electric charge, etc. One of the most important constraints is baryon number conservation, which can be written as

$$\dot{\varrho}_u = 0 \;\Rightarrow\; \sum \dot{X}_i \equiv 0 \;\Leftrightarrow\; \sum A_i \dot{n}_i \equiv 0 \tag{2.18}$$

This condition ensures that the number of nucleons remain constant even if, for instance, neutrons decay.

By defining the plasma temperature (T), nucleon number density (ϱ_u) and initial abundances for each element of the network, we can now solve the network and obtain the abundances temporal evolution for every element as well as we can calculate the γ-ray emissivity spectra for such plasma.

[2] In practice, nucleon number density ϱ_u can be converted to mass density ρ_{mass}, simply by multiplying it with nucleon mass m_u, $\rho_{mass} \approx \varrho_u \times m_u$

2.4.1 A pure proton plasma

Let us consider a unit volume of plasma at two fixed-temperatures, 30 MeV and 100 MeV. The nucleon number density for this plasma is assumed $\varrho_u = 10^{18}$ cm^{-3}. This nucleon number density will be kept fixed for all the examples that are shown in this chapter. This number density is a typical value for a very hot, two temperature, optically thin accretion plasma.

At low temperatures $k_B T < 20$ MeV, pure proton plasma is dominated by p–p elastic scattering. As a result the proton abundance does not change. At temperatures higher than $k_B T > 20$ MeV, p–p inelastic collisions start to produce π-mesons. This collision convert protons to neutrons and to deuterium.

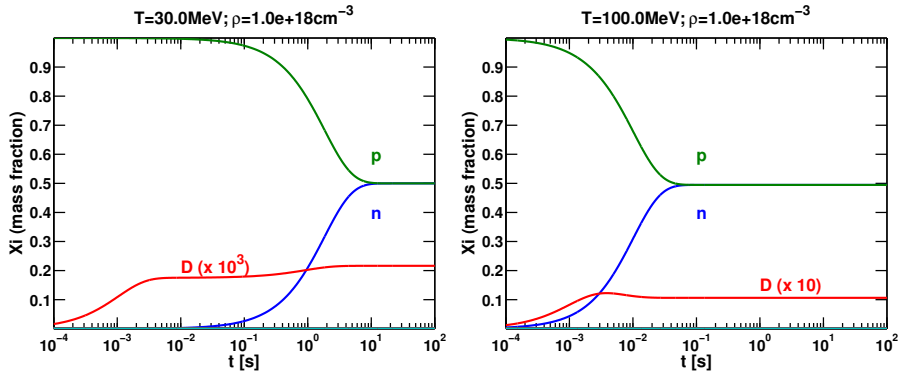

Figure 2.4: Abundance evolution of a very hot and initially pure proton plasma. On the left is shown the mass fraction abundance evolution for temperature $k_B T = 30$ MeV and on the right hand side that of temperature $k_B T = 100$ MeV. Both solutions have initial mass fraction abundance $X_p = 1$ (pure proton) and the nucleon number density $\varrho_u = 10^{18}$ cm^{-3}. The green line shows the proton abundance evolution, blue line that of neutrons and the red one is the deuterium multiplied to the coefficient shown in brackets.

The π-mesons production cross-sections satisfy the isospin symmetry; therefore a pure proton plasma will result a proton-neutron (p-n) plasma, with equal amount of protons and neutrons ($X_n = X_p = 0.5$). Deuterium is also produced in such plasmas due to the capture reaction and π-meson production.

In a pure proton plasma the deuterium is formed only through $p + p \rightarrow D + \pi^+$. On the other hand, protons destroy deuterium through the pick-up reaction $p + D \rightarrow 2p + n$. Therefore, the amount of deuterium in a fixed temperature plasma is give by:

$$\dot{n}_D = n_p^2 \left(\frac{R_{pp}}{2} - R_{pD} \frac{n_D(t)}{n_p} \right),$$

where R_{pp} is the abbreviation for the rate ($\langle \sigma \upsilon \rangle$) of the reaction $p + p \rightarrow D$

and R_{pD} that of deuterium destruction $p + D$. The n_p and n_D are the number densities of proton and deuterium in the plasma.

The solution of the eq. (2.17), gives initially a linear rise of the deuterium number density ($n_D = R_{pp}\, n_p^2\, t/2$), then with the increase of n_D, the destruction process tends to equilibrate the amount of D to a value

$$\frac{n_D^{eq}}{n_p} = \frac{R_{pp}(T)}{2\, R_{pD}(T)}.$$

At temperature $k_B T = 30$ MeV, $R_{pp} \approx 1.7 \times 10^{-19}\,\mathrm{cm^3\,s^{-1}}$ and $R_{pD} \approx 9 \times 10^{-16}\,\mathrm{cm^3\,s^{-1}}$; thus the equilibrium value is $n_D^{eq}/n_p \approx 9{\times}10^{-5}$ or in mass fraction abundance ratio $X_D^{eq}/X_p = 2 \times (n_D^{eq}/n_p) \approx 1.8 \times 10^{-4}$.

At temperature $k_B T = 100$ MeV the $R_{pp} \approx 1.3 \times 10^{-17}\,\mathrm{cm^3\,s^{-1}}$ and $R_{pD} \approx 9 \times 10^{-16}\,\mathrm{cm^3\,s^{-1}}$; thus the equilibrium value – if it would have enough time to reach it – is $n_D^{eq}/n_p \approx 7 \times 10^{-3}$ or $X_D^{eq}/X_p = 2 \times (n_D^{eq}/n_p) \approx 1.4 \times 10^{-2}$.

For $t > (n_p \times \langle \sigma \upsilon \rangle_{pp\to n})^{-1}$, the protons start to effectively be converted to neutrons until the equilibrium is reached. This causes a shift in the equilibrium abundance of the deuterium.

The pure proton plasma produce γ-rays through π^0 production in p–p inelastic collisions as well as through p–n capture.

2.4.2 A proton-neutron plasma

Assume an initial p–n plasma. In reality this plasma is a product of the evolution of other plasmas. It may come form a plasma that has destroy all nuclei or from a plasma as shown in the previous example. As shown in section 2.4.1, this plasma will not show a noticeable abundance evolution for temperatures $k_B T > 1$ MeV. In case of an initial asymmetry between the amount of protons and neutrons, the plasma will only evolve to an equal amount of protons and neutrons if it is able to produce π-mesons efficiently.

Figure 2.5 shows the p-n plasma γ-ray emissivity for temperatures 1, 10 and 100 MeV. The γ-ray spectra through π^0 production it is not shown.

2.4.3 A pure ^{4}He plasma

The abundance evolution analysis

The $\alpha + \alpha$ reactions produce light elements dominated by ^{6}Li, ^{7}Li and ^{7}Be. For the pure He-plasma with constant temperature and density, the Li or Be production rate would be:

$$\dot{n}_{Li/Be} = R_{\alpha\alpha} \frac{n_\alpha^2}{2}$$

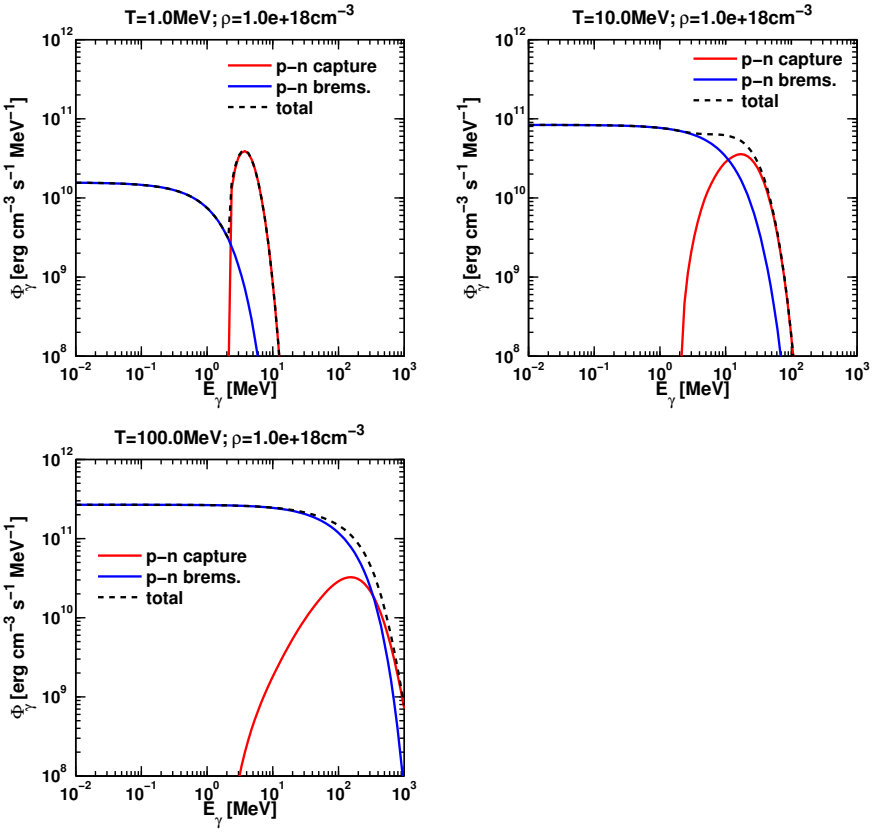

Figure 2.5: The γ-ray emissivity of an initial p-n plasma for three temperatures 1, 10 and 100 MeV. For this example the initial mass fractions are set $X_p = X_n = 0.5$ and the nucleon number density is fixed at $\varrho_u = 10^{18}$ cm^{-3}. The spectrum is a composition of p-n bremsstrahlung and capture reaction. The γ-ray emissivity due to π^0 production is not included here.

The $n_{Li/Be}$ and n_α are the number densities of Li (or Be) and ^{4}He, respectively. The $R_{\alpha\alpha}$ is the Maxwellian average rate for producing Li or Be through the $\alpha + \alpha$ reactions.

Initially the destruction processes are negligible; therefore, one obtains:

$$n_{Li/Be}(t) = R_{\alpha\alpha}\frac{n_\alpha^2}{2} \times t = \left(\frac{n_\alpha}{2}\right) \times \left(\frac{R_{\alpha\alpha}}{R_\alpha^t}\right) \times \left(\frac{t}{\tau_\alpha}\right),$$

where $\tau_\alpha = (n_\alpha\, R_\alpha^t)^{-1}$ is the ^{4}He destruction time-scale and R_α^t is the destruction rate at the given plasma temperature. We thus conclude that the first generation products of $\alpha+\alpha$ reactions, have abundances that depend linearly with time ($X_i \propto t$) for $t \ll \tau_\alpha$.

The α-particles can interact with the first generation of nuclei (G1 such as Li or Be) to produce a second generation (G2). The production rate for the second generation is written:

$$\dot{n}_{G2} = R_{\alpha G1} n_\alpha n_{G1}$$

Its solution will be:

$$n_{G2}(t) = \left(\frac{n_\alpha}{2}\right) \times \left(\frac{R_{G1}}{R_\alpha^t}\right) \times \left(\frac{R_{G2}}{R_\alpha^t}\right) \times \left(\frac{t}{\tau_\alpha}\right)^2 .$$

The R_{G1} and the R_{G2} are the production Maxwellian average rates for the generation G1 and the generation G2, respectively, at the given plasma temperature.

Using this expression, we can generalise the last result to the N'th generation (GN), for which the number density will be:

$$n_{GN}(t) = \left(\frac{n_\alpha}{2}\right) \times \left[\left(\frac{R_{G1}}{R_\alpha^t}\right) \times \cdots \times \left(\frac{R_{GN}}{R_\alpha^t}\right)\right] \times \left(\frac{t}{\tau_\alpha}\right)^N ,$$

where the R_{G1} to R_{GN} are the production rates for each generation from their previous one.

Therefore, we conclude that the N'th generation abundance have a $X_i \propto t^N$ dependence for $t \ll \tau_\alpha$. Hence, it is remarkable that the higher the generation of a product is, the steeper will its abundance raise with time.

When the plasma evolution time becomes comparable to the ^{4}He destruction time-scale $t \sim \tau_\alpha$, each generation abundance reaches the maximum. The maximum possible number density for the generation N'th is given by:

$$n_{GN}^{max} \simeq \left(\frac{n_\alpha}{2}\right) \times \left[\left(\frac{R_{G1}}{R_\alpha^t}\right) \times \cdots \times \left(\frac{R_{GN}}{R_\alpha^t}\right)\right].$$

The peak value is always $n_{GN} < n_{GN}^{max}$, because the above formula is valid for $t \ll \tau_\alpha$.

Suppose that the generation "i'th" has a very small rate $R_{Gi} \ll R_\alpha^t$. As a result the "i'th" generation will have an insignificant abundance; hence, the generations "i'th + 1" will barely form. On the other hand if the rate is too high then the generation "i'th - 1" does not exist because it is quickly converted to generation "i'th". Thus to have a chain of reactions similar with what is described above, the rates between generations will not change drastically from each other. Therefore, we cannot gain very high number density of the N'th generation by considering for instance, one channel with very high rate.

For a period of time larger than the destruction of ^{4}He ($t > \tau_\alpha$) the amount of ^{4}He and other products that depend on it, will decline. The ^{4}He is destroyed by itself from $\alpha + \alpha$ reactions initially, but soon the proton abundance becomes large; thus the $p + \alpha$ reactions become much more effective and dominate ^{4}He destruction for $t \gg \tau_\alpha$.

For $t \gg \tau_\alpha$ when $p + \alpha$ is the dominant ^{4}He distraction process, thus the ^{4}He distraction rate is give by

$$\dot{n}_\alpha = R_\alpha^t \times n_p \times n_\alpha$$

The solution of which is:

$$n_\alpha(t) = n_\alpha^0 \times \exp\left(-\frac{t}{\tau_\alpha}\right),$$

where n_α^0 is the initial ^{4}He number density and τ_α is the ^{4}He destruction time-scale.

The first generation (G1) products of the $\alpha + \alpha$ reactions for $t \gg \tau_\alpha$ will start to decline due to ^{4}He destruction; therefore, we have:

$$\dot{n}_{G1} = R_{G1}\frac{n_\alpha^2}{2} = \left(\frac{R_{G1}}{R_\alpha^t}\right) \times \left(\frac{n_\alpha^0}{2\,\tau_\alpha}\right) \times \exp\left(-2\,\frac{t}{\tau_\alpha}\right),$$

the integration of which, gives:

$$n_{G1}(t) = \left(\frac{R_{G1}}{R_\alpha^t}\right) \times \left(\frac{n_\alpha^{0\,2}}{4}\right) \times \exp\left(-2\,\frac{t}{\tau_\alpha}\right) = \left(\frac{R_{G1}}{R_\alpha^t}\right) \times \frac{n_\alpha^2(t)}{4}$$

For the second generation (G2) we have:

$$\dot{n}_{G2} = R_{G2} n_\alpha n_{G1} = \left(\frac{R_{G1}}{R_\alpha^t}\right) \times \left(\frac{R_{G2}}{R_\alpha^t}\right) \times \left(\frac{n_\alpha^3(t)}{4\,\tau_\alpha}\right)$$

The solution of which gives $n_{G2} \propto n_\alpha(t)^3$. We can conclude that the N'th generation number density dependence for $t \gg \tau_\alpha$, is $n_{GN} \propto n_\alpha(t)^{N+1}$.

To sum up this analysis, the asymptotic behaviour of the N'th generation products should be:

$$\begin{cases} n_{GN}(t) \propto t^N & : t \ll \tau_\alpha \\ n_{GN}(t) \approx \text{peak value} & : t \sim \tau_\alpha \\ n_{GN}(t) \propto \exp\left(-(N+1) \times \frac{t}{\tau_\alpha}\right) & : t \gg \tau_\alpha \end{cases} \tag{2.19}$$

In other words, the higher the generation is, steeper its abundance raises with time and sharper it falls.

The abundance evolution of a pure ^{4}He plasma for temperatures $k_B T = 1$ MeV and $k_B T = 10$ MeV, is shown in fig. 2.6.

The evolution analysis of the γ-ray spectra

The γ-ray production rate due to a nuclear reaction depends directly on the abundances of the nuclei. The photon production rate is $\dot{n}_\gamma = \langle \sigma \upsilon \rangle_\gamma \; n_1 \; n_2$, where $\langle \sigma \upsilon \rangle_\gamma$ is the Maxwellian average rate of the reaction $1 + 2 \rightarrow \gamma$. The n_1 and n_2 are number densities of species 1 and 2, respectively.

Let us analyse the γ-ray production rate in a pure ^{4}He plasma. These predictions allow us to construct analytically the γ-ray emissivity for every component of the γ-ray spectra, with a rather good accuracy.

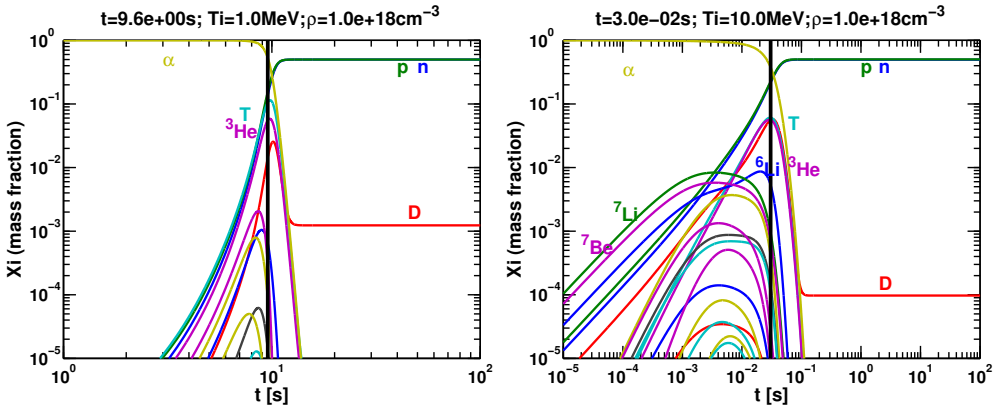

Figure 2.6: The abundance evolution for an initial pure ^{4}He plasma. Here the nucleon number density is fixed $\varrho_u = 10^{18}$ cm^{-3}, and two temperatures are considered $k_BT = 1$ MeV (left) and $k_BT = 10$ MeV (right). The black vertical line represents the moment of time for which the γ-ray spectra in fig. 2.9 is built.

Let us split the plasma evolution into three stages – as we have already done in section 2.4.3. The first stage is during $t < \tau_\alpha$ for which ^{4}He abundance is practically constant. The second stage $t \sim \tau_\alpha$ is the start of ^{4}He destruction. At this period, all generations of nuclei abundances reach their maximum value. The last stage is $t > \tau_\alpha$ during which neither ^{4}He nor other generations of nuclei are present in the plasma. During this period we obtain a proton–neutron plasma.

During the firs stage, the abundance of the ^{6}Li, ^{7}Li and ^{7}Be grow linearly with time; thus, α-particles start to excite them. As a result, the de-excitation lines of ^{6}Li, ^{7}Li and ^{7}Be, start to appear in the plasma spectra together with the excited products of $\alpha + Li/Be$. They all will have the same γ-ray production rate behaviour, i.e. linear increase with time. The reason is $\dot{n}_\gamma = \langle\sigma\upsilon\rangle_\gamma \; n_\alpha \; n_{Li/Be}$, where, $n_{Li/Be} \sim t$.

Following the same logic, the excitation of other generations of nuclei from α-particles will have a γ-ray production rate time dependence identical to the abundance for that given generation.

At the second stage, since all the abundances for all generations reach a maximum, so will the γ-ray production rate do. Whilst for the third period ($t > \tau_\alpha$) when ^{4}He destruction take place, the decline of the γ-ray production rate will be $\dot{n}_\gamma = \langle\sigma\upsilon\rangle_\gamma \; n_\alpha \; n_{GN} \propto \exp\left(-(N+2) \times \frac{t}{\tau_\alpha}\right)$ faster than the abundance of the generation N (n_{GN}). During this last period the γ-ray production rate is dominated by p–n plasma radiation.

To sum all up:

$$\dot{n}_\gamma(t) \propto \begin{cases} \sim n_{GN}(t) \propto t^N & : t \ll \tau_\alpha \\ \sim n_{GN}(t) \approx \text{peak value} & : t \sim \tau_\alpha \\ \sim n_\alpha \times n_{GN}(t) \propto \exp\left(-(N+2) \times \frac{t}{\tau_\alpha}\right) & : t \gg \tau_\alpha \end{cases} \tag{2.20}$$

Figure 2.7 shows the evolution of the production rate for different γ-ray lines.

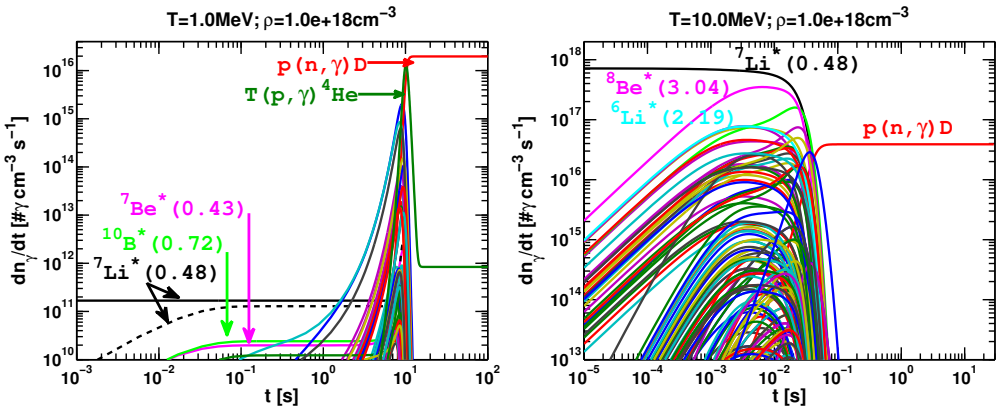

Figure 2.7: Gamma-ray production rates for an initial pure ^{4}He plasma. The plasma has nucleon number density fixed $\varrho_u = 10^{18}$ cm^{-3} and temperatures $k_B T = 1$ MeV (left) and $k_B T = 10$ MeV (right).

If we want to know the γ-ray emissivity at a certain moment of time, the $\dot{n}_\gamma$ shown in fig. 2.7 become very useful. The γ-ray lines will have a peak value ($\Phi^l_{\gamma\max}$) and width (for details see eq. (2.10)) :

$$\Phi^l_{\gamma\max}(t) = \sqrt{\frac{M\,c^2}{2\pi\,k_B\,T}} \times \dot{n}_\gamma(t) \tag{2.21}$$

$$\Delta E_\gamma = \sqrt{\frac{k_B\,T}{M\,c^2}} \times E^0_\gamma \tag{2.22}$$

where $Mc^2 = A \times m_u\,c^2$ is the emitter nucleus mass, with A its mass number and $m_u\,c^2 = 931.5$ MeV the nucleon mass. The E^0_γ is the central γ-ray line energy.

For example, from fig. 2.7 at temperature $k_B T = 10$ MeV and instant $t = 10^{-2}$ s, the production rate of the $E^0_\gamma = 0.478$ MeV line emitted due to de-excitation of ^{7}Li is $\dot{n}_\gamma \approx 6 \times 10^{17}$ cm^{-3} s^{-1}; whereas, for $E^0_\gamma = 3.04$ MeV line produced by ^{8}Be is $\dot{n}_\gamma \approx 4 \times 10^{17}$ cm^{-3} s^{-1}. Hence, the maximum emissivity for these lines will be $\Phi^{0.478}_\gamma \approx 9.8 \times 10^{12}$ erg cm^{-3} s^{-1} MeV^{-1} and $\Phi^{3.04}_\gamma \approx 6.9 \times 10^{12}$ erg cm^{-3} s^{-1} MeV^{-1}; whilst, their widths are $\Delta E^{0.478}_\gamma \approx 0.02$ MeV and $\Delta E^{3.04}_\gamma \approx 0.1$ MeV. Figure 2.8 shows the nuclear line emissivity.

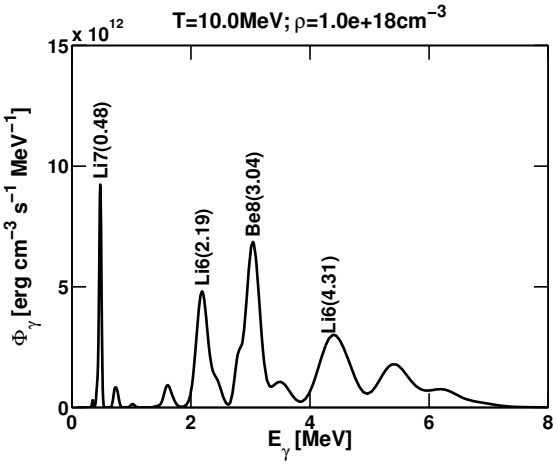

Figure 2.8: Gamma-ray line emissivity for an initial pure ^{4}He plasma with $k_BT = 10$ MeV and at the instant $t = 10^{-2}$ s. The γ-ray line production rate it is shown in fig. 2.7.

Nuclear bremsstrahlung emissivity Φ^b_γ is constant for $E_\gamma \ll k_BT$; whereas, for $E_\gamma \geq k_BT$ it has a sharp decline. Thus, to predict the nuclear bremsstrahlung emissivity it is enough to know the height of the constant part as a function of temperature and density. Note that for a composite plasma with different species of nuclei, we need to include the modification factor to the p–n bremsstrahlung, as it is shown in eq. (2.16).

The constant behaviour of the bremsstrahlung emissivity for $E_\gamma \ll k_BT$, is because the differential cross-section has a $d\sigma/dE_\gamma \propto E_\gamma^{-1}$ behaviour at low E_γ energies. With a good approximation the p–n elastic cross-section is $\sigma^{el}_{pn} \propto E^{-1/2}$ for $0.1 < E < 10$ MeV and $\sigma^{el}_{pn} \propto E^{-1}$ for $10 < E < 400$ MeV. By substituting these information in the eqs. (2.15) and (2.16), we obtain the following formula for the p–n bremsstrahlung emissivity:

$$\Phi^b_\gamma(E_\gamma \ll k_BT) \approx \begin{cases} 8.0\times10^{-25}\ n_p\ n_n\ \theta & : 0.1 < k_B\,T < 2\,\text{MeV} \\ 3.2\times10^{-26}\ n_p\ n_n\ \theta^{1/2} & : 2 < k_B\,T < 100\,\text{MeV} \end{cases}, \qquad (2.23)$$

where $\theta = k_B\,T/m_p\,c^2$ and n_p and n_n are the protons and neutrons number densities, respectively. The Φ^b_γ is in units erg cm^{-3} s^{-1} MeV^{-1}. For $E_\gamma \sim k_BT$, the bremsstrahlung emissivity falls sharply.

The p–n capture on the other hand, has an emissivity that starts from $E_\gamma = Q$, reaches a peak at $E^{\max}_\gamma$ and then declines – where Q is the reaction Q-value.

It is remarkable though, that the $p + n \rightarrow D + \gamma$ capture reaction emissivity maximum does not change noticeably for a wide range of temperatures. The emissivity changes from $\Phi^c_\gamma/n_p\,n_n = 1.6\times10^{-25}$erg cm^3 s^{-1} MeV^{-1} to $\Phi^c_\gamma/n_p\,n_n = 1.3\times10^{-25}$erg cm^3 s^{-1} MeV^{-1} when the temperature changes from $k_BT = 1$ MeV

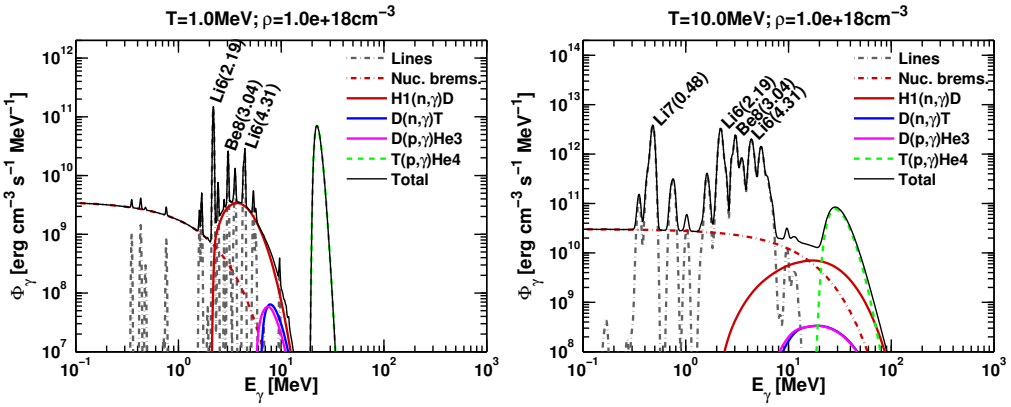

Figure 2.9: Gamma-ray spectra for an initial pure ^{4}He plasma. The abundance evolution for this plasma is shown in the fig. 2.6. The spectra is constructed at the moment of time shown with a black vertical line in the fig. 2.6. The plasma has nucleon number density $\varrho_u = 10^{18}$ cm^{-3} and temperatures $k_BT = 1$ MeV (left) and $k_BT = 10$ MeV (right).

to $k_BT = 200$ MeV, respectively. Thus, with a good accuracy, the emissivity peak value can be considered independent of temperature. Hence, the emissivity peak value and its photon energy is given by:

$$\Phi^c_{\gamma\max} \approx 1.5\times10^{-25}\times n_p\, n_n \quad \left[\mathrm{erg\,cm^{-3}\,s^{-1}\,MeV^{-1}}\right] \tag{2.24}$$

$$E^{\max}_\gamma \approx Q + \frac{3}{2}\,k_B\,T \tag{2.25}$$

Here $Q = 2.225$ MeV is the Q-value of the $p + n \to D + \gamma$ capture reaction. The γ-ray energy at the maximum emissivity is found by differentiating eq. (2.15) with respect to E_γ.

The width of the capture emissivity spectra at the half maximum is of the order $\Delta E_\gamma \sim 2\times E^{\max}_\gamma$. Figure 2.5 shows the p–n spectra for different temperatures. There $n_p = n_n = 0.5\times10^{18}$ cm^{-3}.

Figure 2.9 shows the emissivity from different components for the solutions that are shown in fig. 2.6. The spectra are constructed for the instant when the plasm starts to destroy ^{4}He, for which all other generations abundances have reached their maximum.

The spectrum in fig. 2.9 is dominated by nuclear lines, in particular the lines that come from the de-excitation of the first generation of nuclei. We can clearly see there the p–n bremsstrahlung and capture continuum radiation. Moreover the continuum radiation of the $p + T \to {}^4\mathrm{He} + \gamma$ with Q-value $Q = 19.8$ MeV dominates because of the large amount of the T at that particular moment of time. However, the cross-section for this reaction is poorly known experimentally; thus, the result must be taken with caution.

2.4.4 Hydrogen and Helium mixed plasma

Let us consider an initial plasma with $X_p = X_\alpha = 0.5$. The dominant nuclear reactions in such plasma are $p + \alpha$ and $\alpha + \alpha$. At temperature $k_B T = 1$ MeV the $\alpha + \alpha$ reactions are not as effective as the $p + \alpha \rightarrow D + {}^3\mathrm{He}$, because the $\alpha + \alpha$ reactions have a higher threshold energy.

The hydrogen-helium mixed plasma differs from the pure hydrogen or pure helium plasma due to $p + \alpha \rightarrow D + {}^3\mathrm{He}$ reaction as well as due to the reactions of p and α-particles with the $p + \alpha$ and $\alpha + \alpha$ reaction products. Another difference of H-He plasma from the pure helium one, is the ${}^4\mathrm{He}$ destruction time-scale τ_α. For the mixed plasma, the ${}^4\mathrm{He}$ destruction time-scale is shorter, because protons are present from an earlier stage; thus, increasing the ${}^4\mathrm{He}$ destruction efficiency.

Figure 2.10 shows the chemical evolution of the H-He plasma for temperatures $k_B T = 1$ and 10 MeV. The γ-ray spectra are also constructed therein, at the instant when ${}^4\mathrm{He}$ destruction starts to take place.

The discussion about the chemical evolution and γ-ray production rate (cf. sections 2.4.3 and 2.4.3) applies here as well. Figure 2.10 shows that the products of the $p + \alpha$ and $\alpha + \alpha$ reactions, rise linearly with time, peak at the moment of ${}^4\mathrm{He}$ destruction and then fall down exponentially. The γ-ray spectra will be dominated by the nuclear lines from the Li and Be isotopes. These isotopes are produced in an excited state from $\alpha + \alpha$ reactions, or get excited from p or α particles. After ${}^4\mathrm{He}$ is destroyed, the plasma becomes a p–n plasma.

2.4.5 A proton-heavy element mixed plasma

Now we consider a plasma that is initially composed by hydrogen and elements heavier than ${}^4\mathrm{He}$. Here is investigated the plasma evolution for two fixed-temperatures, 1 and 10 MeV. The elements that are considered here, are: ${}^{12}\mathrm{C}$, ${}^{28}\mathrm{Si}$ and ${}^{56}\mathrm{Fe}$. Their initial mass fraction abundances are:

1. $X_p = 0.7$ and $X_{{}^{12}\mathrm{C}} = 0.3$
2. $X_p = 0.7$ and $X_{{}^{28}\mathrm{Si}} = 0.3$
3. $X_p = 0.7$ and $X_{{}^{56}\mathrm{Fe}} = 0.3$

This is equivalent of having a plasma with $n_p = 7 \times 10^{17} \mathrm{cm}^{-3}$ and $n_{{}^{12}\mathrm{C}}/n_p = 3.6\ 10^{-2}$, $n_{{}^{28}\mathrm{Si}}/n_p = 1.53\ 10^{-2}$, and $n_{{}^{56}\mathrm{Fe}}/n_p = 7.7\ 10^{-3}$, respectively. Since $n_{\mathcal{X}}/n_p < 0.1$ for these cases, we can neglect the ${}^{12}\mathrm{C} + {}^{12}\mathrm{C}$, ${}^{28}\mathrm{Si} + {}^{28}\mathrm{Si}$ and ${}^{56}\mathrm{Fe} + {}^{56}\mathrm{Fe}$ reactions (cf. appendix A).

The plasma evolution period is 100 s and its temporal composition evolution and the γ-ray lines production rate, are shown in figs. 2.11, 2.13 and 2.15.

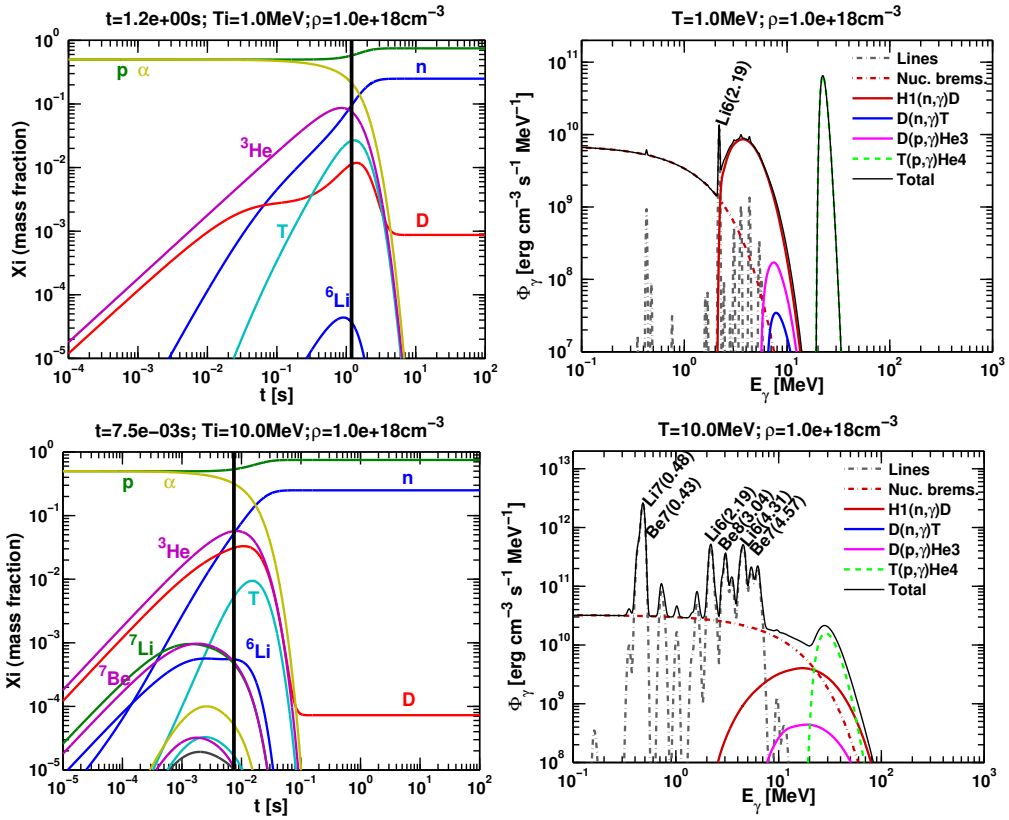

Figure 2.10: Chemical composition evolution and emissivity of an initial $p-\alpha$ mixed plasma. The initial mass fraction abundances are $X_p = X_\alpha = 0.5$. The nucleon number density is fixed $\varrho_u = 10^{18}$ cm^{-3}, and two temperatures are considered: $k_BT = 1$ and 10 MeV. The figures on the left show the chemical evolution for the two temperatures; whereas, the right side shows the emissivity spectra built at the instant marked with the black vertical line in the respective chemical evolution plot.

The γ-ray spectra are also constructed in figs. 2.12, 2.14 and 2.16. Two characteristic periods are considered for its construction: The period before and during the destruction of the element under consideration. The γ-ray spectra of the period when the heavy element is fully destroyed, matches the p–n plasma γ-ray spectra, which is already shown in section 2.4.2. In appendix E, some cross-sections with their respective rates are shown for some intensive γ-ray lines of some important elements.

2.4.6 Solar composition plasma

Now we consider a plasma with initial solar composition. Let the nucleon number density and the temperature be fixed to $\varrho_u = 10^{18}$ cm^{-3} and $k_BT = 10$ MeV, similar to the examples above. The evolution of such a plasma will have three stages. The first period lasts until all "metallic" nuclei are

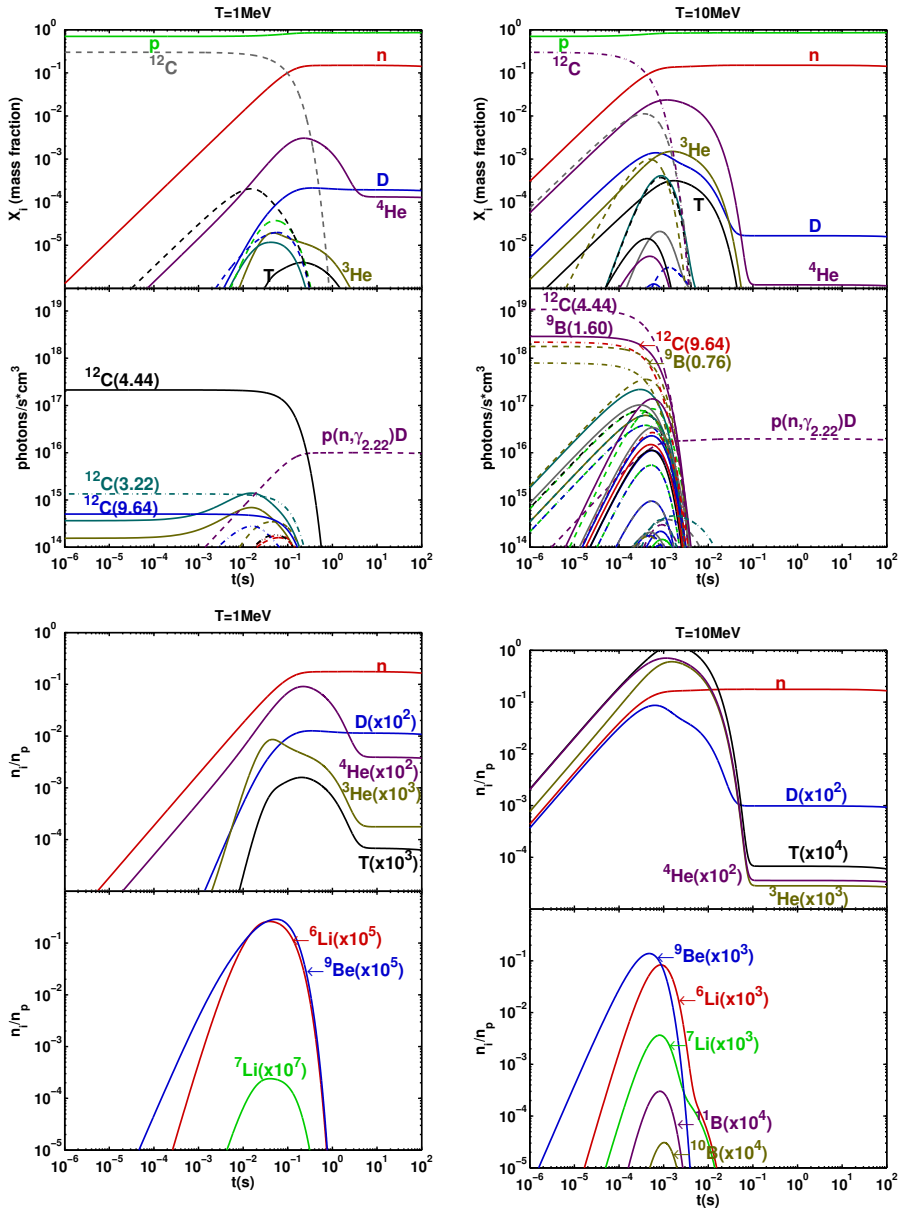

Figure 2.11: Temporal evolution of mass fraction abundances and γ-ray line emission for a plasma with initial mass composition of 70% protons and 30% ^{12}C, for temperatures 1 MeV (left) and 10 MeV (right). In each case, the bottom panels show in particular the evolution of the abundance of light elements up to ^{11}B, multiplied by the coefficient in brackets for comparison.

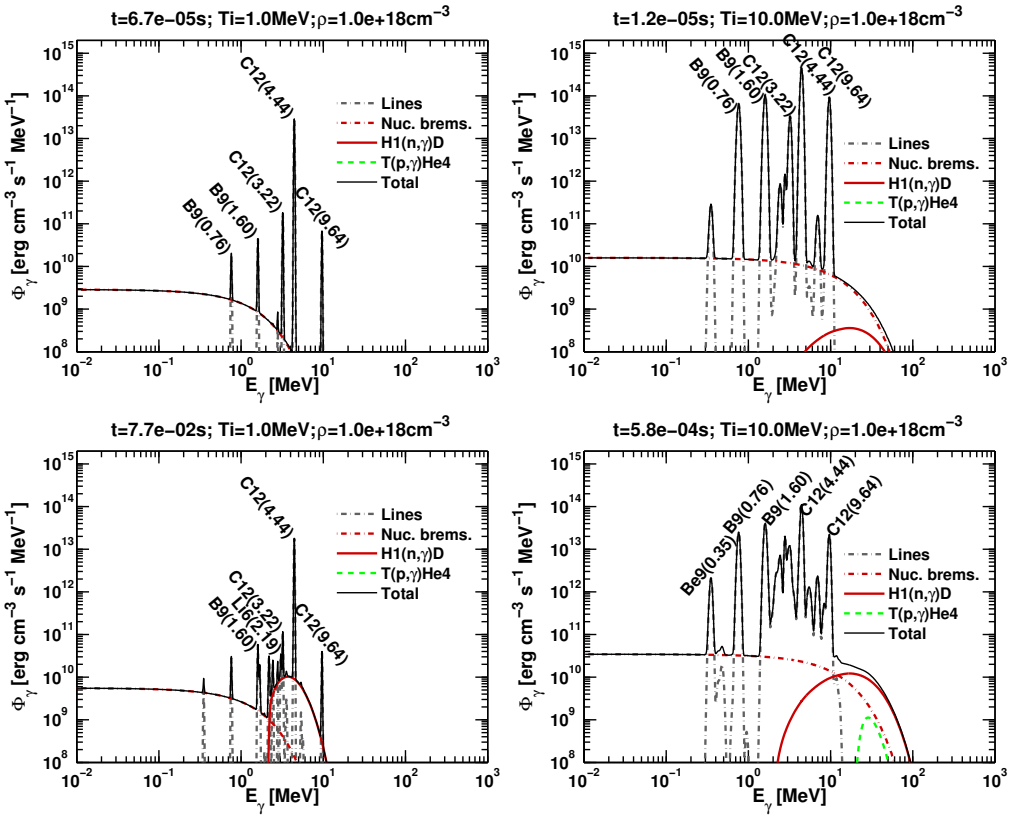

Figure 2.12: Gamma-ray spectra of a plasma with initial composition of 70% protons and 30% ^{12}C, for temperatures 1 MeV (left) and 10 MeV (right). The spectra are built for two instance of evolution belonging to the period before and during the ^{12}C destruction.

destroyed. The second period lasts until ^{4}He is destroyed and the third period is when the p–n plasma forms. Figure 2.17 shows the abundance temporal evolution for such plasma. There the γ-ray emissivity is also constructed for the first period. The other two periods of this plasma will have the same spectra as the H-He and p–n plasma in their respective periods.

2.4.7 Temperature and/or density time dependence plasma

All the above examples had a fixed temperature and density. Moreover, their evolution period has been shorter than the neutron decay lifetime. Here we cover these two interesting cases with two examples.

For the first example consider a plasma with fixed temperature and nucleon number density ($\varrho_u = 10^{18}$ cm^{-3}), over the entire solution interval $\Delta t = 10^4 \gg \tau_n \approx 880$ s.

To a first-order approximation, the result of the evolution of a low-density, high-temperature plasma over time-scales larger than one second is a system

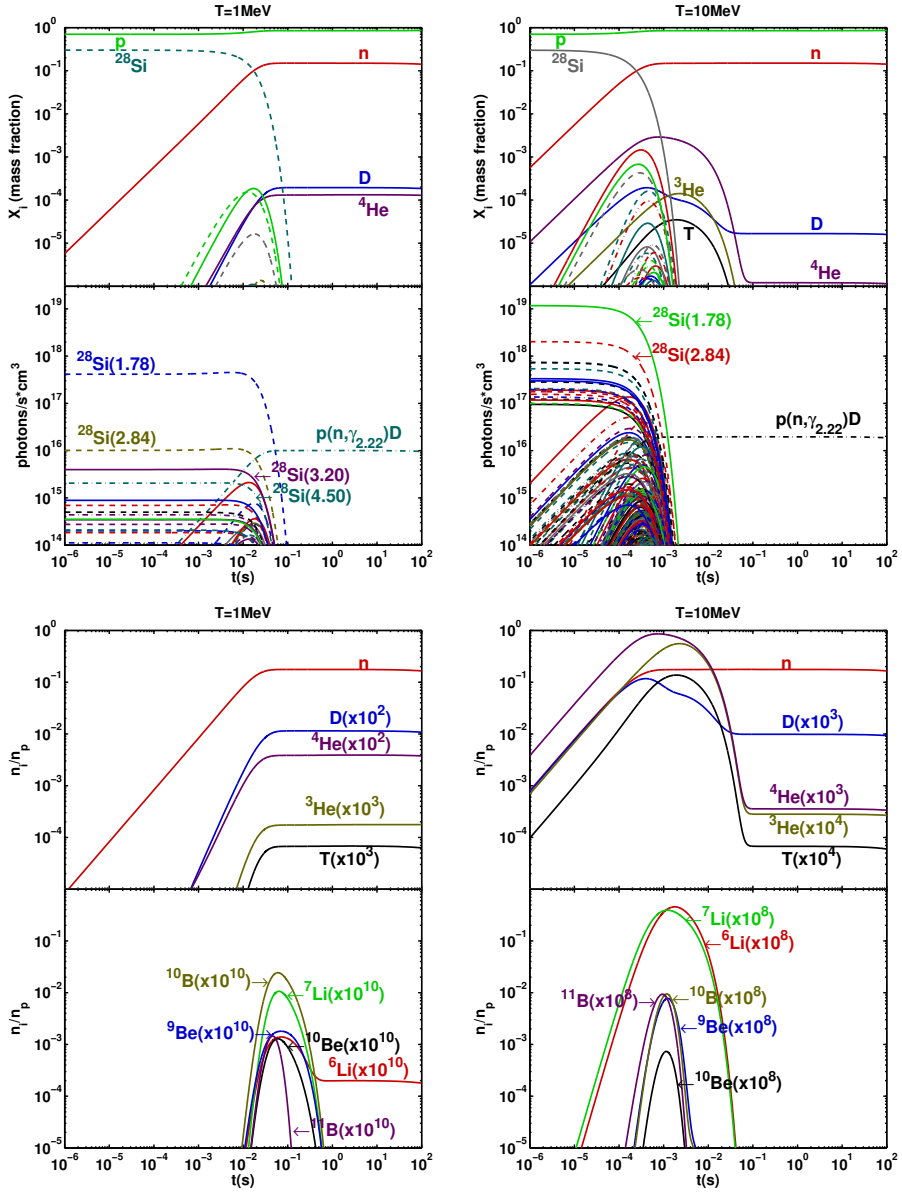

Figure 2.13: Temporal evolution of mass fraction abundances and γ-ray line emission for a plasma with initial mass composition of 70% protons and 30% ^{28}Si, for temperatures 1 Mev (left) and 10 MeV (right). In each case, the bottom panels show in particular the evolution of the abundance of light elements up to ^{11}B, multiplied by the coefficient in brackets for comparison.

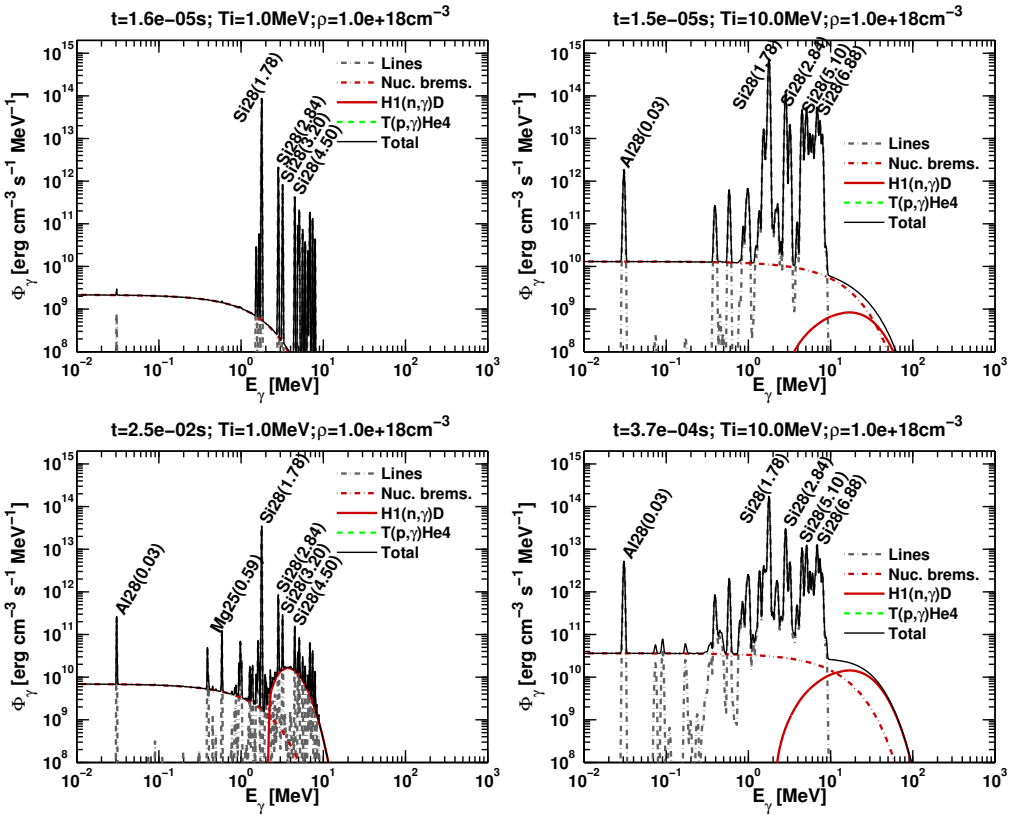

Figure 2.14: Gamma-ray spectra of a plasma with initial composition of 70% protons and 30% ^{28}Si, for temperatures 1 MeV (left) and 10 MeV (right). The spectra are built for two instances of evolution belonging to the period before and during the ^{28}Si destruction.

formed by protons and neutrons. If the plasma temperature is $k_BT \lesssim 20$ MeV, the p–n interactions are feeble to keep free neutrons from decay; thus, for time-scales larger than neutron lifetime the p–n plasma will consist of a pure proton plasma. If the temperatures are higher than 20 MeV then the π-meson production serves as a coupling between protons and neutrons and the plasma will tend to evolve towards an equal amount of protons and neutrons. This symmetric behaviour has its roots in the isospin symmetry which was assumed earlier cf. section 2.2.2.

Figure 2.18 left, shows the evolution of a plasma initially composed with $X_p = 0.7$ and $X_{Fe} = 0.3$ at temperature $k_BT = 10$ MeV. After neutrons start to decay, this plasma becomes a proton plasma; as a result, it becomes "darker" (low fluxes of γ-rays). If the plasma temperature will be high enough to produce π-meson, then neutrons will be in equilibrium with protons

The second example considers the plasma temperature as a function of time. If plasma temperature increases with time, it will facilitate the destruction processes and result to a p–n plasma. However, the most in-

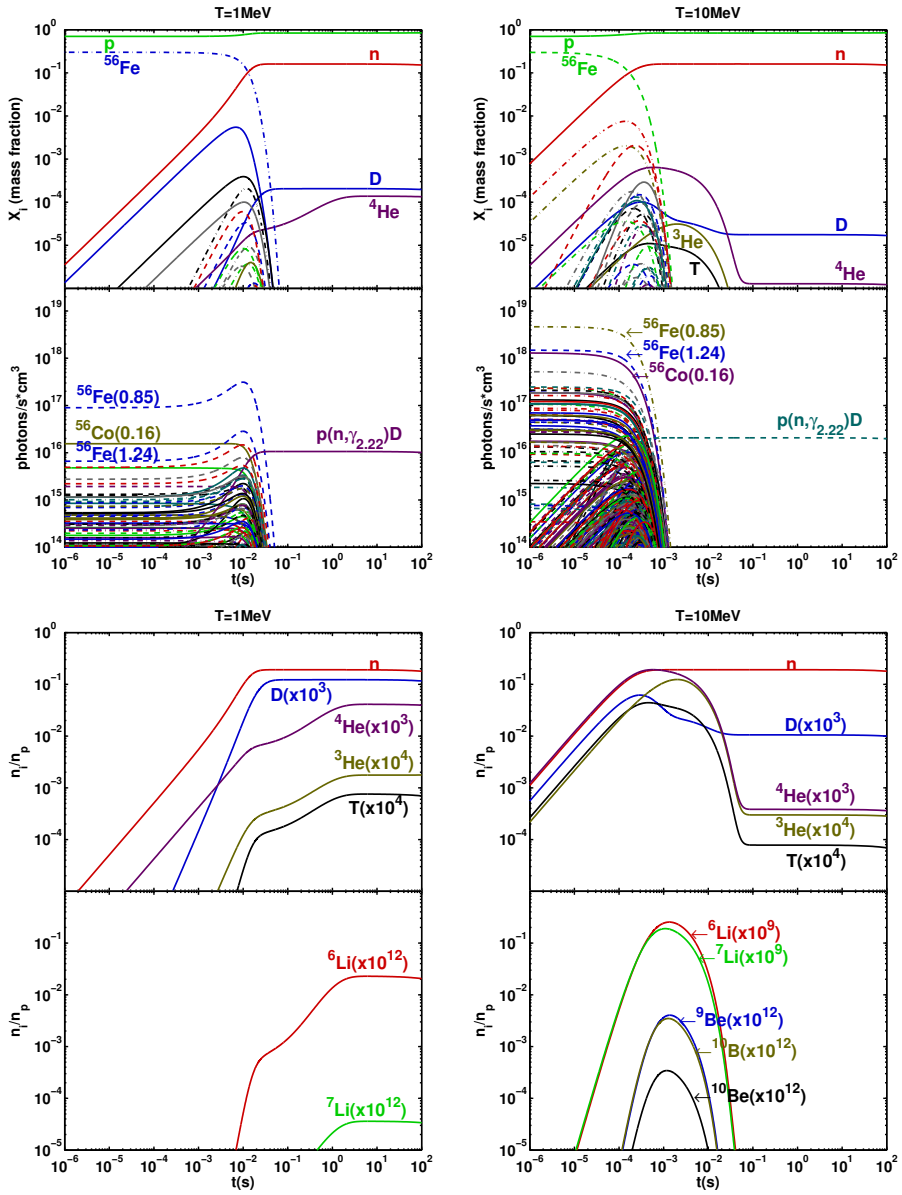

Figure 2.15: Temporal evolution of the mass fraction abundances and γ-ray line emission for a plasma with initial mass composition 70% protons and 30% ^{56}Fe, for temperatures 1 Mev (left) and 10 MeV (right). In each case, the bottom panels show in particular the evolution of the abundance of light elements up to ^{11}B, multiplied by the coefficient in brackets for comparison.

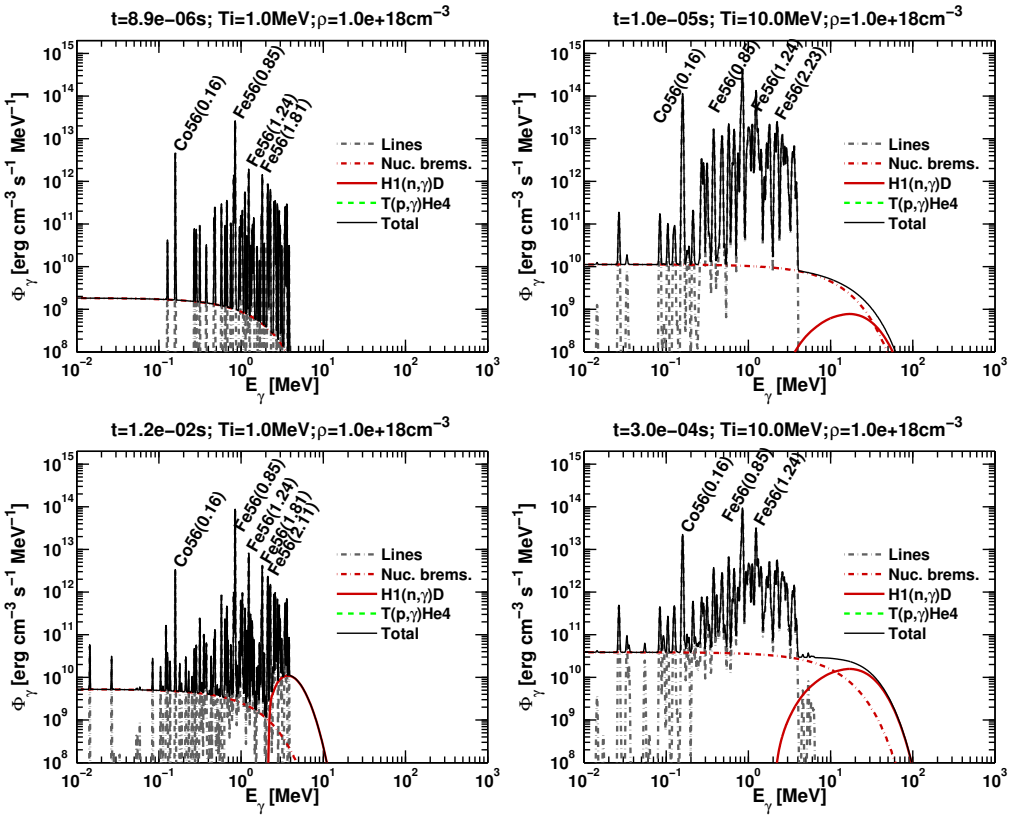

Figure 2.16: Gamma-ray spectra of a plasma with initial composition of 70% protons and 30% ^{56}Fe, for temperatures 1 MeV (left) and 10 MeV (right). The spectra are built for two instance of evolution belonging to the period before and during the ^{56}Fe destruction.

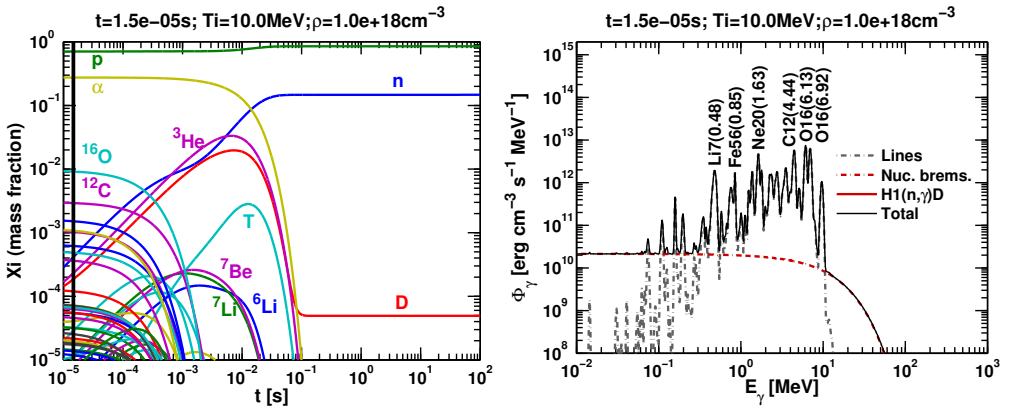

Figure 2.17: The solar composition plasma temporal evolution. The nucleon number density is $\varrho_u = 10^{18}$ cm^{-3}, and the temperatures is $k_BT = 10$ MeV. The figure on the left shows the chemical evolution; whereas, on the right is shown the emissivity spectra built at the instant marked with the black vertical line in the chemical evolution plot.

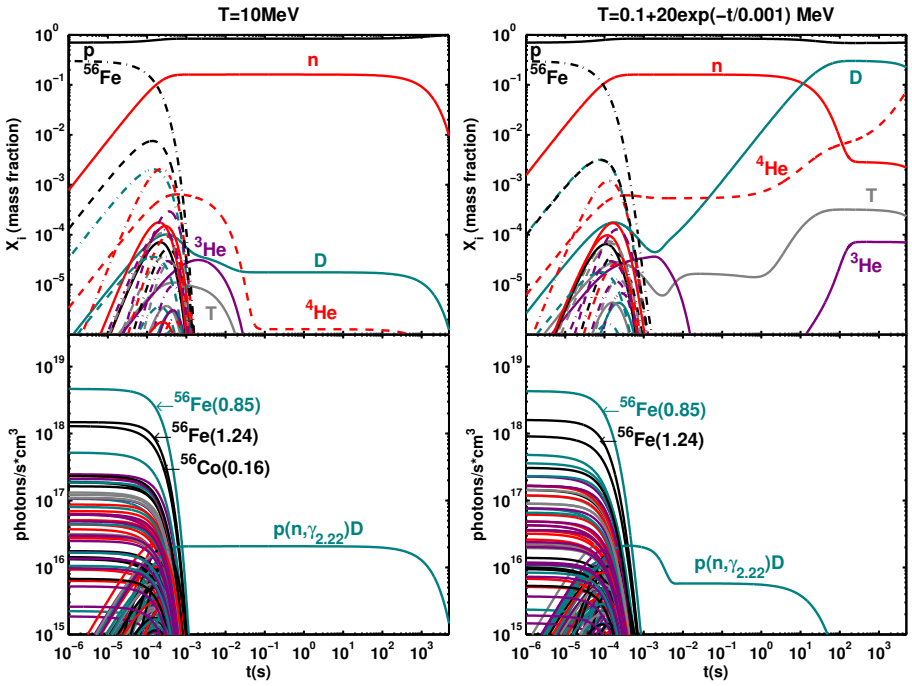

Figure 2.18: The temporal evolution of the mass fraction abundances and the γ-ray line, emission for a plasma with initial composition of 70% protons and 30% ^{56}Fe, for constant temperature 10 MeV (left), and for time dependent temperature $T = 0.1 + 20\exp(-t/0.001)$ MeV (right).

teresting case is when the plasma cools down very quickly i.e. the cooling time-scale is comparable or shorter than the nuclear destruction time-scale. If plasma temperature becomes too low, the nuclear reactions "freeze out". Under these conditions many light and intermediate-mass elements can form. The same phenomenon could occur if the density and/or pressure are instantaneously lowered, such as in the case of free expansion.

The temporal dependence of the temperature adopted here is of the form $T = 0.1 + 20\exp(-t/\tau_\Delta)$ MeV, where $\tau_\Delta = 10^{-3}$ s. Due to the added complexity and computational expenses, the network computes reaction rates down to $T = 0.1$ MeV.

2.4.8 Using the nuclear network for Monte-Carlo simulations

The applicability of the nuclear network described here can be extended to applications that require Monte-Carlo simulations. Astrophysical problems such as: Evaporation of neutrons from a very hot and non-fully-thermalized plasma; Radiation emitted due to neutron's transport along a star atmosphere or a cloud, or the transport of accreted matter into a neutron star atmosphere – are examples where one may need both Monte Carlo simula-

tions and nuclear physics.

These problems however, go beyond the scope of this thesis and are thus not discussed here. Nevertheless, I show here a simple example where the nuclear network is used with a Monte-Carlo method to simulate the destruction of a given nucleus.

In section 2.2.3, it was discussed how to built a nuclear network. The rate threshold that was suggested there was $R^{\rm th} = 10^{-19}$ cm^3 s^{-1}. Although, this is a reasonable choice for problems related with plasma chemical composition and γ-ray spectra, for other problems such as the Monte-Carlo methods, it is not sufficient.

Consider a unit volume of plasma made of e.g. pure protons with temperature $k_B T = 10$ MeV and number density fixed to $\varrho = 10^{18}$ cm^3. Let us throw nuclei into this plasma e.g. ^{56}Fe, and lets track how these nuclei "dissolve" with time. These simulations require a network that has many more channels than the one we have used so far in the other examples. I have constructed a nuclear network with a threshold rate $R^{\rm th} = 10^{-20}$ cm^3 s^{-1}. Figure 2.19 shows some possible dissolving paths of a ^{56}Fe nucleus in a proton soup during 100 collisions.

Consider again the above example but replacing the proton plasma with a neutron one. The fig. 2.20 shows some possible dissolving paths of a ^{56}Fe nucleus in a neutron soup during 100 collisions.

2.5 Summary and Discussion

The main purpose of this chapter was to develop a nuclear reaction network that works for temperatures $k_B\,T > 1$ MeV. All the tools are explained in details and a numerical code that produce, manage and solve the nuclear network, is built. The nuclear network is validated through different examples for which the chemical evolution and the γ-ray emissivity are calculated, see sections 2.4.1 to 2.4.8.

These examples allow us to draw some general inferences about how the abundances behave with time and how the γ-ray spectra look like at a certain moment during the plasma evolution. Plasma that is composed initially of e.g. a solar composition, will evolve in three distinct stages. The first stage lasts until elements heavier than ^{4}He are destroyed, the second stage lasts until the ^{4}He is destroyed; finally, in the third stage plasma is composed of protons, neutrons and some traces of light elements such as deuterium.

During the first stage $t \ll \tau_{\mathcal{A}}$, the abundances of the heavy elements are almost constant – the $\tau_{\mathcal{A}}$ is the destruction time scale of a given element $\mathcal{A}$. Therefore, the interactions $p + \mathcal{A}$ and $\alpha + \mathcal{A}$ will produce some first generation

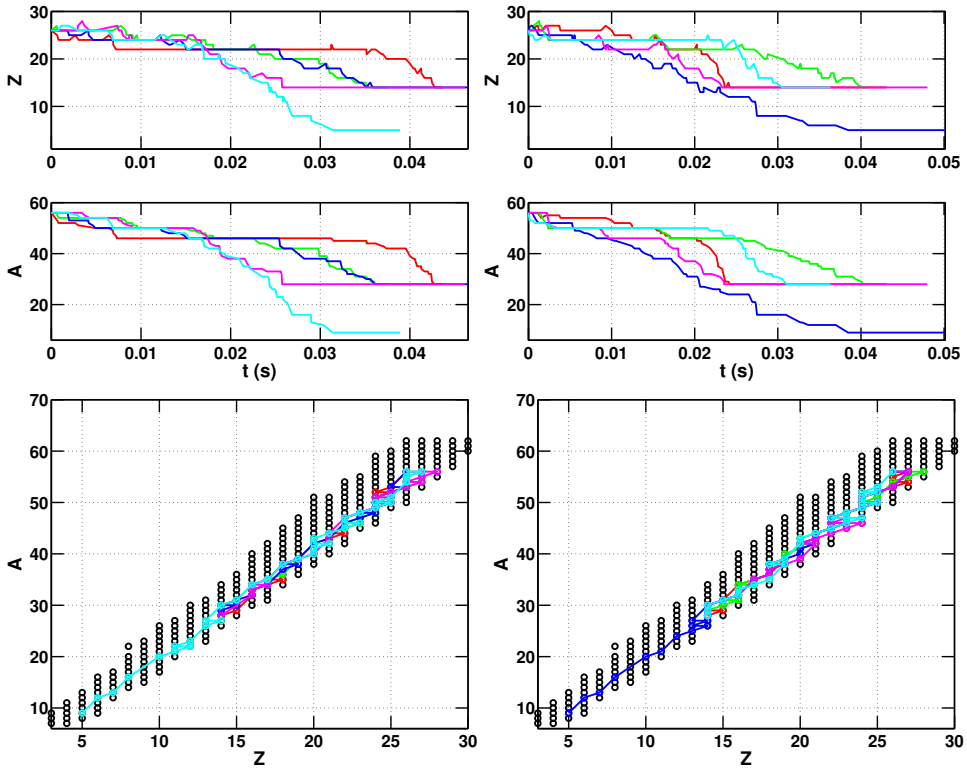

Figure 2.19: Disintegration paths of a ^{56}Fe nucleus in a proton plasma with $k_BT = 10$ MeV and $\varrho = 10^{18}$ cm^3. Figures on the left show five paths and on the right five more. Paths with one color shows the evolution of one single ^{56}Fe nucleus during 100 collisions. The figures show how charge number Z and mass number A change with time, as well as the evolution in the $Z - A$ plane is shown.

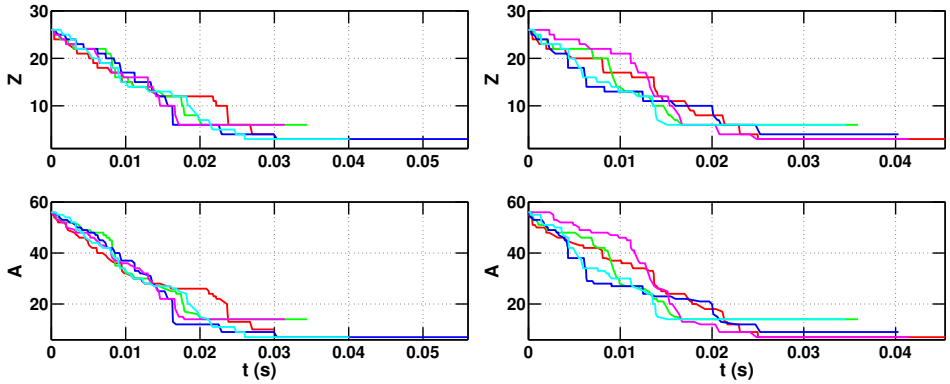

Figure 2.20: The dissolving paths of a ^{56}Fe nucleus in a pure neutron plasma with $k_BT = 10$ MeV and $\varrho = 10^{18}$ cm^3. Figures on the left shows five paths and on the right five more. Paths with one color shows the evolution of one single ^{56}Fe nucleus during 100 collisions. The figures show how charge number Z and mass number A change with time.

of nuclei. This first generation abundance will increase linearly with time ($X_{G1} \propto t$) because abundances of p or α-particles and nucleus $\mathcal{A}$ are constant.

When the first generation of nuclei become abundant enough they can produce a second generation of nuclei by interacting with protons and α-particles. The abundance for the second generation depends quadratically on time ($X_{G2} \propto t^2$). The second generation can also interact with protons or α-particles and generate a third generation, and so on and so forth. For a generation N the abundance will increase as $X_{GN} \propto t^N$ for $t \ll \tau_{\mathcal{A}}$. Therefore, higher the generation of an element in a reaction chain is, steeper its abundance increases with time.

All these generations abundances will increase with time until $t \sim \tau_{\mathcal{A}}$. At this moment the abundances of each generation reach a maximum. For $t > \tau_{\mathcal{A}}$ the element $\mathcal{A}$ abundance start to drop exponentially. At this moment all its generations abundances drop like $X_{GN} \propto X_{\mathcal{A}}^{N+1}(t)$.

This analysis allows us to study the evolution of different generations. To summarize, higher the generation of an element is, steeper its abundance increases and sharper it falls.

During the second stage, all elements heavier than ^{4}He and their intermediate elements disappear. The remnant of the heavy elements are some isotopes of hydrogen and helium. For $t \ll \tau_\alpha$ – where τ_α is the ^{4}He destruction time scale – the abundance of ^{4}He as well as that of protons are constant. Therefore, the abundances of the $p + \alpha$ and $\alpha + \alpha$ reactions products will increase linearly with time. This first generation will interact with p or α and produce a second generation. The second generation abundance will depend quadratically on time. Further increase in the second generation abundance can produce a third generation of elements, etc.

When $t \sim \tau_\alpha$ then all generations that were initiated by ^{4}He will peak. For $t > \tau_\alpha$ the ^{4}He abundance drops exponentially; thus, other generation abundances will drop like $X_{GN} \propto X_\alpha^{N+1}(t)$, see eq. (2.19). The second stage of the plasma evolution looks qualitatively similar to the first stage, except that the source of the chain of the intermediate elements is ^{4}He.

At the last stage $t \gg \tau_\alpha$, a neutron–proton plasma is formed. In a such plasma there are some traces of the hydrogen and helium isotopes that coexist with protons and neutrons. The reason is the weak fusion which equilibrate the destruction processes. The most abundant of these isotopes is deuterium. The deuterium equilibrium abundance depends on the plasma temperature and whether or not the plasma is able to produce π-mesons.

The γ-ray lines are produced through de-excitation of nuclei. A given nuclear reaction can either excite a given nucleus or it can produce a daughter nucleus in an excited state. In both cases the γ-ray line production rate $\dot{n}_\gamma$ will have the same behaviour. If however, a given γ-ray is produced by the N'th

generation reactions, then $\dot{n}_\gamma \propto n_{GN}(t) \propto t^N$ for $t \ll \tau_{\mathcal{A}}$. The $\dot{n}_\gamma$ will peak when abundances of all generations reach their maximum, i.e. $t \sim \tau_{\mathcal{A}}$. However, it will decline sharper than the N'th generation abundance, $\dot{n}_\gamma \propto n_{\mathcal{A}}(t) \times n_{GN}$ for $t \gg \tau_{\mathcal{A}}$, cf. eq. (2.20).

The γ-ray line emissivity is proportional to the γ-ray line production rate $\dot{n}_\gamma$; therefore, the evolution of the γ-ray line emissivity Φ^l_γ, will be identical to the $\dot{n}_\gamma$. The p–n capture and bremsstrahlung are proportional to $\propto n_p \times n_n$; thus they will evolve in the same way as the neutron abundance.

The three stages of plasma chemical evolution are reflected in the γ-ray emissivity spectra. At the first stage, when the plasma is abundant with elements heavier than ^{4}He, intensive γ-ray lines are radiated. The emissivity of these lines will evolve identical with $\dot{n}_\gamma$. Nuclear bremsstrahlung is the dominant continuum radiation. At the second stage plasma is abundant with $p+\alpha$ and $\alpha+\alpha$ reaction products; thus, the γ-ray spectra are composed of γ-ray lines, nuclear bremsstrahlung of $p-n$ and $p-\alpha$ and capture reactions spectra. The source of nuclear γ-ray lines are basically Li and Be isotopes which are formed through $\alpha+\alpha$ reactions. These isotopes are either produced in an excited state or protons and α-particles interact with these nuclei and excite them. The dominant capture reaction in this stage is the $p+n \rightarrow D+\gamma$; however, intermediate elements such as D and T reach their maximum abundance at $t \sim \tau_\alpha$. Therefore, capture reactions such as $p+D \rightarrow {}^3\mathrm{He}+\gamma$, $n+D \rightarrow T+\gamma$ and $p+T \rightarrow {}^4\mathrm{He}+\gamma$ become significant.

At the last stage γ-ray spectra are dominated by the continuum radiation of p-n bremsstrahlung and capture. For temperatures $k_BT > 30$ MeV the $p+p$ interactions produce π-mesons. Thus the γ-ray spectrum has an additional component due to $\pi^0 \rightarrow 2\gamma$ decay. This component was not included here because the next chapter is dedicated to it.

The destiny of a long-lived (i.e., $t > \tau_n$), constant density and temperature $k_BT < 20$ MeV plasma, is a purely protonic composition. This is due to the β-decay of free neutrons into protons, and as a result no other element will remain in equilibrium. Aharonian and Sunyaev (1984) suggested a "neutron evaporation" mechanism for very hot accretion disk around a black hole through which a fraction of the neutrons escape and transforming the accretion disk in an astrophysical neutron source. The neutrons might be captured by surrounding (relatively) cold(er) material such as hydrogen and form deuterium, emitting 2.22 MeV γ-rays. The observation of this spectral line would serve to reveal the existence of the nearby neutron source.

Plasmas which for some reason are cooled to such an extent that reactions are "frozen" at the right moment in time, could produce a higher abundance of intermediate elements (and therefore light elements). Such a scenario could be related with shock waves formed during a supernova

explosion. Since supernova explosions are ubiquitous in the universe, this mechanism could, in principle, change cosmic abundances.

I conclude that the use of the nuclear reaction network that was suggested here can be extended to other applications such as the Monte Carlo applications.

3 The non-developed Maxwellian distribution plasma

3.1 Motivation

Very hot astrophysical plasmas with temperatures $k_B T > 20$ MeV start to produce π^0-mesons through inelastic p–p collisions. The decay of π^0-meson leads to two high energy γ-rays. The importance of this process as a source of γ-rays in hot accretion plasma around black holes has been recognized long ago (e.g. Dahlbacka et al., 1974; Kolykhalov and Syunyaev, 1979; Giovannelli et al., 1982; Aharonian and Atoyan, 1983; Dermer, 1986).

The π^0 production cross-section through p–p inelastic collisions has a kinematic threshold at $E_k \approx 2\, m_\pi\, c^2 \approx 280$ MeV – m_π is the π^0 mass. Thus, a thermal proton plasma with temperature below $k_B T < 100$ MeV is able to produce π^0 only through high energy protons ($E \gg k_B T$) that populate the distribution tail. As a result, the π^0 production is very sensitive to the shape of the distribution tail.

Typically, a thermal plasma is described by a Maxwellian distribution. In real astrophysical plasmas however, full thermalization – i.e. fully developed Maxwellian tails – may not establish. The reasons could be short lifetime of plasma or some acceleration processes. In the first case ions do not have enough time to interact and exchange momentum and energy, thus the plasma will not be able to develop a tail. In the second case, even slight acceleration of particles may result in deviation of the distribution tail.

Astrophysical situations where full thermalization may not take place, are for instance Advection Dominated Accretion Flows (ADAF) regimes (e.g. Narayan and Yi, 1994). For these accretion regimes, the plasma falling time is shorter than the time required to develop the ion's Maxwellian tail. Thus, the γ-ray spectra due to π^0 production from these objects can differ substantially compared to the case of developed Maxwellian distribution.

Recent reports by Fermi collaboration of variable γ-ray sources with soft energy spectra can be result of π^0 production and decay in hot accretion flows

onto relativistic compact objects such as black holes or neutron stars. The very hot plasma of such objects may not be able to develop the Maxwellian distribution tail which would affect the π^0 production

Hence, it is of great practical interest to investigate the γ-ray production in such plasmas. There are two main component that influence the π^0 production and its γ-ray spectra. The first is related to the p–p inelastic collisions close to the kinematic threshold and the second component is related with distribution tail of the ion component of the plasma.

3.2 The $pp \rightarrow pp\pi^0$ cross-section

Many experiments have been performed to measure the $pp \rightarrow \pi^0$ production close to the kinematic threshold (e.g. Shimizu et al., 1982; Meyer et al., 1990, 1992; Stanislaus et al., 1991; Bondar et al., 1995; Machner and Haidenbauer, 1999; Agakishiev et al., 2012). The cross-section $\sigma_{pp\pi^0}$ shows a rapid increase from the kinematic threshold $E_k \approx 0.28$ GeV until a proton kinetic energy around 0.85 GeV. For proton kinetic energies between 0.85 and 2.5 GeV, the data show approximately constant cross-section with a value 4 mb. A good fit to low energy data below 1 GeV can be found in Dermer (1986). Moreover, the latter for proton energies higher than 1 GeV start to significantly exceed the experimental data. In the calculation here we will assume a constant cross-section of $\sigma_{pp\pi^0} = 4$ mb for $0.85 < E_k < 2.5$ GeV, i.e we will use:

$$\sigma_{pp\pi^0} = \begin{cases} 0 & : 0 < p_p \leq 0.77654\, GeV/c \\ 0.032\eta^2 + 0.04\eta^6 + 0.047\eta^8 & : 0.77654 < p_p \leq 0.96\, GeV/c \\ 32.6(p_p - 0.8)^{3.21} & : 0.96 < p_p \leq 1.27\, GeV/c \\ 5.40(p_p - 0.8)^{0.81} & : 1.27 < p_p \leq 1.53\, GeV/c \\ 4 & : 1.53 < p_p \leq 3.3\, GeV/c \end{cases} , \quad (3.1)$$

where $\sigma_{pp\pi^0}$ is in millibarn (mb) and $\eta = p_\pi^{max}/m_\pi$ as defined in section 2.2.2. In fig. 3.1 the cross-section given by eq. (3.1), the fit suggested by Dermer (1986) and the experimental data (see e.g. Machner and Haidenbauer, 1999; Agakishiev et al., 2012), are compared.

3.3 The π^0 production reaction rate

Following Weaver (1976), in a relativistic plasma the production rate for two plasma species 1 + 2 can be written as:

$$R_{12} = \int dR = \frac{n_1\, n_2\, c}{1 + \delta_{12}} \int \tilde{f}_1(\vec{p}_1)\, \tilde{f}_2(\vec{p}_2)\, \frac{\gamma_r \beta_r}{\gamma_1 \gamma_2}\, \sigma_{12}(\beta_r)\, d^3\vec{p}_1\, d^3\vec{p}_2 \ , \quad (3.2)$$

where n_1 and n_2 are the number densities for the two species 1 and 2 in the laboratory frame; $\vec{p}_1$ and $\vec{p}_2$ are the momenta of two particles; $\tilde{f}_1(\vec{p}_1)$

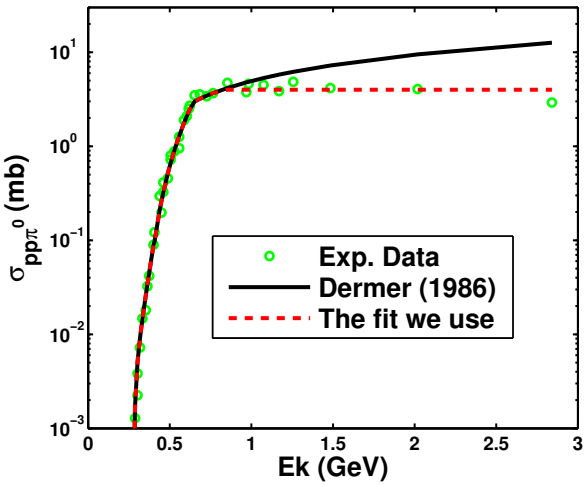

Figure 3.1: The $p+p \rightarrow \pi^0$ production cross-section as a function of proton collision kinetic energy. Circles are the experimental data taken from the (Machner and Haidenbauer, 1999; Agakishiev et al., 2012). Full black line is the fit provided in (Dermer, 1986), red dash-line is the fit that is used in this work.

and $\tilde{f}_2(\vec{p}_2)$ are the momenta distributions of particles 1 and 2; $\sigma_{12}(\beta_r)$ is the interaction cross-section as a function of the collision speed β_r for which the Lorentz factor is defined by $\gamma_r = \gamma_1\gamma_2(1-\vec{\beta}_1\cdot\vec{\beta}_2)$; γ_1 and γ_2 are the protons Lorentz factors and β_1 and β_2 their speeds in the laboratory frame; $\delta_{12} = 1$ if particles 1 and 2 are identical and zero otherwise.

For the $p + p \rightarrow \pi^0$ reaction, the differential production rate can be presented as

$$dR = \frac{n_p^2\, c}{2}\, f_p(\gamma_1)\, f_p(\gamma_2)\, \frac{\sqrt{\gamma_r^2-1}}{\gamma_1\gamma_2}\, \sigma_{pp\pi^0}(\gamma_r)\, d\gamma_1\, d\gamma_2\, \frac{du}{2}\ , \tag{3.3}$$

The γ_1 and γ_2 are the protons Lorentz factors in the laboratory frame; Where $u = \cos(\eta)$, η is the angle between two colliding protons in the laboratory frame. The $\gamma_r = \gamma_1\gamma_2(1-\beta_1\beta_2\, u)$ is the collision Lorentz factor.

3.3.1 π^0 production rate in plasma described by a Maxwellian distribution

In a relativistic fully thermalized plasma, particles have the following distribution

$$f_{MB}(\gamma,\theta) = \frac{\gamma^2\beta}{\theta\, K_2(1/\theta)}\, \exp\left(-\frac{\gamma}{\theta}\right)\ , \tag{3.4}$$

where γ is the Lorentz factor and $\beta = \sqrt{1-\gamma^{-2}}$; $\theta = k_B T/m_p c^2$ is the temperature in units of proton mass; $K_2(x)$ is the modified Bessel function of the second kind.

By inserting eq. (3.4) into eq. (3.3), Weaver (1976) has obtained the following formula for the production rate

$$d\,R(\gamma_r,\theta) = \frac{n_p^2\,c}{2\,(\theta\,K_2(1/\theta))^2}\,\frac{(\gamma_r^2-1)\,K_1\,(z(\gamma_r))}{z(\gamma_r)}\,\sigma_{pp\pi^0}(\gamma_r)\;\;d\,\gamma_r\;\;, \tag{3.5}$$

γ_r is the collision Lorentz factor, $z(\gamma_r) = \theta^{-1}\sqrt{2(\gamma_r+1)}$, and $K_1(x)$ and $K_2(x)$ are the modified Bessel functions of the second kind.

The integration of eq. (3.5) for the cross-section given by eq. (3.1) is shown in fig. 3.2. This figure shows the rate $\langle\sigma\upsilon\rangle = 2R/n_p^2$ (circles) as a function of the plasma temperature. We find a simple analytical fit for the rate:

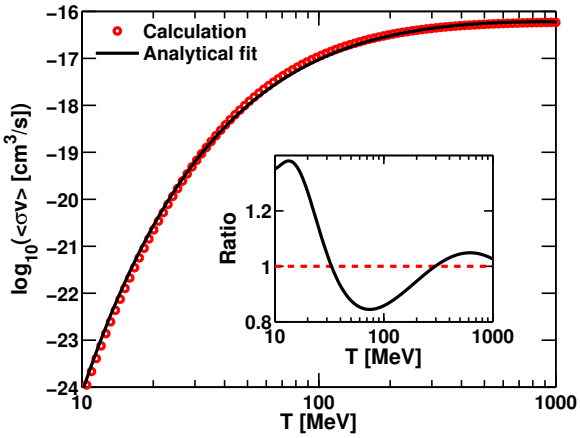

Figure 3.2: The rate $\langle\sigma\upsilon\rangle$ of $p+p\rightarrow\pi^0$ reaction as a function of temperature. The circles are the results from eq. (3.5). The solid line is the analytical fit given by eq. (3.6). The inserted figure shows the ratio between the fit and the numerical calculations.

$$\langle\sigma\upsilon\rangle = 10^{-27}\,c\,\exp\left(\frac{1.3885+1.5835\,\log_{10}(\theta)}{\sqrt{\theta}}\right)\left[\mathrm{cm^3 s^{-1}}\right] \tag{3.6}$$

The analytical fit formula is shown in eq. (3.6) by a solid line. The fit is valid for proton temperatures between 10 MeV and 1 GeV. The accuracy of the fit is better than 20 %, see fig. 3.2.

3.3.2 Deviation from Maxwellian distribution

Below we consider two distinct classes of the distribution tail. The first class is a Maxwellian distribution with a sharp cutoff at a certain energy. We will refer to it as f_{cut} for short. The second class is a Maxwellian distribution where the tail after some given energy is replaced by a power law function. We will refer to this class f_{pl}.

Let us assume an original relativistic Maxwellian distribution $f_{MB}(\gamma,\theta)$, see eq. (3.4). Then the distributions $f_{\rm cut}$ and $f_{\rm pl}$ are presented as

$$f_{\rm cut}(\gamma,\tilde{\theta}) = A\begin{cases} f_{MB}(\gamma,\tilde{\theta}) & : 1 \le \gamma \le \gamma_0 \\ 0 & : \gamma > \gamma_0 \end{cases} \tag{3.7}$$

$$f_{\rm pl}(\gamma,\tilde{\theta},\alpha) = A\begin{cases} f_{MB}(\gamma,\tilde{\theta}) & : 1 \le \gamma \le \gamma_0 \\ B\times E_k^{-\delta} & : \gamma > \gamma_0 \end{cases} \tag{3.8}$$

The constant B is fixed to provide continuity of the distribution function at γ_0; whereas, A and $\tilde{\theta}$ to conserve the total number of particles and the total plasma energy. Thus, they are defined from the following conditions

$$\begin{cases} \int\limits_1^\infty f(\gamma,\tilde{\theta})\,d\gamma = 1 \\ \int\limits_1^\infty (\gamma-1)\,f(\gamma,\tilde{\theta})\,d\gamma = \int\limits_1^\infty (\gamma-1)\,f_{MB}(\gamma,\theta)\,d\gamma \end{cases} \tag{3.9}$$

3.3.3 The π^0 reaction rate in a modified Maxwellian distribution plasma

We calculate here the π^0 production rate $\langle\sigma\upsilon\rangle = 2R/n_p^2$ for three different distributions: pure Maxwellian distribution, Maxwellian distribution with a sharp cutoff and Maxwellian distribution with a power-law tail. The Maxwellian distribution with a sharp cutoff has a cut off at $\gamma_0 = 1 + 3\theta$; whereas the Maxwellian distribution with a power-law tail is formed by replacing the Maxwellian distribution tail from $\gamma_0 = 1 + 3\theta$ to infinity with a power law function with an index $\delta = 2.2$.

Figure 3.3, illustrates how strongly the π^0 production rate is influenced by the distribution tail. The inserted figure shows the ratio of the rates of two modified distributions to the rate corresponding to the pure Maxwellian distribution.

As one may expect, at low temperatures, the Maxwellian distribution with a sharp cutoff has a much smaller rate compared to the pure Maxwellian. The opposite happen to the Maxwellian distribution with a power-law tail $E_k^{-2.2}$ which at low temperatures populate more high energy protons than the pure Maxwellian distribution tail; therefore it has a larger rate.

At higher temperatures, the cut off energy becomes larger ($\gamma_0 = 1+3\theta$) and the Maxwellian part (or the distribution core) of the modified distribution becomes wider. For these reasons, the Maxwellian distribution with a sharp cutoff contains more high energy protons that are able to produce π^0. Thus, its rate becomes comparable to the Maxwellian rate.

For the given normalization, the Maxwellian distribution with power-law tail, at high temperatures contain less particles in its tail compared to

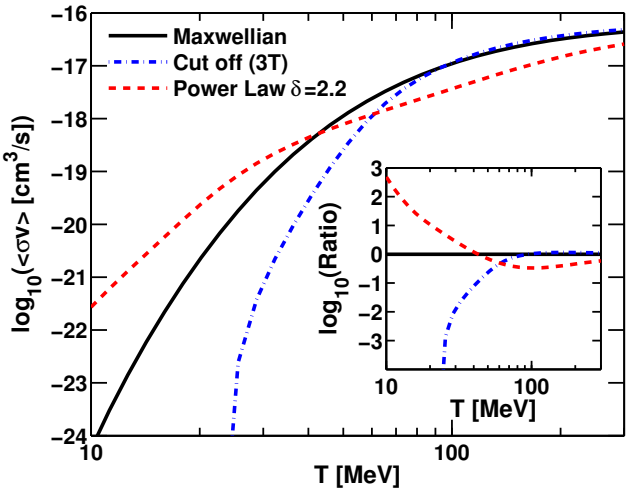

Figure 3.3: Comparison of the π^0 production rates for three different distributions as a function of temperature. Solid black line is calculated for a pure Maxwellian distribution plasma. The blue dot-dash line is calculated for Maxwellian distribution with a sharp cutoff at proton kinetic energy $E_k = 3k_BT$ ($\gamma_0 = 1 + 3\theta$). The red dash-line is calculated for a Maxwellian distribution with a power-law tail $E_k^{-2.2}$ ($\gamma_0 = 1 + 3\theta$). The inserted figure shows the ratio of the two modified distributions rates compare to the pure Maxwellian distribution one.

the pure Maxwellian distribution. Most of the particles go to the relatively cold Maxwellian "core" leaving the tail lesser populated. This results in the reduction of the rate at high temperatures compare to the pure Maxwellian distribution.

3.4 Gamma-radiation spectra from $p + p \rightarrow \pi^0$ reaction

The aim here is to compute the γ-radiation spectra for plasma temperatures between 20-200 MeV. For this temperature interval, the π^0 production threshold plays a crucial role for the γ-ray spectra similarly as it does with the π^0 production rate. Therefore, we need to calculate the γ-ray spectra close to the π^0 kinematic threshold.

Convenient fits for γ-ray spectra at very high proton energies Kelner et al. (2006) and intermediate proton energies Kamae et al. (2006) have been suggested in the literature. For energies close to the $p + p \rightarrow \pi^0$ kinematic threshold, one finds the differential cross-section for π^0 production spectra that has been suggested by Stecker (1970).

3.4.1 The plasma π^0 production spectra

For calculations it is convenient to use a δ-function approach suggested by Aharonian and Atoyan (2000):

$$\frac{dN}{dE_\pi}(\theta, \mathcal{K}, E_\pi) = \int d\,R(\theta) \times \frac{\mathcal{A}}{m_\pi c^2} \times \delta\left(\frac{E_\pi - \mathcal{K}\, m_p\, c^2(\gamma_r - 1)}{m_\pi c^2}\right) \tag{3.10}$$

Here E_π is the π^0 total energy; $d\,R(\theta)$ is defined by eq. (3.3) or eq. (3.5), depending on the plasma distribution function. From the conservation of the total number of π^0-mesons, the constant is set $\mathcal{A} = 1.05$ and $\mathcal{K}$ is fixed by the condition

$$\int\limits_{m_\pi c^2}^{\infty} dE_\pi\ \frac{dN}{dE_\pi}(\theta, \mathcal{K}, E_\pi) = R(\theta)\ , \tag{3.11}$$

$R(\theta)$ is defined from the integration of eq. (3.3) or eq. (3.5) depending on the plasma distribution function.

The γ-ray spectrum is obtained by integrating the π^0 spectrum

$$\frac{dN}{dE_\gamma}(E_\gamma, \theta, \mathcal{K}) = 2 \times \int\limits_{E_\gamma + \frac{m_\pi^2 c^4}{4E_\gamma}}^{\infty} \frac{dE_\pi}{\sqrt{E_\pi^2 - m_\pi^2 c^4}}\ \frac{dN}{dE_\pi}(E_\pi, \theta, \mathcal{K}) \tag{3.12}$$

3.4.2 Parameter $\mathcal{K}(T)$ for a pure Maxwellian plasma

Solution of eq. (3.11) for a given $R(T)$ for a pure Maxwellian plasma, provides a unique $\mathcal{K}$. Figure 3.4, shows the dependence of $\mathcal{K}$ on temperature. We can fit the parameter $\mathcal{K}(\theta)$ with accuracy better than 0.4 % by the following

$$\begin{aligned}\mathcal{K}(\theta) = 0.061\ \exp\left(-\left(\frac{\log_{10}(\theta) + 1.768}{0.32}\right)^2\right) + \\ + 2.781\ \exp\left(-\left(\frac{\log_{10}(\theta) + 9.867}{5.76}\right)^2\right)\end{aligned} \tag{3.13}$$

The fit of $\mathcal{K}(\theta)$ is shown in fig. 3.4.

3.5 The plasma cooling rate from π^0 production

The emission from the decay $\pi^0 \to 2\gamma$ carries energy which escapes from the plasma. Figure 3.5 shows the energy cooling rate for $\pi^0 \to 2\gamma$ emission. It also shows for comparison some typical cooling processes of ions such as the electrons heating through Coulomb exchange, nuclear lines, nuclear continuum radiation including p–n capture and bremsstrahlung.

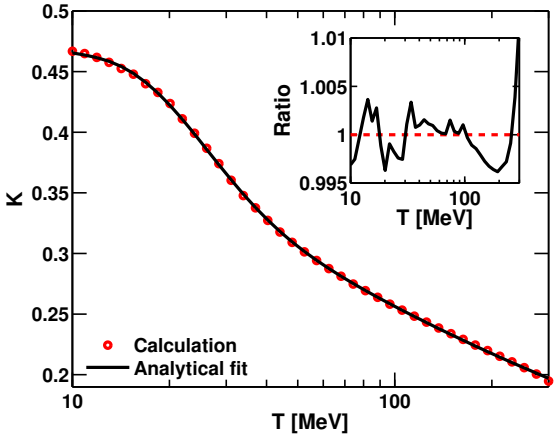

Figure 3.4: The temperature dependence of the parameter $\mathcal{K}$ inside the δ-fuction. Circles are the numerical calculation of eq. (3.11) and the solid line is the fit formula in eq. (3.13). The inserted figure shows the ration between the fit and the numerical calculation.

We find that the energy loss due to π^0 production can be fitted for temperatures $k_B T < 300$ MeV, by the following

$$q_\pi(T) = \frac{m_\pi c^2}{2\,K(T)} \times R(T) \tag{3.14}$$

$R(T)$ and $K(T)$ are given by eqs. (3.6) and (3.13), respectively. Figure 3.6 compares the π^0 energy loss between the numerical calculations and the fit.

The accuracy of the fit is better than 17 % for plasma temperatures between $10 \leq k_B T \leq 300$ MeV.

3.6 π^0 decay γ-radiation of a Maxwellian distribution plasma

The γ-ray spectra for different temperatures and models are presented in fig. 3.7. These spectra are based on the cross-section proposed by Kamae et al. (2006), from Dermer (1986) and the δ-function approach that is described here. Figure 3.7 shows that the delta function approach produces results that mimic Dermer (1986). The Kamae et al. (2006) fits always produce a wider spectra compared to Dermer (1986) and the one from the δ-function approach.

For the temperature $k_B T = 20$ MeV, the Kamae et al. (2006) cross-section gives γ-ray spectra which is lower than Dermer (1986) or δ-function ones. The reason is that Kamae et al. (2006) are correct for proton kinetic energies $E_k > 488$ MeV, which is 1.7 times larger than the kinematic threshold.

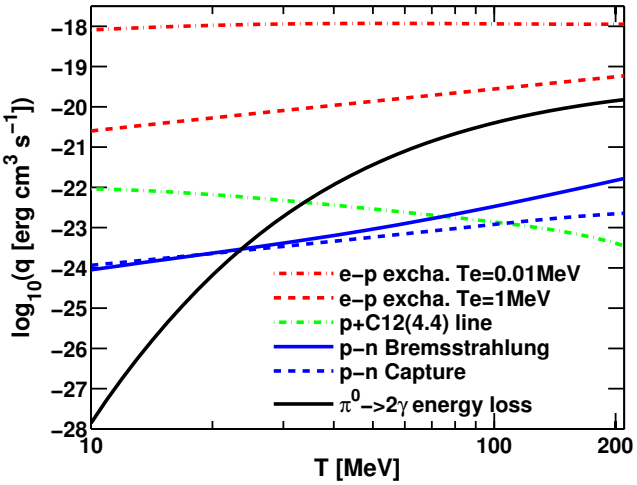

Figure 3.5: Comparison of the plasma $p + p \rightarrow \pi^0 \rightarrow 2\gamma$ energy loss (solid-black line) versus other ion interaction losses such as: the ion-electron Coulomb exchange for two electron temperatures – characteristic of a two temperature accretion plasma – $k_B T_e = 0.01$ MeV (red dot-dash line) and $k_B T_e = 1$ MeV (red dash line). The ^{12}C(4.4) line is a representative of the nuclear line emission (green dot-dash line). The cooling processes representative of proton-neutron (p–n) plasma, the p-n bremsstrahlung (solid-blue line) and the p-n capture ($p + n \rightarrow D + \gamma$) the blue dash line. The ion-electron Coulomb exchange calculation considers equal amount of protons and electrons. The ^{12}C(4.4) is calculated for a plasma with equal abundance of protons and ^{12}C. The p–n capture and bremsstrahlung considers equal abundance of protons and neutrons.

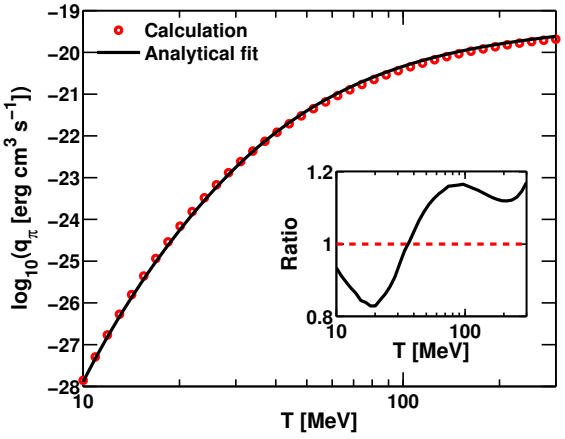

Figure 3.6: The comparison of the $p + p \rightarrow \pi^0$ energy loss between the numerical calculations and the fit formula of eq. (3.14). The inserted figure shows the ratio between the fit and the numerical calculations.

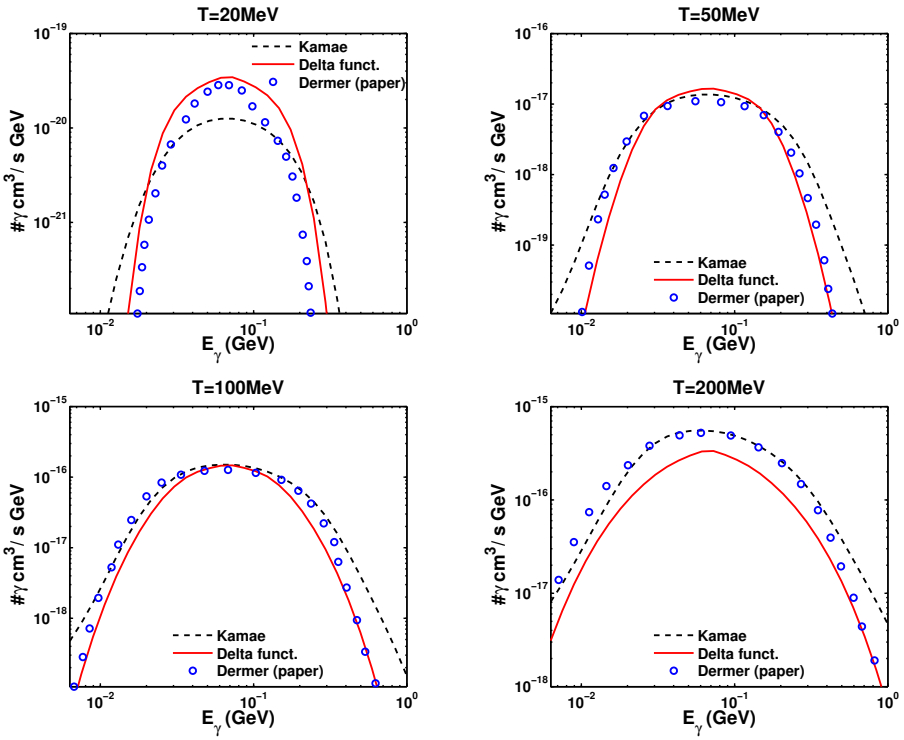

Figure 3.7: Gamma-ray spectra of a Maxwellian distribution plasma for different temperatures between Kamae et al. (2006), Dermer (1986) and the δ-function approach. The difference of the δ-function approach at $k_BT = 200$ MeV comes from the flatter cross-section that is used here – which is motivated by the data. For temperature 20 MeV the Kamae et al. (2006) calculation is lower because their cross-sections are valid for $E_k > 488$ MeV.

For temperatures $k_BT = 50$ and 100 MeV the δ-function approach give results that are in good agreement with Dermer (1986). Whereas for $k_BT = 200$ MeV, the δ-function approach is lower than Dermer (1986) and Kamae et al. (2006) because of the π^0 production cross-section that is used. The cross-section in fig. 3.1, is lower than the one used by Dermer (1986).

The γ-ray spectrum of the δ-function approach for a Maxwellian distribution plasma is fitted as a function of E_γ and temperature. The analytical fit formula has the following representation

$$\frac{dN}{dE_\gamma}(\theta) = 2 \times R(\theta) \times \frac{dS_\gamma}{dE_\gamma} \quad \left[\mathrm{cm}^{-3}\,\mathrm{s}^{-1}\,\mathrm{GeV}^{-1}\right]$$

$$\frac{dS_\gamma}{dE_\gamma}(\theta) = \frac{\theta\ \exp\left(-\sqrt{\mathcal{X}}/\theta\right)}{m_\pi c^2} \times$$

$$\times \exp\left(A_1(\theta) + A_2(\theta)\,\mathcal{Y} + A_3(\theta)\,\mathcal{Y}^2 + A_4(\theta)\,\mathcal{Y}^3\right) . \qquad (3.15)$$

Here $m_\pi c^2$ is the π^0 mass (in GeV). The $\mathcal{X} = E_\gamma/m_\pi c^2 + m_\pi c^2/(4E_\gamma)$, $\mathcal{Y} = \log(\mathcal{X})$.

The functions $A_1(\theta) - A_4(\theta)$ are defined in eq. (3.16). Let $x = \log(\theta)$ then:

$$\begin{aligned} A_1(\theta) &= \exp\left(a_1 + a_2\, x + a_3\, x^2 + a_4\, x^3\right) \ , \\ A_2(\theta) &= \theta^{-1/2}\left(b_1 + b_2\, x + b_3\, x^2 + b_4\, x^3\right) \ , \\ A_3(\theta) &= c_1 + c_2\,\theta^{-1} + c_3\,\theta^{-2} + c_4\,\theta^{-3} + c_5\,\theta^{-4} + c_6\,\theta^{-5} \ , \\ A_4(\theta) &= d_1 + d_2\,\theta^{-1} + d_3\,\theta^{-2} + d_4\,\theta^{-3} + d_5\,\theta^{-4} + d_6\,\theta^{-5} \ . \end{aligned} \tag{3.16}$$

The values of the $a_1 - a_4$, $b_1 - b_4$, $c_1 - c_6$ and $d_1 - d_6$ coefficients are shown in table 3.1.

Table 3.1: The coefficients a, b, c and d of the functions $A_1(\theta)$, $A_2(\theta)$, $A_3(\theta)$ and $A_4(\theta)$, respectively.

index	a	b	c	d
1	-5.7938E-1	1.1784	2.0462	-1.0110
2	-1.5822	2.4825	-7.5069E-2	6.6742E-2
3	-1.8994E-1	1.4282	-3.8762E-2	1.5706E-2
4	-2.0215E-2	1.6593E-1	2.0636E-3	-9.5610E-4
5			-3.5334E-5	1.7342E-5
6			2.0315E-7	-1.0322E-7

The fit in eq. (3.15) is valid for proton temperatures between 15-220 MeV and for photon energies E_γ between 10-600 MeV. The raccuracy of the fit is about 10-15 % for temperatures between 15-30 MeV and about 8 % or less for temperatures between 30-220 MeV.

3.7 π^0 decay γ-radiation of modified Maxwellian distribution plasma

As long as the plasma temperature is lower than the threshold energy of π^0 production, the distribution tail will have a strong effect on the π^0 decay γ-ray spectrum. This is illustrated for a proton plasma with Maxwellian distribution of temperatures $k_B T = 50$ MeV. The Maxwellian distribution tail is modified as discussed in section 3.3.2 to produce a Maxwellian distribution with a sharp cutoff and a Maxwellian distribution with a power-law tail. The cut off is taken at kinetic energy $E_k = 3k_B T$. Two cases of power law tail are considered, one is with power law index $\delta = 2.2$ and the other one is with index $\delta = 4$. Figure 3.8 shows the shape of the distributions and the corresponding γ-ray spectra due to π^0 decay.

The γ-ray spectra imprints the characteristics of the proton distribution. Let we separate the proton distribution function into the tail and the core parts, then π^0-mesons are produce by protons that come both from the "core"

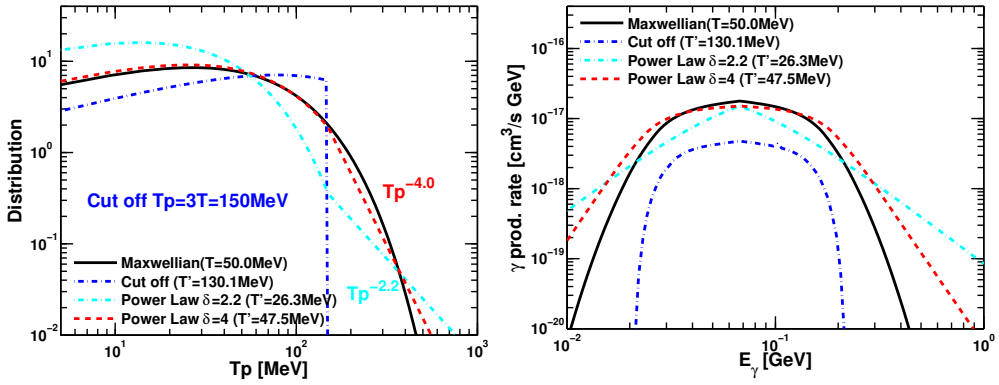

Figure 3.8: Gamma-ray spectra due to π^0 production in modified Maxwellian distributions at $k_BT = 50$ MeV. On the left the proton distribution functions are shown; whilst, on the right the corresponding γ-ray spectra. The initial Maxwellian distribution temperature is $k_BT = 50$ MeV. The Maxwellian distribution tail is modified either by a sharp cutoff at proton kinetic energy $E_k = 3k_BT$ or by a power-law tail with index $\delta = 2.2$ and $\delta = 4$. Note that because of the condition of the energy conservation the temperatures are different.

(for short we can call *core–core* interaction); one of the protons come from the Maxwellian "core" and the other come from the tail (or the *core–tail* interaction); both protons come from the tail (or the *tail–tail* interaction).

The *core–core* interactions involve protons that come from relatively low energy parts of the distribution (with $E_k \sim k_BT$). Thus, we will observe this interaction in the γ-ray spectrum, only if the plasma effective temperature is high enough so that protons can produce π^0-mesons. Due to low energy protons that are involve in this interaction, the π^0-mesons are produced almost at rest. Consequently, photons have energy around $E_\gamma \approx m_\pi c^2/2$.

At low temperatures, more abundant $p + p$ interactions are the *core–tail* interaction because they combine the high energy protons from the tail and a large number of particles from the Maxwellian core. The *tail–tail* interactions at low temperatures are suppressed.

Let us consider the γ-ray spectra produced by a Maxwellian distribution proton plasma as the standard shape. By using the above analyses, we can discuss qualitatively how the γ-ray spectra of a modified Maxwellian distribution plasma deviates from the standard one.

The Maxwellian distribution with a sharp cutoff is obviously limited by the *core–core* interaction; thus, the γ-ray spectrum is narrower than the standard one. Note that in our calculation of the sharp cutoff distribution, we have required the conservation of energy, therefore the Maxwellian distribution with a sharp cutoff has higher temperature.

For temperatures lower than $k_BT < 90$ MeV, the π^0 production rate of

the Maxwellian distribution with a sharp cutoff is lower than that of a pure Maxwellian distribution. However, the rate between these two distributions becomes comparable for $k_BT > 90$ MeV, as can be seen in fig. 3.3.

The Maxwellian distribution with a power-law tail of index $\delta = 2.2$, at low temperatures has a distribution core with effective temperature lower than the original Maxwellian because this distribution contains more protons in the tail. Therefore, *core–core* interaction is not effective to produce π^0-mesons, whilst the *tail–core* interaction dominates. Hence, the γ-ray spectra are a result of the high energy protons from the core with relatively cold protons from the Maxwellian core. This results in a power law shape of the γ-ray production spectra with the same index as that of the distribution, i.e. $\delta = 2.2$

The Maxwellian distribution with power-law tail of index $\delta = 4$ has a hotter Maxwellian core and lesser protons in the tail compare to the power law of index $\delta = 2.2$. Thus both *core–core* and *core–tail* interactions are featured in the γ-ray spectra. For this reason the central part around the peak $E_\gamma \approx m_\pi c^2/2$ will contain the *core–core* and *core–tail* features. Whereas for higher energies, where *core–tail* interactions dominate, the γ-ray spectra transform to a power law of index similar to that of the tail i.e. $\delta = 4$.

With an increase of the temperature, the effect of the distribution tail become less pronounced, as it is demonstrated in fig. 3.9 where the γ-ray spectra are shown for the temperature $k_BT = 100$ MeV. Note that for this case the cut-off distribution will have a temperature higher than the $E_k = 3k_BT$, thus it is not a physically meaningful example. We see that the discussion above for the $k_BT = 50$ MeV Maxwellian plasma applies here as well.

3.8 Gamma-ray spectra due to π^0 production versus nuclear de-excitation lines

Here we will consider a plasma that has initially a solar composition. The nucleon number density and ion temperature are kept fixed during the whole evolution $t_{tot} = 100$ s. Figure 3.10 shows the time evolution of the chemical composition and the γ-ray emissivity for three instants of a $k_BT = 50$ MeV plasma. These instants are related to the stage when the initial heavy nuclei begin to breakup; the stage when the ^{4}He nuclei start to breakup, and the third stage when a proton–neutron plasma is formed and all other nuclei are destroyed.

The γ-ray spectra of the first stage is dominated by nuclear lines and π^0 decay γ-ray spectra. In the second stage, the γ-ray spectra is dominated by π^0 decay γ-ray spectra as well as the γ-ray lines from $\alpha - \alpha$ reactions (e.g.

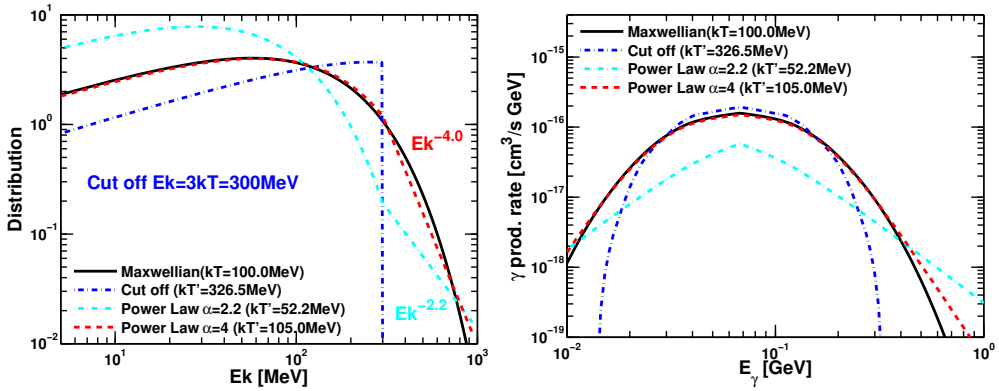

Figure 3.9: Gamma-ray spectra due to π^0 production in modified Maxwellian distributions at $k_BT = 100$ MeV. On the left the proton distribution functions are shown; whilst, on the right the corresponding γ-ray spectra. The initial Maxwellian distribution temperature is $k_BT = 100$ MeV. The Maxwellian distribution is modified either by a sharp cutoff at proton kinetic energy $E_k = 3k_BT$ or by a power law tail of index $\delta = 2.2$ and $\delta = 4$. Note that because of the condition of the energy conservation the temperatures are different.

^{7}Li(0.478 MeV)), p–n and $p-\alpha$ bremsstrahlung and p–n capture. The third stage is a proton-neutron plasma; thus γ-ray spectra is dominated by the π^0 decay γ-ray spectra and p–n capture and bremsstrahlung. Note that due to isospin symmetry the $p + p \rightarrow \pi^0$ production is symmetric with $n + n \rightarrow \pi^0$. The γ-ray spectra of the thermal electron bremsstrahlung with electron temperature $k_BT_e = 0.1$ MeV is included. It dominates for temperatures below 1 MeV.

Figure 3.11 shows the γ-ray spectra for a solar composition plasma for two different temperatures $k_BT = 20$ MeV and $k_BT = 100$ MeV at the period when all initial nuclei are present. By changing the plasma temperature from 20 to 100 MeV the γ-ray spectra from π^0 production is increased about four orders of magnitude. Instead, the nuclear γ-ray lines decreases roughly by a factor of 4.

3.9 Summary and Discussion

In this chapter the chemical and γ-ray emissivity evolution for a two temperature plasma have been calculated for the first time. The γ-ray emissivity that comes from π^0 production is included.

There are three stages that chemical composition of a very hot plasma can go through. The first stage is before all elements heavier than ^{4}He are destroyed. The second stage is after all heavy elements are destroyed but before ^{4}He destruction. The third stage is when all elements are destroyed

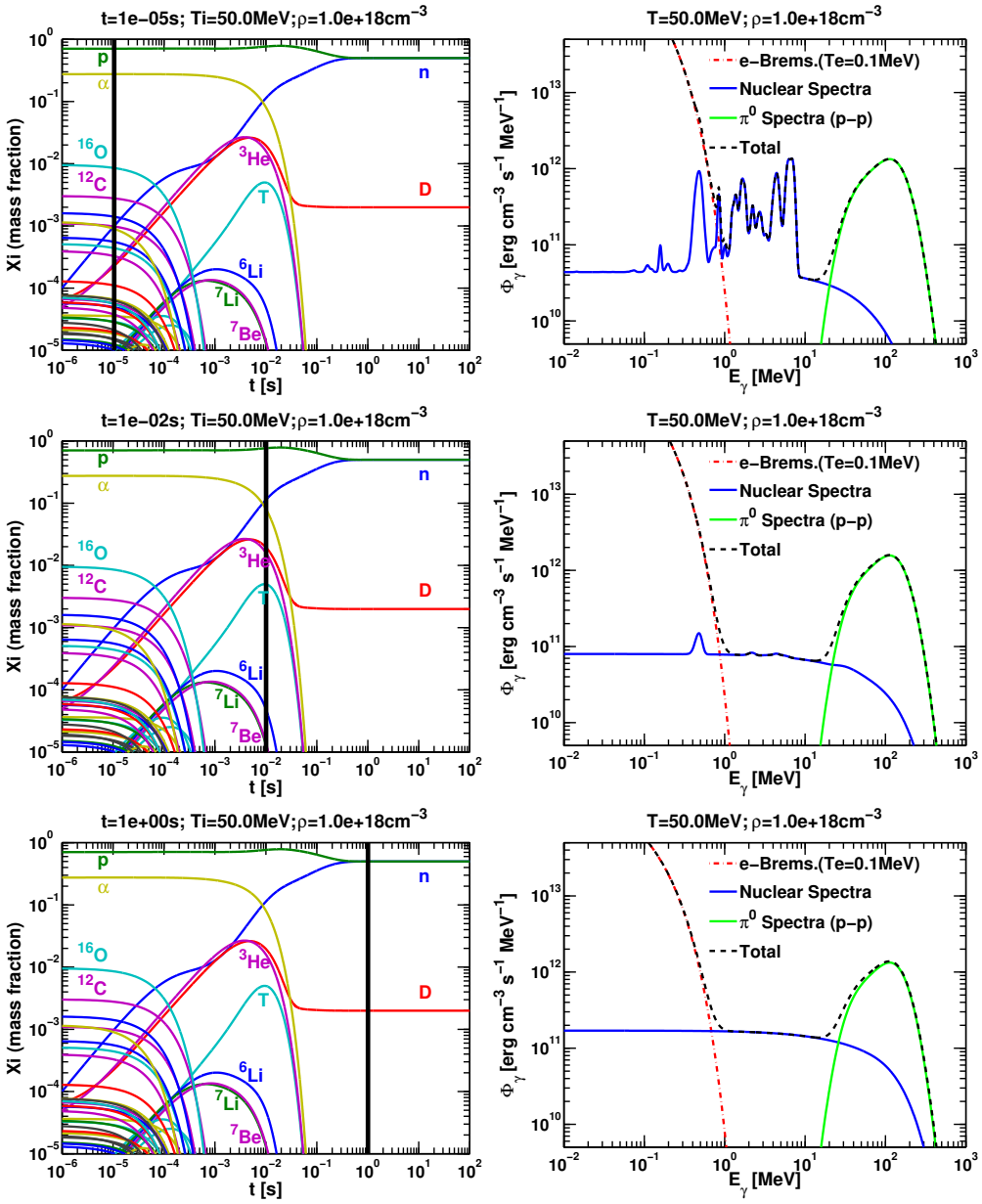

Figure 3.10: Time evolution of the chemical composition and γ-ray spectra of an initial solar composition plasma. Plasma evolves for 100 seconds with a fixed temperature $k_BT = 50$ MeV and nucleons number density $\varrho_u = 10^{18}$ cm^{-3}. On the left the temporal chemical evolution is shown and with the black vertical line is marked the period when the γ-ray spectra is constructed on the right hand side, respectively. The nuclear γ-ray spectra is composed by the nuclear lines, the nuclear bremsstrahlung and the capture reactions. There is also shown the γ-ray spectrum from π^0 production. The thermal electron bremsstrahlung at temperature $k_BT_e = 0.1$ MeV is also shown.

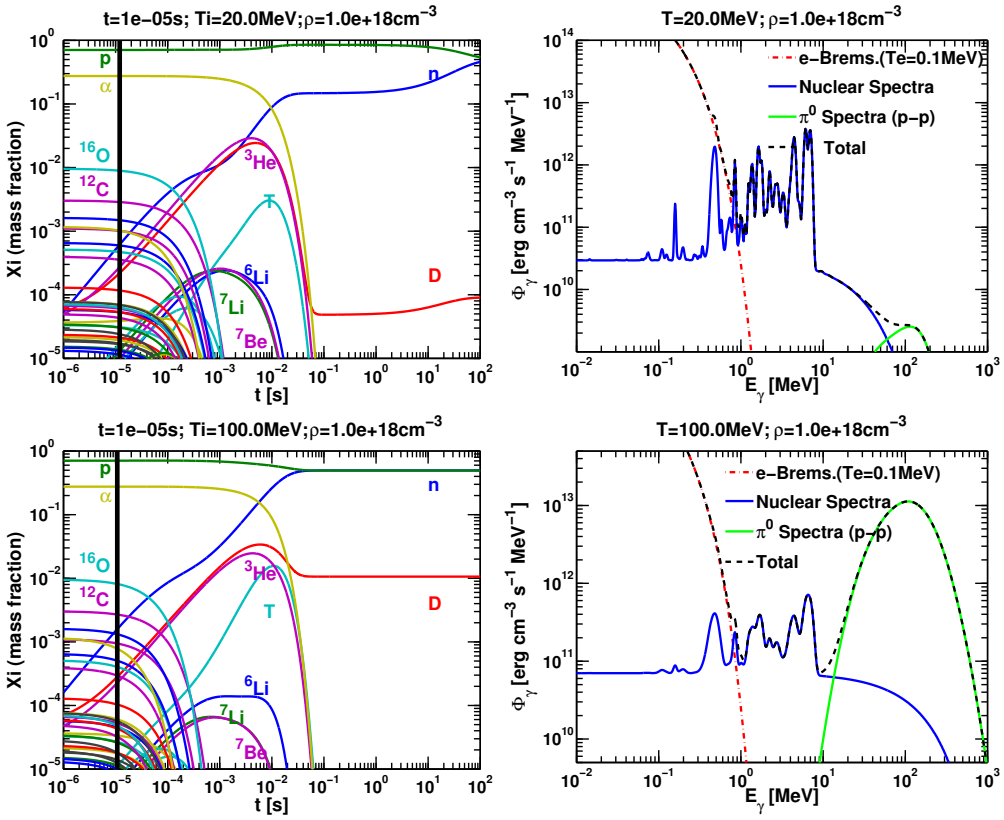

Figure 3.11: Time evolution of the chemical composition and γ-ray spectra of an initial solar composition plasma at $k_BT = 20$ MeV and $k_BT = 100$ MeV. The nucleons number density is fixed $\varrho_u = 10^{18}$ cm^{-3}. The nuclear γ-ray spectra is composed by the nuclear lines, the nuclear bremsstrahlung and the capture reactions. The γ-ray spectrum from π^0 production is plotted separately. The thermal electron bremsstrahlung at temperature $k_BT_e = 0.1$ MeV is also shown.

and a p–n plasma is formed.

Although, different γ-ray spectra components are strongly influenced by the chemical composition evolution, the π^0 production is a function of proton abundance. Because proton abundance evolve very slowly, the π^0 component of γ-radiation is almost constant. Other γ-radiation components depend on the chemical evolution stage. The first stage is dominated by nuclear lines coming from heavy nuclei interactions. The second stage spectra is dominated by nuclear lines produced via $\alpha + \alpha$ reaction products, the $p - n$ and $p - \alpha$ bremsstrahlung as well as $p - n$ capture. The third stage is dominated by $p - n$ capture and bremsstrahlung. It is noticeable that γ-ray emissivity due to π^0 production start to dominate nuclear lines for a plasma with temperature $k_BT > 50$ MeV.

As long as the plasma temperature is less than the threshold energy of

$p + p \rightarrow \pi^0$ production, the π^0 production rate will strongly depend on the high energy part of the plasma distribution function. For this reason we have investigated the π^0 production rate and γ-ray emissivity for different distribution "tails".

Two classes of modified Maxwellian distribution tails were considered. The sharp cutoff Maxwellian distribution which is a Maxwellian distribution for which the tail is cut off at a certain energy. The second class includes Maxwellian distribution the tail of which is replaced – from a certain energy – with a power law function.

The numerical tools that allow us to perform the calculation of the π^0 production rate and γ-ray spectrum for a modified Maxwellian distribution function, were developed. This tools are validated for a thermal plasma by comparing the π^0 production γ-ray spectrum with Dermer (1986) and Kamae et al. (2006) calculations.

Modified Maxwellian distribution imprints its characteristics in the π^0 production γ-ray spectrum. For a sharp cutoff Maxwellian distribution for which no high energy protons are present, the γ-ray spectrum will also show a cut off, i.e. it will be narrower compare to a pure Maxwellian distribution. For a Maxwellian distribution with a power law tail, low and high energy part of the γ-ray spectrum will have a power law shape of the same index. The reason is the interaction between high energy protons from the tail with the relatively cold protons from the core. Hence, observation of the γ-ray spectrum from π^0 production will give us information about the distribution tail. On the other hand, detection of the Doppler broadened γ-ray lines give us information about the plasma distribution core.

For a Maxwellian distribution plasma, accurate analytical fits are provided for the π^0 production rate, cooling rate and for the γ-ray spectrum.

4 Nuclear γ-ray emission of hot accretion flow onto black hole

4.1 Introduction

Hard X-ray emission of compact binary systems is explained by radiation of a hot accretion plasma with electron temperature up to 100 keV.

One of the first attempts to explain these very high energy photons was done by Shapiro et al. (1976) (the SLE model for short). The SLE model is a very hot, optically thin, two temperature accretion disk plasma with no advection. Here the only cooling process for ions is the Coulomb exchange with electrons. Electrons on the other hand, are heated by ions, loose their energy radiatively through Bremsstrahlung and Comptonization. Because of the low density, the Coulomb exchange interaction cannot equalize the ion and electron temperature; therefore, ions and electrons are decoupled. As a result, a two temperature plasma is formed. The typical SLE electron temperature is of the order of $T_e \sim 10^9$ K, whereas, the ion temperature can go up to $T_i \sim 10^{11}$ K. This model is thermally unstable and its realization has been questioned (see e.g. Abramowicz et al., 1995, 2000).

The importance of advection on the heat transport and on viscous and thermal accretion disk stability, has been recognized by many authors (e.g. Paczynski and Bisnovatyi-Kogan, 1981; Abramowicz et al., 1988; Narayan and Popham, 1993; Narayan and Yi, 1994; Abramowicz et al., 1995).

The modelling of a two temperature optically thin accretion plasma with advection is described in Narayan and Yi (1994, 1995*a*,*b*). These models are often called Advection Dominated Accretion Flows (or ADAF models). Ions and electrons interact ineffectively through Coulomb exchange; hence, ions and electrons are decoupled. The electrons are cooled through Synchrotron, Bremsstrahlung and Comptonization and their temperature can reach values $T_e \sim 3 \times 10^9$ K. On the other hand, the ion temperature is close to the virial temperature and can be as high as $T_i \sim 10^{12}$ K.

Due to the high ion collision energy ($k_B T_i > 1$ MeV) – larger than their

binding energy – nuclei in the accretion plasma can easily break up. The breakup reactions dominate in very hot accretion plasmas and will be responsible for the plasma chemical evolution, as it has been shown in the previous chapter. Nuclear interactions can also produce γ-rays. Estimations for different γ-ray emission components and different very hot accretion models are found in e.g. Dahlbacka et al. (1974); Higdon and Lingenfelter (1977); Kolykhalov and Syunyaev (1979); Bisnovatyi-Kogan et al. (1980); Aharonian and Sunyaev (1984, 1987); Mahadevan et al. (1997); Yi and Narayan (1997); Jean and Guessoum (2001); Oka and Manmoto (2003).

The γ-rays resulting from nuclear interactions will produce a characteristic spectrum of the accretion disk in the MeV energy range. The measurement of this spectrum would give unique information about such as for example the ion temperature.

Nuclear reactions in a very hot accretion disk can also produce indirect effects. Due to e.g. positive Bernoulli integral, the accretion disk may have winds which can carry material from the disk and contaminate the surroundings. The hot disk can also evaporate neutrons which can produce some further nuclear reactions e.g. in the binary companion star atmosphere.

Very high temperature accretion models such as ADAF, with an optically thin plasma with respect to neutrons, can evaporate thermal neutrons almost isotropically. The breakup reactions in the accretion disk plasma produce neutrons. Due to their electrical neutrality, neutrons with energy high enough to overcome gravity can easily escape (e.g. Aharonian and Sunyaev, 1984; Jean and Guessoum, 2001). The evaporated neutrons have high energies and can reach the companion star atmosphere before decay. In the star atmosphere, neutrons can destroy heavier nuclei such as Carbon, Oxygen, Nitrogen (the CNO nuclei) and produce light elements such as Lithium, Beryllium and Boron. They can also scatter off in the star atmosphere and cool down until they are captured by Hydrogen and producing Deuterium and the characteristic 2.2 MeV γ-rays (Aharonian and Sunyaev, 1984; Jean and Guessoum, 2001). This chemical composition modification of the companion star atmosphere can become a contamination source of the interstellar medium.

The aim of this chapter is to calculate the ion component of plasma γ-ray spectra due to nuclear reactions for the ADAF and SLE models. Both models, as we have already described, predict very hot optically thin two temperature plasmas. This imply that nuclear reactions can affect plasma composition and the electron temperature is low enough, so that the radiation of the disk cannot mask the nuclear γ-ray lines.

Using the nuclear network that is described in chapter 2, the chemical abundances and nuclear γ-ray emissivity evolution with the disk radius, are

calculated. Upper limits have been found on the luminosities of different parts of the γ-ray spectra and on the neutrons evaporation efficiency.

The accretion plasma may not always be able to fully thermalize and develop the Maxwellian distribution tail, as described in chapter 3. This can strongly affect the γ-ray emissivity of high energy threshold reactions such as $p + p \rightarrow \pi^0$. The π^0 production γ-ray spectrum for an ADAF accretion plasma with non-developed Maxwellian tails is also calculated.

4.2 Method

The calculation of the nuclear γ-ray emissivity of the accretion disk requires an accretion model and a comprehensive nuclear reaction network. The accretion model predicts the plasma physical parameters such as plasma density, ion temperature, radial velocity etc. The nuclear network on the other hand, contains information about the most relevant nuclear reactions and their γ-ray production rates. By solving the nuclear network for each radius of the disk, we find the chemical abundances and γ-ray emissivity evolution throughout the disk.

4.2.1 Accretion models

The accretion models used here are the ADAF (Narayan and Yi, 1994, 1995*a*,*b*) and the SLE (Shapiro et al., 1976). Both of these models have solutions for which every physical quantity is a function of the radius R (or $r = R/R_s$ where R_s the Scharzschild radius) and the accretion disk parameters: the viscosity parameter α, the mass of the black hole M (or $m = M/M_\odot$ where $M_\odot$ is the solar mass), the accretion rate $\dot{M}$ (or $\dot{m} = \dot{M}/\dot{M}_{edd}$ where $\dot{M}_{edd}$ is the so called Eddington accretion rate) and the parameter $\beta = P_{\rm g}/P_{\rm tot}$ which relates the gas pressure to the total pressure $P_{\rm tot} = P_{\rm g} + P_{\rm m}$, where $P_{\rm m}$ is the magnetic pressure (see e.g. Narayan and Yi, 1995*a*).

Note that the original SLE model has been modified to include the Synchrotron cooling (in additional to the Comptonization). This modification slightly lowers the SLE electron temperature.

By defining α, m, $\dot{m}$ and β, we can calculate any other physical quantity for every radius r (see Shapiro et al., 1976; Narayan and Yi, 1995*a*). To facilitate these calculations, a computer code is developed, which calculate all relevant model parameters in the framework of the ADAF and SLE models.

4.2.2 Accretion plasma with a modified Maxwellian distribution

Ions in the accretion disk may not be in thermodynamic equilibrium. Due to the low plasma density and short accretion time-scales, ions do not have

enough time to exchange energy and momentum. Hence, ions may not fully develop their Maxwellian distribution tail.

The ADAF models predict very high ion temperatures $k_B T_i \sim 100$ MeV; therefore, nuclear reactions and γ-ray lines are not affected by the ion distribution tail. As it is described in chapter 2, the nuclear reaction cross-sections typically have a threshold of few MeV/nucleon. They peak around 10-30 MeV/nucleon and then they decrease as a power-law. This means that the most important part of the cross-section is covered by the core of a Maxwellian distribution with an average energy of order ~ 10 MeV. The π^0 (π^+) production reactions are strongly influenced by the Maxwellian distribution tail.

In this section we consider two type of modified Maxwellian distribution of particles. The first one assumes that plasma cannot form a Maxwellian tail at all. In this case is assumed a sharp cutoff of the Maxwellian distribution $3\,k_B T_i$. The second case assumes some acceleration mechanism to be present in the plasma which produces a suprathermal component of particles above the Maxwellian distribution tail. Thus, the pure Maxwellian distribution tail is replaced from a proton kinetic energy $3\,k_B T_i$ with a power law tail of index 2.2.

Both, ADAF and SLE accretion flows, have very hot and optically thin plasma; therefore, the nuclear breakup reactions dominate. We assume that their plasma initial composition is similar to the solar composition of elements. The low number density ensures that nuclei will interact in their ground state, see section 2.2.

The electron temperatures for ADAF and SLE models are $k_B T_e < 0.3$ MeV. Hence, the thermal Bremsstrahlung photo-production rate for $E_\gamma > 3$ MeV is negligible. The ADAF has a maximum number density of the order $\varrho \sim 10^{16}\,\mathrm{cm}^{-3}$ and the radius for which the nuclear reactions are important is of the order $R \sim 10^8$ cm. The SLE has a maximum number density of the order $\varrho \sim 10^{18}\,\mathrm{cm}^{-3}$ and $R \sim 10^6 - 10^7$ cm. Therefore, the photodisintegration ratio with respect to proton reactions for both models is $\Gamma_{(\gamma,\mathcal{A})}/\Gamma_{(p,\mathcal{A})} \ll 10^{-5}$ in case of a solar composition and $\Gamma_{(\gamma,\mathcal{A})}/\Gamma_{(p,\mathcal{A})} \ll 10^{-3}$ if we have higher metallicity plasma (i.e. $n_{\mathcal{A}}/n_p = 10^{-1}$) see eq. (B.7) – $\mathcal{A}$ is a given nucleus. A more important impact on the dynamics of the accretion flow may have the effect of evaporation of neutrons.

Below we use the notation for which a quantity Q is scaled as $Q_{(i)} = 10^{-(i)}\,Q$, where the index i shows the power of ten.

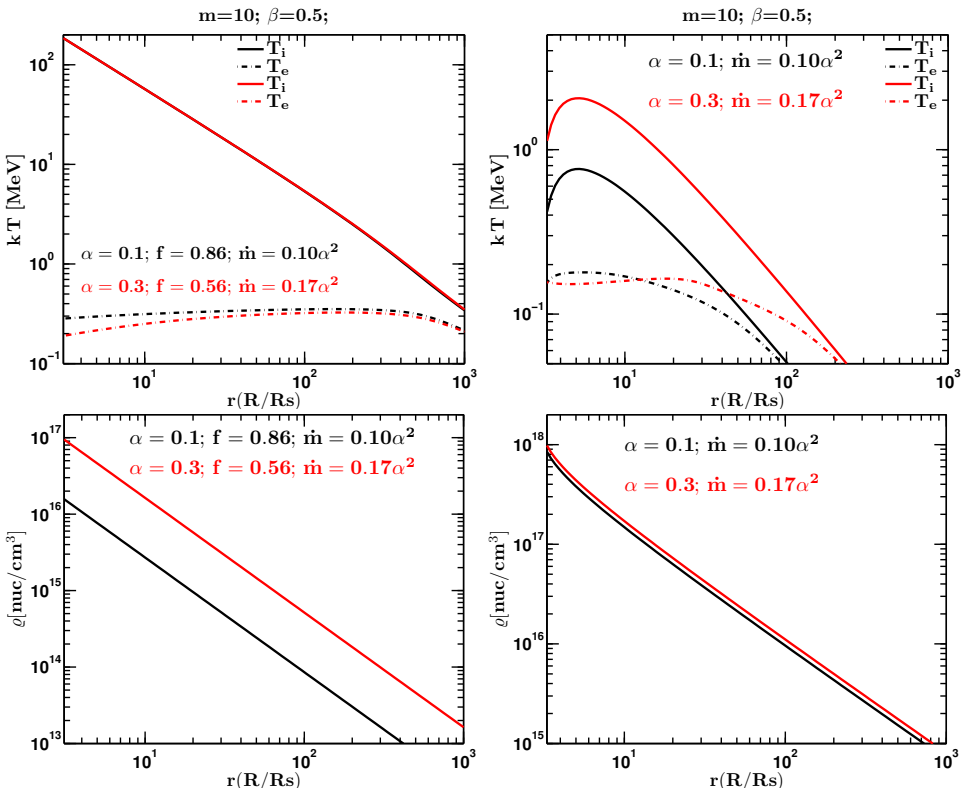

Figure 4.1: The temperature and density profiles for ADAF and SLE models. The figures on the left are the profiles for the ADAF model; the figures on the right are for the SLE model. Two sets of parameters are considered: in one case $\alpha = 0.1$, $\dot{m} = 0.1 \times \alpha^2$ and in the other $\alpha = 0.3$, $\dot{m} = 0.17 \times \alpha^2$. The $m = 10$ and $\beta = 0.5$ are kept fixed. The black color is used for the first set of parameters, whilst red for the second.

4.3 Results

To demonstrate the radial chemical evolution and the emissivity spectra for ADAF and SLE accretion models, two different sets of accretion parameters are chosen. Parameters kept fixed are $m = 10$ and $\beta = 0.5$; we use $\alpha = 0.1$, $\dot{m} = 0.1 \times \alpha^2$ for the first case, and $\alpha = 0.3$, $\dot{m} = 0.17 \times \alpha^2$ for the other. The plasma initial composition is considered to be the solar composition of elements. We will also assume the case of higher metallicity plasma for which the initial mass fraction abundances are $X_p = X_\alpha = 0.3$ and $X_{C12} = X_{O16} = 0.2$.

Figure 4.1 compares the temperature and the density profiles of the ADAF and SLE models for the accretion parameters. It shows clearly that the ADAF ion temperature is independent of the accretion parameters and is equal to the virial temperature. The ADAF electron temperature and density however, are more sensitive on the parameters. The SLE, on the other hand, has a density profile that is not sensitive to model parameters.

Figures 4.2 to 4.5 show the chemical evolution of the plasma as a function of the disk radius and the disk emissivity $\Phi_\gamma(E_\gamma)$.

The ADAF accretion model predict much hotter plasma than the SLE model. Therefore, for a set of parameters close to the critical ones, the ADAF is able to destroy all heavy nuclei. Nuclear reactions become important already at 100 R_s. Moving toward the last stable orbit, the ADAF plasma becomes hotter and denser. As a result, the destruction processes intensify, thus, nuclei heavier than ^{7}Li and ^{7}Be – which are result of $\alpha + \alpha$ reactions – have a negligible abundance.

The destruction of heavy nuclei before reaching the hottest and densest part, will suppress the γ-ray line emissivity of the ADAF. Hence, it will lower the disk efficiency of converting accretion energy into γ-ray lines.

In figs. 4.2 to 4.5 are shown also the emissivities of ADAF and SLE. One can see that a part of the nuclear γ-ray lines can be screened by the electron thermal bremsstrahlung. The blue lines represents the nuclear emission. We can see the continuum which is dominated by the nuclear Bremsstrahlung and on top of it, are the Doppler broadened nuclear lines. The thermal π^0 emission is shown with the cyan dash-line.

The ADAF model temperature is very close to the virial temperature and it remains so high for a wide range of parameters. This allows the luminosities to be scaled as $L \sim \rho \times R^3 \sim m\,\dot{m}^2\,\alpha^{-2}$. This scaling is valid far for parameters far from critical ones. For the ADAF we have the following relations:

$$L_e = (1 - f) \times L_{acc} \tag{4.1}$$

$$L_N \sim 3 \times 10^{31}\, m_{(1)}\, \dot{m}^2_{(-3)}\, \alpha^{-2}_{(-1)} \quad \mathrm{erg\ s^{-1}} \tag{4.2}$$

$$L_\pi \sim 3 \times 10^{33}\, m_{(1)}\, \dot{m}^2_{(-3)}\, \alpha^{-2}_{(-1)} \quad \mathrm{erg\ s^{-1}} \tag{4.3}$$

Where L_N is the γ-ray luminosity due to nuclear γ-ray lines, p–n capture and bremsstrahlung; L_π is the γ-ray luminosity due to production and decay of π^0-meson.

Note however,that there will be an upper limit on the luminosities due to the critical value of the accretion rate $\dot{m}_c \approx 0.2\,\alpha^2$, beyond which ADAF most likely do not exist (see e.g. Narayan and Yi, 1995*a*). Therefore, the luminosity of a solar initial composition plasma cannot be higher than:

$$L_N \leq 1 \times 10^{33}\, m_{(1)}\ \mathrm{erg\ s^{-1}}$$

$$L_\pi \leq 1 \times 10^{35}\, m_{(1)}\ \mathrm{erg\ s^{-1}}\ .$$

The upper limit is taken assuming $\alpha = 0.3$, $\dot{m} = 0.17\alpha^2$. This limit on the γ-ray lines luminosity is about an order of magnitude higher than the calculations of Yi and Narayan (1997).

For the SLE model, is cold to produce π^0 and its nuclear γ-ray luminosity cannot be higher than:

$$L_N \leq 6 \times 10^{32}\, m_{(1)} \text{ erg s}^{-1} \ ,$$

where the upper limit is taken for $\alpha = 0.3$, $\dot{m} = 0.17\alpha^2$.

For a plasma with higher mass fraction abundance of initial heavy elements $X_p = X_\alpha = 0.3$ and $X_{C12} = X_{O16} = 0.2$, the upper limits shift to

$$\text{ADAF} \left| \begin{array}{ll} L_N \leq 8 \times 10^{33}\, m_{(1)} & \text{erg s}^{-1} \\ L_\pi \leq 5 \times 10^{34}\, m_{(1)} & \text{erg s}^{-1} \end{array} \right. \tag{4.4}$$

$$\text{SLE} \left| \begin{array}{ll} L_N \leq 1 \times 10^{34}\, m_{(1)} & \text{erg s}^{-1} \end{array} \right. \tag{4.5}$$

Tables 4.1 and 4.2 summarize the accretion γ-ray luminosities for the two sets of parameters chosen here.

Table 4.1: ADAF and SLE luminosities for $\alpha = 0.1$, $\dot{m} = 10^{-3}$, $m = 10$ and $\beta = 0.5$. The advection parameter is $f = 0.86$ and the accretion luminosity is $L_{acc} = 1.4\, 10^{36}$ erg s^{-1}.

	Solar	Composition	
Model	L_e (erg s^{-1})	L_N (erg s^{-1})	L_π (erg s^{-1})
ADAF	$1.8\, 10^{35}$	$3.1\, 10^{31}$	$3.3\, 10^{33}$
SLE	$9.4\, 10^{35}$	$5.6\, 10^{30}$	0

Table 4.2: ADAF and SLE luminosities for $\alpha = 0.3$, $\dot{m} = 0.17\alpha^2$, $m = 10$ and $\beta = 0.5$. The advection parameter is $f = 0.56$ and the accretion luminosity is $L_{acc} = 2.1\, 10^{37}$ erg s^{-1}. The first table here shows the results for a Solar composition plasma and the second one for $X_p = X_\alpha = 0.3$ and $X_{C12} = X_{O16} = 0.2$.

	Solar	Composition	
Model	L_e (erg s^{-1})	L_N (erg s^{-1})	L_π (erg s^{-1})
ADAF	$9.3\, 10^{36}$	$9.8\, 10^{32}$	$1.1\, 10^{35}$
SLE	$7.6\, 10^{36}$	$5.9\, 10^{32}$	0
	H-He-C-O	Composition	
Model		L_N (erg s^{-1})	L_π (erg s^{-1})
ADAF		$8\, 10^{33}$	$4.7\, 10^{34}$
SLE		$1.2\, 10^{34}$	0

For the case where the plasma is unable to develop a Maxwellian distribution tail, two extreme modifications of the distribution tail are shown in

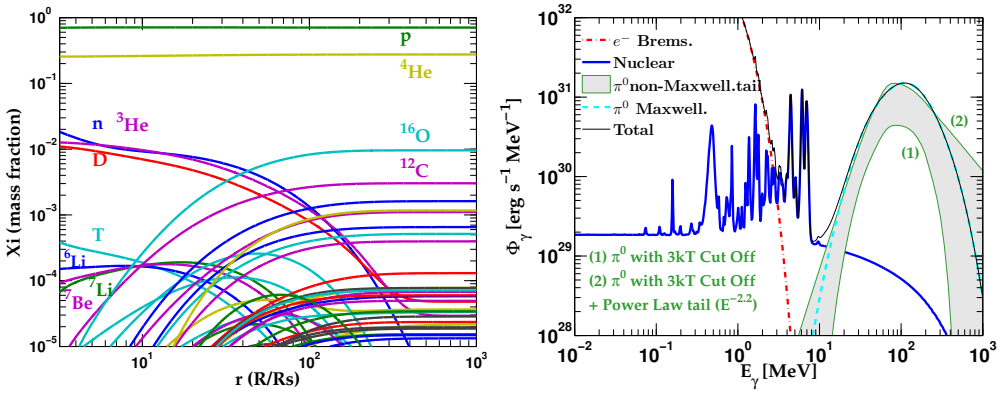

Figure 4.2: The ADAF model for a black hole of mass $m = 10$, $\alpha = 0.1$, accretion rate $\dot{m} = 10^{-3}$ and $\beta = 0.5$. The figure on the left shows the plasma abundances evolution during its fall toward the black hole. The initial plasma composition is the solar composition. The figure on the right is the emissivity of the disk. The red dash-line is the emissivity of the thermal electron bremsstrahlung. The blue-line is the emissivity of nuclear interactions composed by: The nuclear lines, the nuclear capture and the nuclear bremsstrahlung. The cyan-line is the emissivity due to thermal π^0 production. The lines (1) and (2) and the shaded area they enclose, are the possibilities where the emissivity of the $\pi^0 \rightarrow 2\gamma$ should lie in the case when plasma has not been able to develop the Maxwellian distribution tail. The line (1) is the emissivity due to π^0 production for the Maxwellian distribution tail that is cut off at energy $3\,k_B T_i$. The line (2) is the emissivity for the Maxwellian distribution tail that is cut off at energy $3\,k_B T_i$ and is replaced with a power law tail of index 2.2. The advection factor for this model is $f = 0.86$ and the accretion luminosity is $L_{acc} = 1.4 \times 10^{36}$ erg s^{-1}. The luminosity that the electrons radiate away is $L_e = 1.8 \times 10^{35}$ erg s^{-1}, the luminosity that disk radiate through nuclear lines and continuum is $L_N = 3.1 \times 10^{31}$ erg s^{-1} and the luminosity radiated through thermal π^0 production is $L_\pi = 3.3 \times 10^{33}$ erg s^{-1}.

fig. 4.2. The curve (1) is calculated for a Maxwellian distribution with a cut off at $3\,k_B T_i$. The curve (2) for a Maxwellian distribution with a power-law suprathermal component with index $\delta = 2.2$.

Figures 4.6 and 4.7 show the $E_\gamma \times \Phi_\gamma$ as a function of E_γ for the solutions presented in figs. 4.2 to 4.5. The ADAF $E_\gamma \times \Phi_\gamma$ function shows three interesting features: the thermal electron bremsstrahlung "bump", the nuclear lines and the π^0 "bump". The same feature, except for the π^0 "bump" are present in the plasma emissivity of the SLE model.

The ADAF is very hot, thus the secondary neutrons have energy high enough to overcome gravity and effectively escape from the accretion disk. The ratio between the amount of neutrons that manage to escape against the original amount of neutrons is called evaporation efficiency and denoted with η. The evaporation efficiency η for the ADAF model is shown in fig. 4.8. As we can see from this figure, the ADAF can effectively expel neutrons with

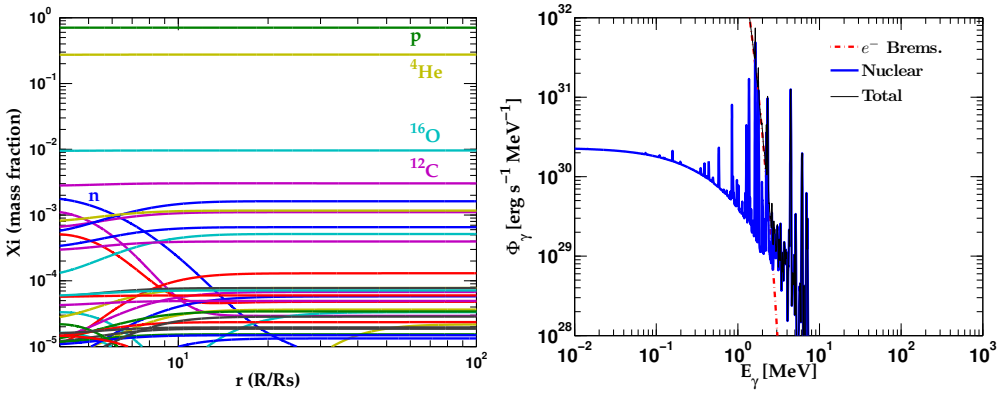

Figure 4.3: The SLE model for a black hole of mass $m = 10$, $\alpha = 0.1$, accretion rate $\dot{m} = 10^{-3}$ and $\beta = 0.5$. The figure on the left, shows the plasma abundances evolution during its fall toward the black hole. The initial plasma composition is the solar composition. The right figure is the γ-ray emissivity of the disk. The red dash-line is the emissivity of the thermal electron bremsstrahlung. The blue-line is the emissivity of the nuclear interactions composed by: The nuclear lines, the nuclear captures and the nuclear bremsstrahlung. This model is very cold to produce π^0-mesons. The accretion luminosity of this model is $L_{acc} = 1.4 \times 10^{36}$ erg s^{-1}. The luminosity that electrons radiate away is $L_e = 9.4 \times 10^{35}$ erg s^{-1} whereas the luminosity due to nuclear γ-rays is $L_N = 5.6 \times 10^{30}$ erg s^{-1} (the $L_\pi = 0$).

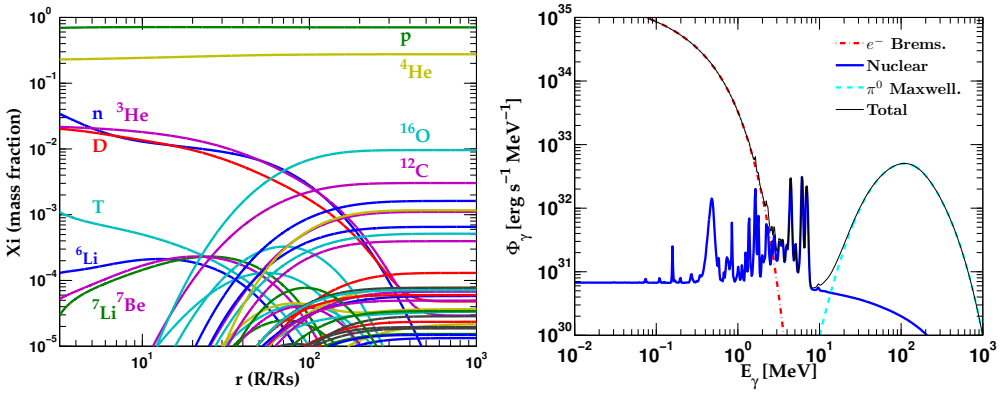

Figure 4.4: The ADAF model for a black hole of mass $m = 10$, $\alpha = 0.3$, accretion rate $\dot{m} = 1.7 \times \alpha^2 = 1.53 \times 10^{-2}$ and $\beta = 0.5$. The advection factor of this model is $f = 0.56$; whilst, the accretion luminosity is $L_{acc} = 2.1 \times 10^{37}$ erg s^{-1}. The figure on the left shows the plasma abundances evolution during its fall toward the black hole. The initial plasma chemical composition is the solar composition. The figure on the right, is the emissivity of the disk. The red dash-line is the emissivity of the thermal electron bremsstrahlung. The blue-line is the emissivity of the nuclear interactions composed by: The nuclear lines, the nuclear capture and the nuclear bremsstrahlung. The cyan-line is the emissivity due to thermal π^0 production. The luminosity through nuclear lines and continuum is $L_N = 9.1 \times 10^{32}$ erg s^{-1}; whereas, the luminosity radiated through thermal π^0 production is $L_\pi = 1.0 \times 10^{35}$ erg s^{-1}.

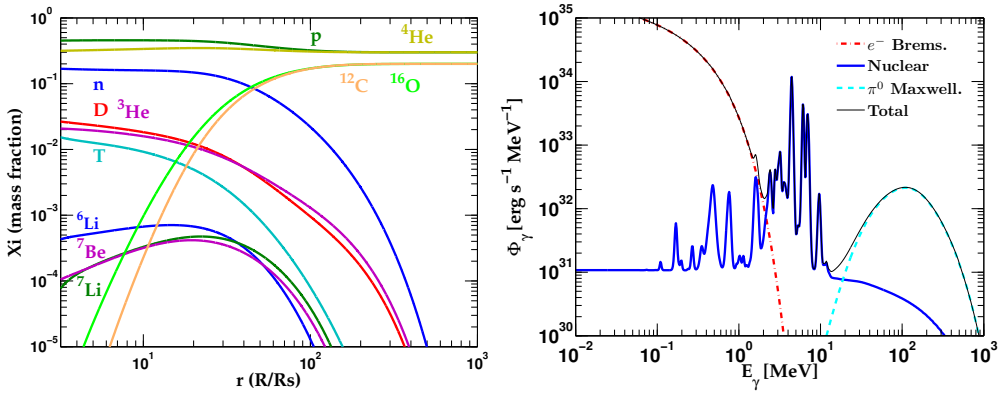

Figure 4.5: The ADAF model for a black hole of mass $m = 10$, $\alpha = 0.3$, accretion rate $\dot{m} = 1.7 \times \alpha^2 = 1.53 \times 10^{-2}$ and $\beta = 0.5$. The advection factor $f = 0.56$ and the accretion luminosity is $L_{acc} = 2.1 \times 10^{37}$ erg s^{-1}. The figure on the left shows the plasma abundances evolution during its fall toward the black hole. The initial mass fraction abundances are $X_p = X_\alpha = 0.3$ and $X_{C12} = X_{O16} = 0.2$. In the figure are shown only n, p, D, T, ^{3}He, ^{4}He, ^{6}Li, ^{7}Li, ^{7}Be, ^{12}C and ^{16}O. No intermediate elements are shown. The figure on the right is the emissivity of the disk. The red dash-line is the emissivity of the thermal electron Bremsstrahlung. The blue-line is the emissivity of the nuclear interactions composed by: he nuclear lines, the nuclear capture and the nuclear bremsstrahlung. The cyan-line is the emissivity due to thermal π^0 production. The luminosity through nuclear lines and continuum is $L_N = 7.5 \times 10^{33}$ erg s^{-1} and the luminosity radiated through thermal π^0 production is $L_\pi = 4.3 \times 10^{34}$ erg s^{-1}.

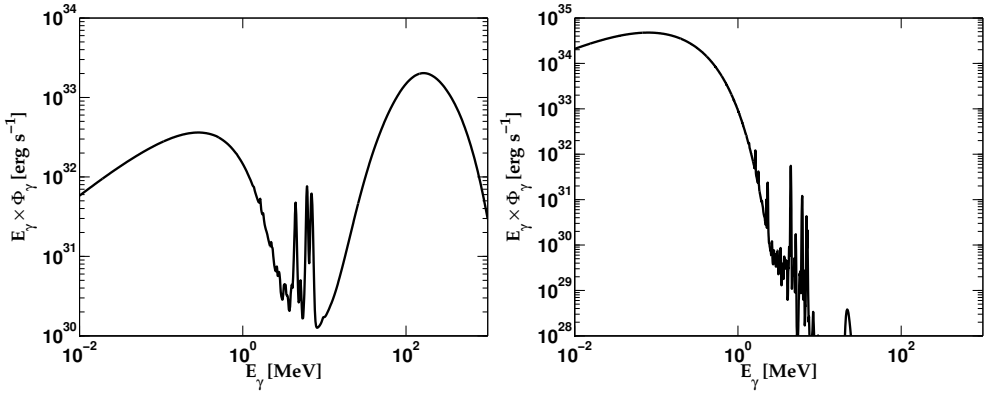

Figure 4.6: The $E_\gamma \times \Phi_\gamma$ function of the E_γ. On the left it is shown the ADAF model; whilst, on the right the SLE model. The disk parameters are $m = 10$, $\alpha = 0.1$, $\dot{m} = 0.1\alpha^2$ and $\beta = 0.5$. The initial plasma chemical composition is the Solar composition.

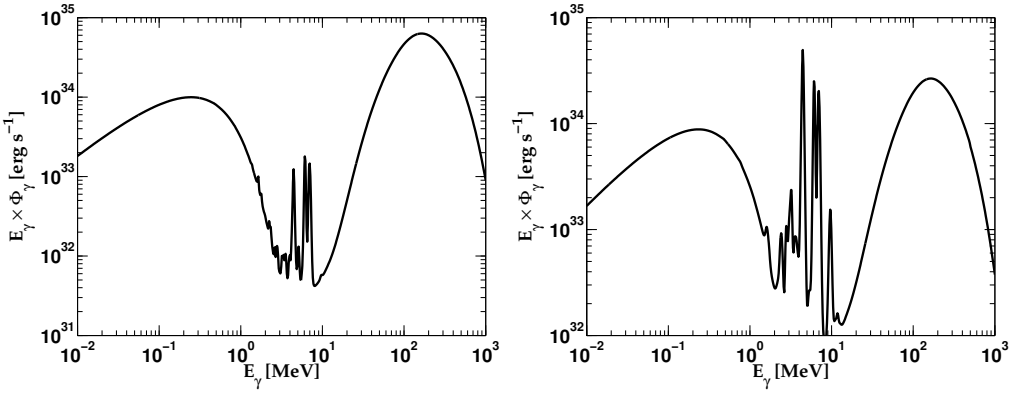

Figure 4.7: The $E_\gamma \times \Phi_\gamma$ as a function of E_γ for the ADAF model. The disk parameters are $m = 10$, $\alpha = 0.3$, $\dot{m} = 0.17\alpha^2 \approx 1.5 \times 10^{-2}$ and $\beta = 0.5$. The initial plasma chemical composition are: for the figure on the left, solar composition; for the figure on the right, initial mass fraction abundances are $X_p = X_\alpha = 0.3$ and $X_{C12} = X_{O16} = 0.2$.

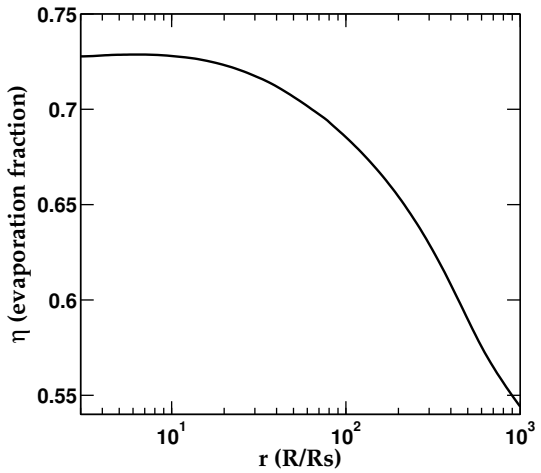

Figure 4.8: The evaporation efficiency η for an ADAF models as a function of radius. The disk parameters for this example are $m = 10$, $\alpha = 0.1$, $\dot{m} = 10^{-3}$ and $\beta = 0.5$. However, this function is universal, and it does not depend on the accretion parameters.

an efficiency $\eta \approx 70$ % for $r < 100$.

The source of the neutrons in the accretion plasma are the nuclear breakup reactions. This process starts around $r \approx 100$. For the innermost part of the ADAF accretion disk $r < 10$, the temperatures become very high and neutrons are produced also in p–p interactions, through $p + p \rightarrow p + n + \pi^+$.

The neutron abundance is proportional to the plasma density and inverse proportional to the plasma radial speed; therefore it scales like $\frac{dX_n}{dr} \sim \rho\, v_r^{-1} R_s \sim \dot{m}\,\alpha^{-2}$. For a given radius the neutrons abundance will scale the

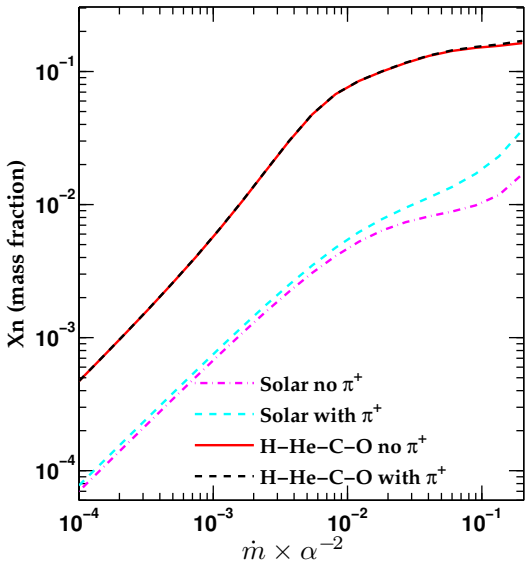

Figure 4.9: The neutron abundance predicted by the ADAF model at $r = 3.1$. The neutron mass fraction abundance is a function of $\dot{m}$ and α. For low accretion rate the mass fraction abundance is proportional with $X_n \propto \dot{m}\,\alpha^{-2}$. Here the parameters are $m = 10$ and $\beta = 0.5$, however the neutrons abundance does not depend on them. The red-line and the black-dash-line have a Solar initial composition, whereas the the cyan-line and the blue-dash-line have $X_p = X_\alpha = 0.3$ and $X_{C12} = X_{O16} = 0.2$ initial composition. The solar abundance has more protons therefore $p + p \rightarrow p + n + \pi^+$ is more important than in the other higher metallicity composition case.

same way; thus, $X_n \sim \dot{m}\,\alpha^{-2}$ and the proportionality constant is a function of radius. Note that this is valid far from the critical parameters such as the critical accretion rate $\dot{m}_c$. The neutron abundance does not depend on the black hole mass. Figure 4.9 shows the $X_n = f(\dot{m}\,\alpha^{-2})$ dependence at $r = 3.1$ for the ADAF model. There it is estimated the role of $p + p \rightarrow p + n + \pi^+$ reaction from the nuclear breakup ones, thus they are shown separated. The $p + p \rightarrow p + n + \pi^+$ reaction will clearly affect the case were the protons are more abundant. Two initial compositions have been considered: the Solar composition of elements and the one with $X_p = X_\alpha = 0.3$ and $X_{C12} = X_{O16} = 0.2$.

Some accretion disks, due to a positive Bernoulli integral, can have outflows. ADAF accretion is one of these models (e.g. Narayan and Yi, 1994; Yi and Narayan, 1997). This outflow can carry some of the accretion material and expel it into the interstellar medium. The accretion material is richer with light elements such as Li and Be; thus, this could be a possible way of enhancement of the content of the light elements in additional to the primordial (Cosmological) Li and Be. Thus, it can contribute to the so

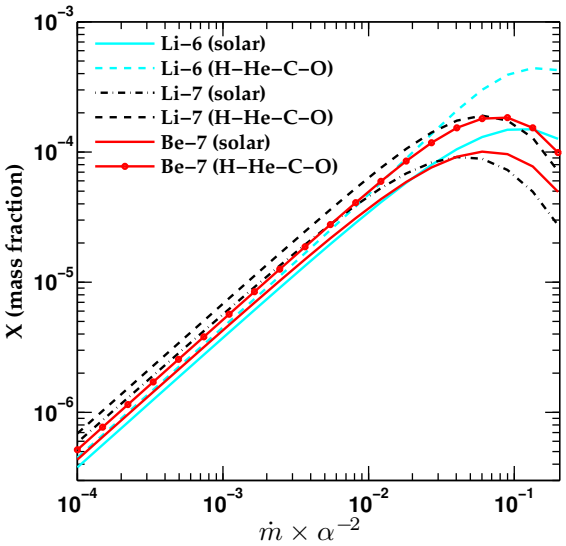

Figure 4.10: The mass fraction abundances of ^{6}Li, ^{7}Li and ^{7}Be predicted by ADAF model at $r = 3.1$. Their mass fraction abundances are a function of $\dot{m}$ and α. For low accretion rate the mass fraction abundance is proportional to $\dot{m}\,\alpha^{-2}$. For this example, I have chosen $m = 10$ and $\beta = 0.5$, although the abundances do not depend on them. The "solar" plots means Solar initial composition, whereas plots with "H–He–C–O" have $X_p = X_\alpha = 0.3$ and $X_{C12} = X_{O16} = 0.2$ initial composition.

called, primordial lithium problem (see e.g. Fields, 2011). Figure 4.10 shows the mass fraction abundance of ^{6}Li, ^{7}Li and ^{7}Be as a function of $\dot{m}\ \alpha^{-2}$, for an ADAF plasma close to the last stable orbit ($r = 3.1$). The calculations are performed for the solar initial composition and for $X_p = X_\alpha = 0.3$ and $X_{C12} = X_{O16} = 0.2$ initial composition. For a given expelling rate one can calculate the mass rate expelled from each of these elements.

4.4 Discussion

4.4.1 Nuclear reactions and abundances

The $r > 100$ region of the accretion disk is not important for nuclear reactions. There the densities and temperatures are very low, thus the nuclear reaction rates are insignificant. Generally, closer to the black hole the temperature and density increase, consequently the nuclear reaction rate increase dramatically.

Due to very high temperatures, ADAF accretion shows a subregion between $3 < r < 20$. In this region the π-meson production starts to become important; thus the $p + p \rightarrow p + p + \pi^0$ reaction produces γ-rays through $\pi^0 \rightarrow 2\gamma$ decay; whilst, the reaction $p + p \rightarrow p + n + \pi^+$ converts protons to

neutrons. The SLE is not hot enough to produce π-mesons.

In the accretion plasmas, moving toward the accretion center, heavy nuclei become lesser abundant due to the breakup reactions. For some accretion disk parameters – close to critical parameters such as the critical accretion rate – heavy nuclei may be fully destroyed; as a result, isotopes of Hydrogen and Helium become more abundant. We find that in the innermost part of the disk isotopes of Lithium and Beryllium are abundant due to $\alpha + \alpha$ reactions. Figures 4.2 to 4.5 show the abundances evolution with the disk radius, in particular fig. 4.10 shows the abundances of ^{6}Li, ^{7}Li and ^{7}Be mass fraction abundances as a function of $\dot{m}\,\alpha^{-2}$ for the ADAF regime.

On the other hand, SLE is colder but has a density an order of magnitude higher than ADAF. Although this enhances the nuclear reaction rates and increases the luminosities, the heavy nuclei are destroyed less efficiently.

Figure 4.9 shows the mass fraction abundance of neutrons at the ADAF's last stable orbit. The neutron mass fraction abundance for solar initial composition can become as high as $X_n \lesssim 10^{-2}$; however, higher metallicity plasma can increase the abundance by one order of magnitude. This is shown in fig. 4.5. Also, the π-meson production can help to increase the neutron abundance.

Depending on the ADAF initial chemical composition, the mass fraction abundances of the D and ^{3}He are of the order $X \sim 10^{-2}$. The source of these elements is basically the $p + \alpha$ reaction.

The mass fraction abundance of T depends crucially from the abundance of neutrons and ^{4}He, which are provided in the reaction $n + \alpha \rightarrow T + D$.

The abundances of ^{6}Li, ^{7}Li and ^{7}Be depends especially on the ^{4}He abundances because, $\alpha + \alpha$ reaction works effectively in the ADAF accretion flows, cf. fig. 4.10. The isotopes of Li and Be are fragile nuclei they are easily destroyed in the plasma. For accretion rates close to critical one, their abundances peak somewhere between $10 - 30\ R_s$. For $r < 10$ the destruction processes start to become important by lowering the Li and Be abundances.

4.4.2 The γ-ray spectra and luminosity

The γ-ray emissivity of the accretion disks are shown in figs. 4.2 to 4.5. Nuclear γ-rays are a contributed by nuclear lines, nuclear bremsstrahlung, neutron capture and γ-rays from π^0 production.

Both ADAF and SLE accretion disk models have electron temperatures $k_B T_e < 0.3$ MeV, thus, thermal electron Bremsstrahlung almost screens all nuclear lines with $E_\gamma < 2$ MeV. The nuclear lines that are in principle possible to detect lies in the interval $2 < E_\gamma < 10$ MeV. The γ-rays with $E_\gamma > 10$ MeV are due to π^0 production. The SLE γ-ray spectra shows a cut off at $E_\gamma \approx 10$ MeV

depending on the chemical composition.

Both ADAF and SLE models have about the same efficiency of converting accretion energy into nuclear γ-ray lines, $L_N/L_{acc} < 6 \times 10^{-4}$. However, ADAF due to high temperatures produces more effectively π^0-mesons. The π^0 production has an efficiency $L_\pi/L_{acc} < 10^{-2}$.

In principle, the measurement of the disk nuclear lines profile would give us unique information about disk physical parameters such as: chemical composition, density, temperature, accretion rate etc. The calculations here take into account the Doppler broadening of nuclear lines due to the thermal motion of excited nuclei. This full width at the half maximum (FWHM) ratio with the central energy is:

$$\frac{\Delta E_\gamma}{E_\gamma} \approx 2.35 \sqrt{\frac{k_B T_i}{M c^2}} \approx 0.24 \times \sqrt{\frac{T_{(1)}}{A}}$$

where M is the excited nucleus mass, A is the nucleus mass-number; $T_{(1)}$ is the temperature in units of 10 MeV.

The SLE is much colder than ADAF therefore its nuclear lines are narrower and higher, whereas ADAF nuclear lines are wider with $\Delta\nu/\nu \sim 0.08$.

4.4.3 Modified Maxwellian distribution

In the framework of ADAF, accretion plasma may not be in thermal equilibrium. Therefore, protons as well as other ions may not be able to develop their Maxwellian distribution tail. On the other hand, even a slight acceleration of the plasma particles lead to formation of suprathermal (power law) tail above the Maxwellian distribution.

Figure 4.2 shows the γ-ray emissivity calculated for two proton distribution tails. The γ-ray spectra due to π^0 production will be somewhere in the shaded area between curve (1) and (2) in the fig. 4.2.

Both, γ-ray lines and γ-rays from π^0 production, are great observational tools to distinguish between different accretion models/regimes. By measuring the γ-ray line width we would get information about the proton temperature. Also, by measuring the π^0 decay γ-ray spectral shape we gain important information about protons distribution shape.

4.4.4 Evaporation of neutrons

Neutron are not bounded by electric or magnetic accretion disk fields; therefore, if neutrons have enough energy to overcome gravity potential of the black hole, they can escape from the disk. ADAF is very hot, thus if neutrons are thermalized at such high temperatures they can easily escape from the disk almost isotropically. ADAF is optically thin with respect to neutrons.

Figure 4.8 shows the evaporation efficiency η as a function of the disk radius. The efficiency profile is quite universal for $r < 100$ because it depends mainly on the disk temperature profile which is approximately virial temperature for a wide range of the accretion parameters. In this condition about 70% of the disk's neutrons can escape. Depending on the accretion parameters and the initial composition, ADAF accretion model allows an escape of neutrons with a rate $0.15 \times \dot{M}$.

A non-negligible contribution to neutron production comes from the reaction $p + p \rightarrow p + n + \pi^+$ inside the region $3 < r < 10$.

4.4.5 Evaporated neutrons interacting with the companion star atmosphere

Solar mass black holes with an accretion disk, are usually observed in binary systems. If the accretion regime is an ADAF and if the disk neutrons managed to escape, they can reach the companion star atmosphere. Neutrons will scatter off nuclei from the star atmosphere, until they loose their energy and eventually are captured by protons. Neutrons can also interact with CNO nuclei and can breakup them.

The result of neutron interactions with the star atmosphere are the production of 2.2 MeV γ-rays from hydrogen capture and the production of light elements such are D, Li and Be in the star atmosphere.

The detection of the 2.2 MeV γ-rays from the companion star and/or the observation of unexpected high abundances of the light elements in the companion star atmosphere or in the interstellar medium that surrounds the binary system would be a secondary signal for the existence of a high temperature plasma in that system.

4.4.6 Metallicity effect on the γ-ray luminosity and the neutron production

Due to higher reaction threshold and high excitation energy, the $p + \alpha$ and $\alpha + \alpha$ reactions are less effective in producing neutrons and γ-ray lines than heavy nuclei. Figure 4.5 demonstrate an example of a plasma with initially high content of heavy elements, $X_p = X_\alpha = 0.3$ and $X_{C12} = X_{O16} = 0.2$. It is shown that neutron abundance and the γ-ray lines luminosity can be increased with at least an order of magnitude compare to the case of a solar composition plasma.

The increase of the accretion rate close to the critical one, will increase the amount of neutrons but will not necessary increase with the same proportions the γ-ray lines luminosity. This is true because the quicker we destroy

heavy nuclei, the innermost part of the disk – which is the hottest and the most dense part – will not be able to radiate γ-ray lines. Thus the efficiency of converting accretion to γ-ray lines will decrease.

4.4.7 Li-production

The so called, the Lithium problem, involves the unexplained abundances of the ^{6}Li and ^{7}Li that are measured in metal-poor stars (e.g. Fields, 2011). Observations show that ^{6}Li is over-abundant whereas ^{7}Li is under-abundant compare to predictions of the big-bang nucleosynthesis. There are many hypothesis of how to solve this problem; they involve three directions: Cosmology, astrophysics and beyond standard model physics.

It is possible that very hot accretion plasmas might play a role in the solution of the Lithium problem. In particular ADAF models have positive Bernoulli integral; thus, if they can produce Li in the disk, the outflows can carry it and expel to the surrounding media and contaminate it.

Recently, by using a simplified tori-model for a solar mass black hole, the Iocco and Pato (2012) predicted a large amount of Li from such systems. The amount of Li expelled from such a system can contaminate the entire Galaxy. It seems, however that this model is too simplified and should suffer the same limitations as the ADAF models do. At high accretion rates ($\dot{m} > 0.3\alpha^2$) the ions will be effectively cooled down such that their temperature will be too low to initiate effective nuclear reactions. Apparently, Iocco and Pato (2012) overestimate the maximal accretion rate of the hot plasma by a factor of 100.

4.5 Summary and Conclusions

In this chapter it is investigated the evolution of the accretion disk abundances and γ-ray emissivities for two accretion disk models, namely ADAF and SLE.

The accretion disk which operates in the ADAF regime, has relatively low γ-rays emissivity; therefore, it might be difficult to observe them with the current detectors. However, the next generation of the MeV-γ-ray instruments allow us to test these predictions and thus to open a new window on the physics of these objects.

The γ-ray emissivity spectra from the accretion plasma show three distinct features: The electron thermal bremsstrahlung, the nuclear lines and in the case of very hot ADAF accretion, the γ-rays from π^0 production. The detectable nuclear lines lie in the interval $2 < E_\gamma < 10$ MeV. The π^0 production γ-ray spectra become noticeable for $E_\gamma > 10$ MeV.

Different part of the MeV-γ-ray spectra carry important information for different physical parameters. The measurement of nuclear γ-ray lines profile give a unique information about the temperature, chemical composition, accretion rate etc. From $E_\gamma > 100$ MeV spectra, we can extract information about the proton distribution shape, in particular its deviation from the Maxwellian distribution.

Depending on the accretion parameters and the initial chemical composition, the γ-ray luminosities for ADAF can reach quite high values: for the nuclear lines and continuum, $L_N \sim 8\times10^{33}\, m_{(1)}$ erg s^{-1} and for the γ-rays from π^0 production, $L_\pi \sim 1\times10^{35}\, m_{(1)}$ erg s^{-1}. The SLE nuclear lines and continuum luminosity can reach values as high as $L_N \sim 1\times10^{34}\, m_{(1)}$ erg s^{-1}. At the same time, SLE cannot provide effective production of π^0 decay γ-ray emission.

The SLE accretion model is cold to be able to emit a considerable amount of neutrons. However, the ADAF model is very hot and neutrons can effectively escape the disk. The neutron escape efficiency for ADAF accretion disk has a universal profile which is valid for a wide range of disk parameters. Depending on the initial composition and the accretion parameters, the neutron mass fraction abundance can be as high as $X_n \approx 0.2$; therefore, the total amount of neutrons that can be expelled from the ADAF accretion disk might be as large as $0.15\times\dot{M}$.

Neutrons that escape the disk and reach the companion star atmosphere, initiate nuclear interactions there. The result of these interactions might be the breakup of the CNO nuclei which will produce light elements, or it can scatter off in the star atmosphere until is cooled down and captured by hydrogen with production of Deuterium and 2.2 MeV γ-ray line. The abundances are possible to contaminate the interstellar environment that surrounds the binary system, through the companion star solar winds. The light elements that are produce in the accretion disk can escape through disk outflows and enhance the abundance of the interstellar medium.

5 Summary and Conclusions

The gamma-ray emissivity of very hot optically thin plasma with ion temperature $T \geq 10^{10}$K has been quantitatively studied for the first time. The calculations are based on a comprehensive network of nuclear reactions. At ion temperatures up to several tens of MeV, the plasma emissivity initially is dominated by de-excitation lines. The emissivity depends on the chemical composition of plasma. However, because of spallation reactions, the chemical composition experiences strong evolution. Correspondingly, both the spectral shape and the absolute emissivity evolve in time with gradual reduction of contribution of heavy elements to gamma-ray production. On timescales exceeding the characteristic time of nuclei destruction (which is a strong function of ion temperature), the plasma consists of protons and neutrons with a small fraction of D, T and ^{3}He. At this stage, proton–neutron plasma radiates through p–n bremsstrahlung as well as through gamma-rays at the capture of neutrons by protons.

At ion temperatures exceeding several tens of MeV, plasma starts to cool radiatively due to inelastic p–p interactions. These interactions produce π^0-mesons which quickly decay to two high energy photons. If the ion temperature is lower than the threshold energy of π^0 production, only protons from the "tail" of distribution ($E \gg kT$) contribute to the gamma-ray production. Generally, particles in thermal plasma are well described by Maxwellian distribution. However, in realistic astrophysical scenarios one may expect significant deviations from Maxwellian distribution. Namely, when the characteristic time of elastic p–p interactions is too long (longer than the accretion time) to establish a developed Maxwellian "tail", the production of π^0-mesons would be strongly suppressed. On the other hand, even a modest particle acceleration, for example by plasma waves, can lead to a suprathermal (typically, power-law) component of particle distribution well above the Maxwellian "tail". This might dramatically increase the π^0 production rate, and consequently the gamma-ray luminosity.

The importance of these two effects, which may have strong impact on the detectability of gamma-radiation from astrophysical objects containing very hot two–temperature plasma, are demonstrated by detailed numerical calculations. The nuclear reaction network has been applied to different models of two–temperature plasma around an accreting black hole – ADAF and SLE. The chemical composition evolution and the γ-ray emissivity of accretion disks are calculated for a wide range of parameters and initial chemical compositions of plasma. Very hot plasma with an ion temperature close to 100 MeV achievable in the ADAF accretion regime, could be marginally detected by Fermi LAT telescope and future low-energy gamma-ray detectors.

The ADAF regime also predicts effective production of neutrons and their evaporation from the accretion disk. A significant fractions of these neutrons can be captured by the atmosphere of the companion star, leading to production of Deuterium as well as light elements (Li, Be, B) through spallation of CNO nuclei. The stellar wind can transport this material and enhance the interstellar medium by light elements. The contribution of this non-cosmological channel to the content of light elements in the Universe could be quite significant and deserves further exploration in the context of the so-called problem of underproduction of light elements, in particular Deuterium and ^{7}Li, in the Big Bang paradigm.

Bibliography

Abramowicz M A, Chen X, Kato S, Lasota J P and Regev O (1995). Thermal equilibria of accretion disks, ApJ **438**, L37–L39.

Abramowicz M A, Czerny B, Lasota J P and Szuszkiewicz E (1988). Slim accretion disks, ApJ **332**, 646–658.

Abramowicz M A, Lasota J P and Igumenshchev I V (2000). On the absence of winds in advection-dominated accretion flows, MNRAS **314**, 775–781.

Agakishiev G, Alvarez-Pol H, Balanda A and *et. al.* (2012). Study of exclusive one-pion and one-eta production using hadron and dielectron channels in pp reactions at kinetic beam energies of 1.25 GeV and 2.2 GeV with HADES, *European Physical Journal A* **48**, 74.

Aharonian F A and Atoyan A M (1983). Time evolution of the particle distribution function in a high-temperature plasma, *JETP* **58**, 1079.
URL: *http://www.jetp.ac.ru/cgi-bin/e/index/r/85/6/p1857?a=list*

Aharonian F A and Atoyan A M (2000). Broad-band diffuse gamma ray emission of the galactic disk, A&A **362**, 937–952.

Aharonian F A and Sunyaev R A (1984). Gamma-ray line emission, nuclear destruction and neutron production in hot astrophysical plasmas - The deuterium boiler as a gamma-ray source, MNRAS **210**, 257–277.

Aharonian F A and Sunyaev R A (1987). Synthesis of light nuclei in a two-temperature astrophysical plasma, *Astrophysics* **27**, 413–422.

Aikawa M, Arnould M, Goriely S, Jorissen A and Takahashi K (2005). BRUSLIB and NETGEN: the Brussels nuclear reaction rate library and nuclear network generator for astrophysics, A&A **441**, 1195–1203.

A.J. Koning S H and Duijvestijn M (2007). TALYS-1.0, pp. 211 – 214.
URL: *http://www.talys.eu/*

Alons P W F, Kraushaar J J, Shepard J R, Cameron J M, Hutcheon D A, Liljestrand R P, McDonald W J, Miller C A, Olsen W C, Tinsley J R and Stronach C E (1986). $^4(\vec{p}$,d)^{3}He reaction at 200 and 400 MeV, Phys. Rev. C **33**, 406–411.

Alpher R A, Bethe H and Gamow G (1948). The Origin of Chemical Elements,

Physical Review **73**, 803–804.

Anders E and Grevesse N (1989). Abundances of the elements - Meteoritic and solar, Geochim. Cosmochim. Acta **53**, 197–214.

Ashkin J and Marshak R E (1949*a*). Bremsstrahlung in High Energy Nucleon-Nucleon Collisions, *Physical Review* **76**, 58–60.

Ashkin J and Marshak R E (1949*b*). Erratum: Bremsstrahlung in High Energy Nucleon-Nucleon Collisions, *Physical Review* **76**, 989–989.

Auce A, Carlson R F, Cox A J, Ingemarsson A, Johansson R, Renberg P U, Sundberg O, Tibell G and Zorro R (1994). Reaction cross sections for 75-190 MeV alpha particles on targets from ^{12}C to ^{208}Pb, Phys. Rev. C **50**, 871–879.

Bauer W, Bertsch G F, Cassing W and Mosel U (1986). Energetic photons from intermediate energy proton- and heavy-ion-induced reactions, Phys. Rev. C **34**, 2127–2133.

Bauer W, Cassing W, Mosel U, Tohyama M and Cusson R Y (1986). High energy γ-ray emission in heavy-ion collisions, *Nuclear Physics A* **456**, 159–172.

Belyanin A A and Derishev E V (2001). Formation and dynamics of self-sustained neutron haloes in disk accreting sources, A&A **379**, L25–L29.

Beringer J, Arguin J F, Barnett R M and *et. al.* (2012). Review of Particle Physics, *Phys. Rev. D* **86**, 010001.
URL: *http://link.aps.org/doi/10.1103/PhysRevD.86.010001*

Bethe H A (1939). Energy Production in Stars, *Phys. Rev.* **55**, 434–456.
URL: *http://link.aps.org/doi/10.1103/PhysRev.55.434*

Bildsten L, Salpeter E E and Wasserman I (1992). The fate of accreted CNO elements in neutron star atmospheres - X-ray bursts and gamma-ray lines, ApJ **384**, 143–176.

Bisnovatyi-Kogan G S, Khlopov M Y, Chechetkin V M and Eramzhyan R A (1980). Gamma-Ray Emission during Gas Accretion onto a Neutron Star, Soviet Ast. **24**, 716.

Bisnovatyi-Kogan G S, Zel'dovich Y B and Syunyaev R A (1971). Physical Processes in a Low-Density Relativistic Plasma., Soviet Ast. **15**, 17.

Blandford R D and Begelman M C (1999). On the fate of gas accreting at a low rate on to a black hole, MNRAS **303**, L1–L5.

Bondar A, Calén H, Carius S and *et. al.* (1995). The $pp \to pp\pi^0$ reaction near the kinematical threshold, *Physics Letters B* **356**(1), 8 – 12.
URL: *http://www.sciencedirect.com/science/article/pii/037026939500794L*

Bunch S, Forster H and Kim C (1964). Interactions of 31 MeV protons with He4, *Nuclear Physics* **53**(0), 241 – 251.
URL: *http://www.sciencedirect.com/science/article/pii/0029558264906029*

Burbidge E M, Burbidge G R, Fowler W A and Hoyle F (1957). Synthesis of the Elements in Stars, *Rev. Mod. Phys.* **29**, 547–650.

URL: *http://link.aps.org/doi/10.1103/RevModPhys.29.547*

Calarco J R, Hanna S S, Chang C C, Diener E M, Kuhlmann E and Fisher G A (1983). Absolute cross section for the reaction ^{3}H(p, γ_0)^{4}He and a review of ^{4}He(γ, p$_0$)^{3}H measurements, Phys. Rev. C **28**, 483–488.

Canon R S, Nelson S O, Sabourov K, Wulf E, Weller H R, Prior R M, Spraker M, Kelley J H and Tilley D R (2002). ^{3}H($\vec{p}$,γ)^{4}He reaction below E$_p$=80 keV, Phys. Rev. C **65**(4), 044008.

Carlson R F, Cox A J, Nimmo J R, Davison N E, Elbakr S A, Horton J L, Houdayer A, Sourkes A M, van Oers W T H and Margaziotis D J (1975). Proton total reaction cross sections for the doubly magic nuclei ^{16}O, ^{40}Ca, and ^{208}Pb in the energy range 20-50 MeV, Phys. Rev. C **12**, 1167–1175.

Colgate S A (1975). Shock-wave thermalization, ApJ **195**, 493–498.

Cyburt R H, Amthor A M, Ferguson R, Meisel Z, Smith K, Warren S, Heger A, Hoffman R D, Rauscher T, Sakharuk A, Schatz H, Thielemann F K and Wiescher M (2010). The JINA REACLIB Database: Its Recent Updates and Impact on Type-I X-ray Bursts, *The Astrophysical Journal Supplement Series* **189**(1), 240.
URL: *http://stacks.iop.org/0067-0049/189/i=1/a=240*

Dahlbacka G H, Chapline G F and Weaver T A (1974). Gamma rays from black holes, Nature **250**, 36–37.

Dermer C D (1986). Secondary production of neutral pi-mesons and the diffuse galactic gamma radiation, A&A **157**, 223–229.

Edgington J A and Rose B (1966). Nuclear Bremsstrahlung from p-p and p-d interactions near 140 MeV, *Physics Letters* **20**, 552–553.

Evaluated Nuclear Data File (ENDF) (n.d.).
URL: *http://www.nndc.bnl.gov/exfor/endf00.jsp*

Expermimental Nuclear Reaction Data (EXFOR/CSISRS) (n.d.).
URL: *http://www.nndc.bnl.gov/exfor/exfor00.htm*

Fields B D (2011). The Primordial Lithium Problem, *Annual Review of Nuclear and Particle Science* **61**, 47–68.

Fowler W A, Caughlan G R and Zimmerman B A (1967). Thermonuclear Reaction Rates, ARA&A **5**, 525.

Gell-Mann M and Watson K M (1954). The Interactions Between pi-Mesons and Nucleons, *Annual Review of Nuclear and Particle Science* **4**, 219–270.

Giovannelli F, Karakula S and Tkaczyk W (1982). High energy gamma-rays from black holes, Acta Astron. **32**, 121–130.

Glagola B G, Viola, Jr. V E, Breuer H, Chant N S, Nadasen A, Roos P G, Austin S M and Mathews G J (1982). Production of ^{6}He, ^{6}Li, ^{7}Li, and ^{7}Be in the alpha +α reaction between 60-160 MeV, Phys. Rev. C **25**, 34–45.

Gould R J (1980). Thermal bremsstrahlung from high-temperature plasmas, ApJ **238**, 1026–1033.

Gould R J (1986). Breakup of helium nuclei in high-temperature plasmas, *Nuclear Physics B* **266**, 737–747.

Guessoum N and Jean P (2002). Detectability and characteristics of the 2.223 MeV line emission from nearby X-ray binaries, A&A **396**, 157–169.

Guessoum N and Kazanas D (1990). Neutron viscosity in accretion disks, ApJ **358**, 525–537.

Guessoum N, Kazanas D and Ramaty R (1999). Production of Li, Be, B in the Companions of X-Ray Novae, *Astrophysical Letters and Communications* **38**, 415.

Harris M J and Share G H (1991). A search for the 2.223 MeV neutron capture gamma-ray line from the directions of Cygnus and the Galactic center, ApJ **381**, 439–443.

Higdon J C and Lingenfelter R E (1977). Nuclear gamma-ray lines in accretion source spectra, ApJ **215**, L53–L55.

Hix W R and Thielemann F K (1999). Computational methods for nucleosynthesis and nuclear energy generation., *Journal of Computational and Applied Mathematics* **109**, 321–351.

Iocco F and Pato M (2012). Lithium Synthesis in Microquasar Accretion, *Phys. Rev. Lett.* **109**, 021102.
URL: *http://link.aps.org/doi/10.1103/PhysRevLett.109.021102*

Jean P and Guessoum N (2001). Neutron-capture and 2.22 MeV emission in the atmosphere of the secondary of an X-ray binary, A&A **378**, 509–521.

JENDL High Energy File 2007 (JENDL/HE-2007) (n.d.).
URL: *http://wwwndc.jaea.go.jp/ftpnd/jendl/jendl-he-2007.html*

Jin L (1990). Can black hole accretion produce Li-7?, ApJ **356**, 501–506.

Jorissen A and Goriely S (2001). The Nuclear Network Generator: A tool for nuclear astrophysics, *Nuclear Physics A* **688**, 508–510.

Kamae T, Karlsson N, Mizuno T, Abe T and Koi T (2006). Parameterization of γ, $e^{+/-}$, and Neutrino Spectra Produced by p-p Interaction in Astronomical Environments, ApJ **647**, 692–708.

Kelner S R, Aharonian F A and Bugayov V V (2006). Energy spectra of gamma rays, electrons, and neutrinos produced at proton-proton interactions in the very high energy regime, Phys. Rev. D **74**(3), 034018.

King C H, Austin S M, Rossner H H and Chien W S (1977). ^{7}Li and ^{7}Be production in the alpha + α reaction, Phys. Rev. C **16**, 1712–1722.

Kolykhalov P I and Syunyaev R A (1979). Gamma emission during spherically symmetric accretion onto black holes in binary stellar systems, Soviet Ast. **23**, 189.

Machner H and Haidenbauer J (1999). Meson production close to threshold, *Journal of Physics G: Nuclear and Particle Physics* **25**(10), R231.
URL: *http://stacks.iop.org/0954-3899/25/i=10/a=201*

Mahadevan R, Narayan R and Krolik J (1997). Gamma-Ray Emission from Advection-dominated Accretion Flows around Black Holes: Application to the Galactic Center, ApJ **486**, 268.

MathWorks Inc. (Matlab R2009b) (n.d.).
URL: *http://www.mathworks.com/help/matlab*

Mercer D J, Austin S M, Brown J A, Danczyk S A, Hirzebruch S E, Kelley J H, Suomijärvi T, Roberts D A and Walker T P (2001). Production of A=6,7 nuclides in the α+α reaction and cosmic ray nucleosynthesis, Phys. Rev. C **63**(6), 065805.

Meyer H, Horowitz C, Nann H, Pancella P, Pate S, Pollock R, Przewoski B V, Rinckel T, Ross M and Sperisen F (1992). Total cross section for $p + p \rightarrow p + p + \pi^0$ close to threshold, *Nuclear Physics A* **539**(4), 633 – 661.
URL: *http://www.sciencedirect.com/science/article/pii/037594749290130C*

Meyer H O, Ross M A, Pollock R E, Berdoz A, Dohrmann F, Goodwin J E, Minty M G, Nann H, Pancella P V, Pate S F, Przewoski B v, Rinckel T and Sperisen F (1990). Total cross section for $p + p \rightarrow p + p + \pi^0$ near threshold measured with the Indiana Cooler, *Phys. Rev. Lett.* **65**, 2846–2849.
URL: *http://link.aps.org/doi/10.1103/PhysRevLett.65.2846*

Narayan R and Popham R (1993). Hard X-rays from accretion disk boundary layers, Nature **362**, 820–822.

Narayan R and Yi I (1995*a*). Advection dominated accretion: Underfed black holes and neutron stars, *Astrophys.J.* **452**, 710.

Narayan R and Yi I s (1994). Advection dominated accretion: A Selfsimilar solution, *Astrophys.J.* **428**, L13.

Narayan R and Yi I s (1995*b*). Advection dominated accretion: Selfsimilarity and bipolar outflows, *Astrophys.J.* **444**, 231.

Nifenecker H and Pinston J A (1989). High energy gamma-ray production in nuclear reactions, *Progress in Particle and Nuclear Physics* **23**, 271–355.

Njock M K, Maurel M, Monnand E, Nifenecker H, Perrin P, Pinston J A, Schussler F and Shutz Y (1988). Impact parameter dependence of high-energy gamma-ray production in argon induced reaction at 85 MeV/nucleon, *Nuclear Physics A* **489**, 368–380.

Oka K and Manmoto T (2003). Gamma-ray emission from an accretion flow around a Kerr black hole, MNRAS **340**, 543–550.

Paczynski B and Bisnovatyi-Kogan G (1981). A Model of a Thin Accretion Disk around a Black Hole, Acta Astron. **31**, 283.

Primas F (2010). Beryllium and boron in metal-poor stars, *in IAU Symposium*, C Charbonnel, M Tosi, F Primas and C Chiappini, eds, Vol. 268 of *IAU Symposium*, pp. 221–230.

Ramadurai S and Rees M J (1985). Deuterium Abundance and Population-III Remnants, MNRAS **215**, 53P.

Rauscher T (2006), 'Nuclear Astrophysics Results (NucAstro)', Online source.
URL: *http://nucastro.org/Welcome.html*

Rauscher T (2011). The Path to Improved Reaction Rates for Astrophysics, *International Journal of Modern Physics E* **20**, 1071–1169.

Rauscher T and Thielemann F K (2000). Astrophysical Reaction Rates From Statistical Model Calculations, *Atomic Data and Nuclear Data Tables* **75**, 1–351.

Remington B A, Blann M and Bertsch G F (1987). n-p bremsstrahlung interpretation of high energy gamma rays from heavy-ion collisions, Phys. Rev. C **35**, 1720–1729.

Rosenfeld A H (1954). Production of Pions in Nucleon-Nucleon Collisions at Cyclotron Energies, *Physical Review* **96**, 139–149.

Sagle A L, Bonner B E, Brady F P, King N S P, McNaughton M W, Romero J L and Ullmann J L (1991). ^{3}H+d⇌n+^{4}He measurements and absolute neutron-polarization determination at 50 MeV, *Nuclear Physics A* **530**, 387–400.

Sagle A L, Bonner B E, Brady F P, King N S P and Romero J L (1991). ^{4}He(p,d)^{3}He analyzing powers and differential cross sections at 32, 40, 50 and 52.5 MeV, *Nuclear Physics A* **530**, 370–386.

Shamu R E and Jenkin J G (1964). Neutron-Alpha Scattering in the 20-MeV Range, *Physical Review* **135**, 99–109.

Shapiro S, Lightman A and Eardley D (1976). A two - temperature accretion disk model for Cygnus X-1. 1. Structure and spectrum, *Astrophys.J.* **204**, 187–199.

Shimizu F, Koiso H, Kubota Y, Sai F, Sakamoto S and Yamamoto S (1982). Study of pp interactions in the momentum range 0.9 to 2.0 GeV/c, *Nuclear Physics A* **389**(3), 445 – 456.
URL: *http://www.sciencedirect.com/science/article/pii/0375947482904249*

Spiger R J and Tombrello T A (1967). Scattering of He^{3} by He^{4} and of He^{4} by Tritium, *Physical Review* **163**, 964–984.

Stanislaus S, Horváth D, Measday D F, Noble A J and Salomon M (1991). Total cross sections and analyzing powers for the reaction $p + p \rightarrow p + p + \pi^0$ near threshold, *Phys. Rev. C* **44**, 2287–2302.
URL: *http://link.aps.org/doi/10.1103/PhysRevC.44.2287*

Stecker F W (1970). The Cosmic γ-Ray Spectrum from Secondary Particle Production in Cosmic-Ray Interactions, Ap&SS **6**, 377–389.

Suess H E and Urey H C (1956). Abundances of the Elements, *Reviews of Modern Physics* **28**, 53–74.

Svensson R (1984). Steady mildly relativistic thermal plasmas - Processes and properties, MNRAS **209**, 175–208.

The Joint Evaluated Fission and Fusion File (JEFF) OECD/NEA Data Bank (n.d.).

URL: *http://www.oecd-nea.org/dbdata/jeff/*

Thielemann F K, Truran J W and Arnould M (1986). Thermonuclear reaction rates from statistical model calculations, *in Advances in Nuclear Astrophysics*, E Vangioni-Flam, J Audouze, M Casse, J P Chieze and J Tran Thanh Van, eds, pp. 525–540.

Tserruya I, Eisen Y, Pelte D, Gavron A, Oeschler H, Berndt D and Harney H L (1978). Total fusion cross section for the ^{16}O+^{16}O system, Phys. Rev. C **18**, 1688–1699.

Vestrand W T (1990). A new gamma-ray diagnostic for energetic ion distributions - The Compton tail on the neutron capture line, ApJ **352**, 353–360.

Votta L G, Roos P G, Chant N S and Woody R (1974). Elastic proton scattering from ^{3}He and ^{4}He and the ^{4}He$(p,d)^3$He reaction at 85 MeV, *Phys. Rev. C* **10**, 520–528.

URL: *http://link.aps.org/doi/10.1103/PhysRevC.10.520*

Weaver T A (1976). Reaction rates in a relativistic plasma, *Phys. Rev. A* **13**, 1563–1569.

URL: *http://link.aps.org/doi/10.1103/PhysRevA.13.1563*

Woosley S, Fowler W A, Holmes J and Zimmerman B (1978). Semiempirical thermonuclear reaction-rate data for intermediate-mass nuclei, *Atomic Data and Nuclear Data Tables* **22**(5), 371 – 441.

URL: *http://www.sciencedirect.com/science/article/pii/0092640X78900189*

Xu Y, Goriely S, Jorissen A, Chen G L and Arnould M (2013). Databases and tools for nuclear astrophysics applications. BRUSsels Nuclear LIBrary (BRUSLIB), Nuclear Astrophysics Compilation of REactions II (NACRE II) and Nuclear NETwork GENerator (NETGEN), A&A **549**, A106.

Yi I and Narayan R (1997). Lithium Production in Hot Advection-dominated Accretion Flows in Soft X-Ray Transients, ApJ **486**, 363.

A

Quantitative justification of discarded nucleus–nucleus reactions

As discussed in section 2.2.1, the most important nuclear reactions between nuclei are those that involve n, p or α-particles. Here we will quantify the error that the discarded reactions cause in the nuclear network solution. The matters will be justified for a solar composition plasma; afterwards, limits will be set on the abundances of e.g. heavy elements, such that the nuclear network solution will have an accepted accuracy.

We can quantify the error magnitude that the discarded reactions generate on the network solution by comparing their reaction rates (or the reaction time-scales) with their respective dominant channels. Let we consider the two most abundant elements after p and α-particles – D and ^{16}O. Deuterium is the third most abundant element after p and α-particles among the group of elements lighter than ^{4}He. It is not abundant initially; however, different nuclear reactions such as spallation of heavy nuclei or weak nucleosynthesis. Proton-proton inelastic collisions in very high temperatures are also able to produce D. All these reactions cannot increase the number density ratio of deuterium with respect to protons (n_D/n_p) more than 10^{-3}. On the other hand, ^{16}O is the most abundant among the elements heavier than ^{4}He. Its initial number density ratio with respect to protons is $n_{O16}/n_p \approx 5.4 \times 10^{-4}$ (Suess and Urey, 1956; Anders and Grevesse, 1989).

Let us symbolize with ξ either D or ^{16}O. More specifically, we want to compare the reaction rates of $D + D$ and $^{16}\mathrm{O} + {}^{16}\mathrm{O}$ (i.e. $\xi + \xi$) with their respective destruction channels from p and α (i.e. $p + \xi$ and $\alpha + \xi$). Note that D becomes abundant when all nuclei are destroyed; thus it is not necessary to compare the $D + D$ with $\alpha + D$ reaction rate simply because α-particles exist in very small quantities during that period.

The reaction rate is defined by $\Gamma = \langle \sigma \upsilon \rangle \times n$, where the $\langle \sigma \upsilon \rangle$ is the Maxwellian average rate, and n is the projectile number density. The destruction reaction

rates ratios are:

$$\frac{\Gamma_{(\xi+\xi)}}{\Gamma_{(p+\xi)}} = \frac{\left\langle \sigma_{(\xi+\xi)}\, \upsilon \right\rangle}{\left\langle \sigma_{(p+\xi)}\, \upsilon \right\rangle} \times \frac{n_\xi}{n_p} \tag{A.1}$$

$$\frac{\Gamma_{(\xi+\xi)}}{\Gamma_{(\alpha+\xi)}} = \frac{\left\langle \sigma_{(\xi+\xi)}\, \upsilon \right\rangle}{\left\langle \sigma_{(\alpha+\xi)}\, \upsilon \right\rangle} \times \frac{n_\xi}{n_\alpha} \tag{A.2}$$

For an order of magnitude estimation of the ratio between the reaction rates we can estimate the rate $\langle \sigma\upsilon \rangle$ by simply considering a constant cross-section σ. where, the rate becomes $\sigma\ \langle \upsilon \rangle = \sigma\, \bar{\upsilon}$, where $\bar{\upsilon} = \langle \upsilon \rangle$ is the average thermal collision velocity which is $\bar{\upsilon} \sim \mu^{-1/2}$, if μ is the reduced mass for the projectile-target system. A rough estimate of the cross-sections ratios, can be done by simply comparing their maximum values for a projectile energy $E > 1$ MeV. This makes sense because at these energies the cross-sections have roughly the same energy dependence.

The $p + D$ reaction has a threshold around 3 MeV. To gain a large amount of D in the plasma, requires to destroy all heavy nuclei; therefore, the plasma must have a high temperature i.e. at least $k_B T > 5$ MeV. For this reason the reaction threshold will not play a significant role. The $p+D$ and $D+D$ reaction cross-sections show the same behaviour for a projectile energy $E > 6$ MeV, and the ratio between the cross-sections highest values is $\sigma_{(D+D)}/\sigma_{(p+D)} \lesssim 0.5$.

The total nonelastic cross-sections for $p + {}^{16}\mathrm{O}$, $\alpha + {}^{16}\mathrm{O}$ and ${}^{16}\mathrm{O} + {}^{16}\mathrm{O}$ have almost the same behaviour. Thus from measurements in (Carlson et al., 1975; Auce et al., 1994; Tserruya et al., 1978), we get the following ratios: $\sigma_{(O16+O16)}/\sigma_{(p+O16)} \sim 2$ and $\sigma_{(\alpha+O16)}/\sigma_{(p+O16)} \sim 2$.

By taking the number density ratios to be $n_D/n_p < 10^{-3}$; $n_{He4}/n_p \approx 8 \times 10^{-2}$ and $n_{O16}/n_p \approx 5.4 \times 10^{-4}$, the reaction rate ratios become:

$$\frac{\Gamma_{(D+D)}}{\Gamma_{(p+D)}} \approx \frac{\sigma_{(D+D)}}{\sigma_{(p+D)}} \sqrt{\frac{\mu_{(p,D)}}{\mu_{(D+D)}}} \frac{n_D}{n_p} \sim 4 \times 10^{-4} \tag{A.3}$$

$$\frac{\Gamma_{(\alpha+O16)}}{\Gamma_{(p+O16)}} \approx \frac{\sigma_{(\alpha+O16)}}{\sigma_{(p+O16)}} \sqrt{\frac{\mu_{(p,O16)}}{\mu_{(\alpha,O16)}}} \frac{n_\alpha}{n_p} \sim 9 \times 10^{-2} \tag{A.4}$$

$$\frac{\Gamma_{(O16+O16)}}{\Gamma_{(p+O16)}} \approx \frac{\sigma_{(O16+O16)}}{\sigma_{(p+O16)}} \sqrt{\frac{\mu_{(p,O16)}}{\mu_{(O16,O16)}}} \frac{n_{O16}}{n_p} \sim 4 \times 10^{-4} \tag{A.5}$$

As mentioned, D and ${}^{16}\mathrm{O}$ represent the elements lighter and heavier than ${}^{4}\mathrm{He}$, respectively. They are the most abundant in their respective categories. Therefore, neglecting a reaction with projectile different from p and α particles will cause an error

$$\frac{\Gamma_{(D+D)}}{\Gamma_{(p+D)} + \Gamma_{(D+D)}} \lesssim 0.04\%; \quad \frac{\Gamma_{(O16+O16)}}{\Gamma_{(p+O16)} + \Gamma_{(\alpha+O16)} + \Gamma_{(O16+O16)}} < 0.04\%$$

Thus, for a solar composition we can neglect all reactions except the one that p and α are involved with a solution accuracy better than 0.4%. Some very hot accretion flow systems can accrete matter from Wolf-Rayet stars or from white dwarfs. These stars have much higher metallicities compared to a solar one. Thus it is important to know if heavy nuclei interactions are important in such systems. By using the above estimates, a plasma with $n_{\mathcal{A}}/n_p \lesssim 10^{-1}$ – if $\mathcal{A}$ is an element heavier than ^{4}He – we can still neglect heavy nuclei interactions but the solution accuracy will drop to 7 %.

B Photodisintegration

As discussed in section 2.2.1, the most important projectiles are protons, neutrons and alpha particles. Plasmas produce photons through ion-nuclear reactions and electron bremsstrahlung. The photon number density depends on the optical depth, i.e. electron density and the plasma's size. The photon number density per E_γ energy interval (dn_γ/dE_γ), is given by:

$$\frac{dn_\gamma}{dE_\gamma} \approx \frac{d\dot{n}_\gamma}{dE_\gamma} \times \frac{R}{c} \times \max(1,\tau) \quad , \tag{B.1}$$

where $d\dot{n}_\gamma/dE_\gamma$ is the photon production rate per E_γ energy interval, R is the size of the plasma, τ is the optical depth and c is the speed of light. The term $\max(1,\tau)$ takes into account the photon's time-escape delay due to propagation through an optically thick plasma ($\tau > 1$).

The optical depth for a homogeneous plasma with number density n and size R is given simply by $\tau(E_\gamma) = n\,R\,\sigma_c(E_\gamma)$, where $\sigma_c(E_\gamma)$ is the Compton scattering cross-section.

The photodisintegration reaction-rate is given by:

$$\Gamma_{(\gamma,\mathcal{A})} = \int dE_\gamma \frac{dn_\gamma}{dE_\gamma} \sigma_{(\gamma,\mathcal{A})}(E_\gamma)\, c \tag{B.2}$$

where $\sigma_{(\gamma,\mathcal{A})}(E_\gamma)$ is the photodisintegration cross-section for a given nucleus $\mathcal{A}$. The cross sections for the important nuclei such as D, ^{12}C, ^{16}O, ^{56}Fe, etc, generally show a threshold $E_\gamma > 2$ MeV, and have a maximum around $7 - 20$ MeV.

By including all of the above, one obtains:

$$\Gamma_{(\gamma,\mathcal{A})} = R \int dE_\gamma \left(\frac{d\dot{n}_\gamma(E_\gamma)}{dE_\gamma} \right) \times \sigma_{(\gamma,\mathcal{A})}(E_\gamma) \times \max\left(1, \tau(E_\gamma)\right) \tag{B.3}$$

Note that the photodisintegration reaction rate in eq. (B.3), includes two cases, one without optical depth and one with optical depth. The case without optical depth scales as $n_e^2 R$ (n_e is the electron number density), whilst the case with optical depth scales as $n_e^3 R^2$. On the other hand ion-nuclear reaction rates scale as n_i^2 (n_i is the ion number density). Thus, for an optically thin plasma, photodisintegration effect is mostly influenced by the size R because $n_e \sim n_i$.

In a high temperature, low density and optically thin plasma, electrons could not be heated to high temperatures. The reasons is that electrons which are heated due to Coulomb exchange with ions are cooled quickly through Bremsstrahlung and other possible cooling processes such as Synchrotron and/or Comptonization. In the extreme case of electrons getting heated to high temperatures ($k_B T_e > 1$ MeV), pair-production processes become effective, and thus, will cool the plasma down (see e.g. Bisnovatyi-Kogan et al., 1971; Svensson, 1984).

We consider here an uniform, electrically neutral, spherically symmetric, optically thin plasma, with a size $R \sim 10^6$ cm and number density $n \sim 10^{18}$ cm^{-3}. Let we also consider two important nuclei, the ^{16}O as the third most abundant cosmic/solar element after Hydrogen and Helium, and Deuterium as the most abundant light element obtained after heavier nuclei are destroyed. Let we first calculate the photodisintegration reaction rate due to electron thermal bremsstrahlung (Gould, 1980) and p–n capture and thermal nuclear bremsstrahlung as it is calculated in section 2.3. Let we calculate the photodisintegration reaction rate for $^{16}\mathrm{O}(\gamma, X)$ and $\mathrm{D}(\gamma, n)p$ reactions and then compare them with e.g. $^{16}\mathrm{O}(p, X)$ proton spallation reaction. The results are shown in fig. B.1. Note that reaction rates calculated with thermal electron bremsstrahlung photons are a function of electron temperature, whereas the reaction rates calculated from p–n interactions are a function of ion temperature. Figure B.1 reveals that for a spherically symmetric, optically thin plasma with size $R = 10^6$ cm, and number density $n = 10^{18}$ cm^{-3}, the photodisintegration due to thermal electron bremsstrahlung and p–n thermal capture and nuclear bremsstrahlung is negligible. Even when the electron temperature becomes comparable with the ion temperature, the photodisintegration reaction rate is 3-4 orders of magnitude below other nuclear reaction rates, which is clearly seen by comparing $^{16}\mathrm{O}(\gamma, X)$ and $^{16}\mathrm{O}(p, X)$. In the case when the electron temperature is lower than the ion temperature, and there is a significant amount of neutrons in the plasma (here we took,

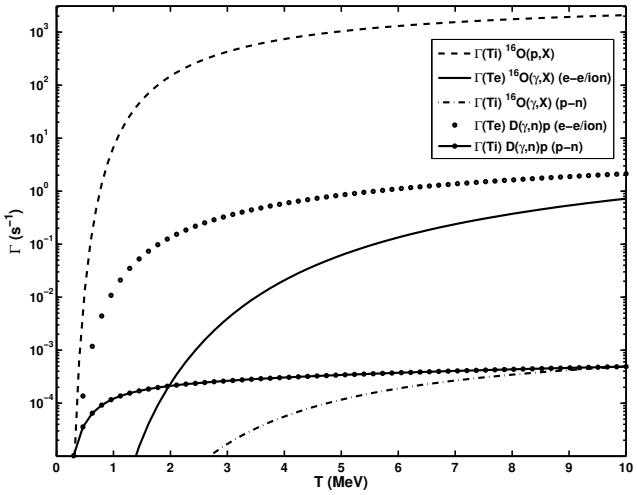

Figure B.1: The photodisintegration of ^{16}O and D nuclei due to thermal electron bremsstrahlung and p–n capture and nuclear bremsstrahlung as a function of temperature, for a plasma with size $R = 10^6$ cm, and $n = 10^{18}$ cm^{-3}. The full line (^{16}O) and the dotted curve (D) are the photodisintegration reaction rates calculated with thermal electron bremsstrahlung photons. They are a function of electron temperature (T_e). The dash-dotted (^{16}O) and the full-dotted (D) lines are the photodisintegration reaction rates calculated with p–n thermal capture and nuclear bremsstrahlung. They are a function of ion temperature (T_i). For comparison the dashed curve is the proton destruction reaction rate of ^{16}O as a function of ion temperature (T_i).

for simplicity, $n_n = n_p = 10^{18}$ cm^{-3}), the most significant amount of γ-rays are produced from $p-n$ interactions. We see from fig. B.1 that the contribution of photodisintegration due to γ-rays coming from $p-n$ interactions is negligible, too. If the electron temperature is $T_e < 1$ MeV then photodisintegration due to photons emitted by electrons and from $p-n$ interactions could affect the nuclear statistical equilibrium only for time-scales longer than $\Gamma^{-1} > 10^4$ s.

Nuclear reactions in plasma produce γ-ray lines. Very high temperature plasma will have an additional γ-ray channel due to $p + p \rightarrow \pi^0$ production. Let we estimate the highest photodisintegration reaction rate from this γ-ray sources.

The prompt nuclear γ-ray lines are formed in a reaction like $p + \mathcal{A} \rightarrow \gamma$. Let $\sigma_{(p\mathcal{A}\gamma)}$ be the γ-ray line production cross-section and n_p and $n_{\mathcal{A}}$ be the number densities of projectile and target nucleus. The photo-production rate per unit volume is given by $\dot{n}_\gamma = \left\langle \sigma_{(p\mathcal{A}\gamma)}\, \upsilon \right\rangle n_p\, n_{\mathcal{A}}$. Consider that the cross-section is constant with its maximum possible value; thus the reaction rate will become $\dot{n}_\gamma = \sigma_{(p\mathcal{A}\gamma)}\, \bar{\upsilon}\, n_p\, n_{\mathcal{A}}$, where $\bar{\upsilon}$ denotes the average thermal collision velocity.

On the other hand, the π^0 production rate per unit volume is given by $\dot{n}_{\pi^0} = \sigma_{\pi^0}\,\bar{\upsilon}\,n_p^2/2$, if σ_{π^0} is the peak value of the $p + p \rightarrow p + p + \pi^0$ reaction. For each π^0 there will be two γ-rays, therefore $\dot{n}_\gamma = \sigma_{\pi^0}\,\bar{\upsilon}\,n_p^2$.

By plugging these photon production rates into eq. (B.1) and then substituting the photon number densities into the eq. (B.2), one obtains:

$$\Gamma_{1(\gamma\mathcal{A})} \sim R\,n_p\,n_{\mathcal{A}}\,\bar{\upsilon} \times \sigma_{1(\gamma\mathcal{A})} \times \sigma_{(p\mathcal{A}\gamma)} \tag{B.4}$$

$$\Gamma_{2(\gamma\mathcal{A})} \sim R\,n_p\;n_p\,\bar{\upsilon}\;\times \sigma_{2(\gamma\mathcal{A})} \times \sigma_{\pi^0} \tag{B.5}$$

The $\sigma_{1(\gamma\mathcal{A})}$ is the maximum photodisintegration cross-section value for the interval $0.1 < E_\gamma < 10$ MeV where nuclear lines are emitted; whereas, the $\sigma_{2(\gamma\mathcal{A})}$ is the maximum photodisintegration cross-section value for the interval $10 < E_\gamma < 400$ MeV where π^0 photons are emitted.

The total non-elastic reaction rate for the element $\mathcal{A}$ through e.g. $p + \mathcal{A}$ is given by $\Gamma_{(p\mathcal{A})} \sim \sigma_{(p\mathcal{A})}\,\bar{\upsilon}\,n_p$. Therefore the ratio between the photodisintegration and total non-elastic reaction rates, is:

$$\frac{\Gamma_{(\gamma\mathcal{A})}}{\Gamma_{(p\mathcal{A})}} \sim R\,n_p \times \left(\frac{\sigma_{1(\gamma\mathcal{A})}\;\sigma_{(p\mathcal{A}\gamma)}}{\sigma_{(p\mathcal{A})}}\,\frac{n_{\mathcal{A}}}{n_p} + \frac{\sigma_{2(\gamma\mathcal{A})}\;\sigma_{\pi^0}}{\sigma_{(p\mathcal{A})}}\right) \tag{B.6}$$

The typical ratios between the cross-sections peak values are: $\sigma_{(p\mathcal{A}\gamma)}/\sigma_{(p\mathcal{A})} \sim 10^{-1}$, $\sigma_{\pi^0}/\sigma_{(p\mathcal{A})} \lesssim 10^{-3}$, because the π^0 production has a threshold at around 280 MeV the ratio in the most important interval is much lower. For solar composition the ratio is $n_{\mathcal{A}}/n_p \sim 10^{-4}$, while for high metallicity composition is $n_{\mathcal{A}}/n_p \sim 10^{-1}$. The photodisintegration cross-section is taken to be $\sigma_{1(\gamma\mathcal{N})} \sim \sigma_{2(\gamma\mathcal{N})} \sim 0.1$ b. By substituting one obtains:

$$\frac{\Gamma_{(\gamma\mathcal{N})}}{\Gamma_{(p\mathcal{N})}} < \mathcal{K} \times \left(\frac{R}{10^8\ \mathrm{cm}}\right) \times \left(\frac{n_p}{10^{17}\ \mathrm{cm}^{-3}}\right), \tag{B.7}$$

with $\mathcal{K} \sim 10^{-4}$ in case of a solar composition and $\mathcal{K} \sim 10^{-2}$ in case of a high metallicity plasma.

We conclude here that the photodisintegration reactions are negligible. They are about three orders of magnitude less than the other nuclear reac-

tions even if we consider the highest values of all parameters.

C The boundaries of the reaction rate integral

The integral in eq. (2.1) is evaluated over the energy range $(0, \infty)$. In practice, however, one needs to integrate eq. (2.1) only in a "narrow" energy interval where the most important contribution to the reaction rate come from. An accurate evaluation of the reaction rate requires to know precisely the cross-section in that narrow energy interval.

For a given temperature, there exists an energy interval $[\epsilon_1(T), \epsilon_2(T)] \in [0, \infty)$, such that, the integration over it brings the major contribution to the rate ($\langle \sigma \upsilon \rangle$). In other words we can split the integral in eq. (2.1) as:

$$\int_0^\infty = \int_0^{\epsilon_1(T)} + \left[\int_{\epsilon_1(T)}^{\epsilon_2(T)} \right] + \int_{\epsilon_2(T)}^\infty \tag{C.1}$$

$$\frac{\int_0^{\epsilon_1(T)} + \int_{\epsilon_2(T)}^\infty}{\int_0^\infty} \equiv \varepsilon \ll 1 \tag{C.2}$$

Working within the temperature range $[T_1, T_2]$, we want to obtain the maximal integration interval $[E_1, E_2]$ such that the accuracy of the rate is greater than a desired value (ε). The energy interval $[E_1, E_2]$ includes all energy windows $[\epsilon_1(T), \epsilon_2(T)]$ for any temperatures in $[T_1, T_2]$. Therefore, it is expected that the lowest temperature T_1 will affect the lowest energy limit E_1, and the highest temperature T_2 that of the energy limit E_2. The reason of course, is the Maxwellian distribution function which constrains the two limits.

Although the Maxwellian distribution is the main factor that constraints the integration limits, it may not work always alone. The reaction cross-sections, however, play a role, too; especially the cross-section behaviour at low and high energies. For instance, the low energy cross-section might be zero due to the reaction threshold. For this case the lowest integration limit

does not need to be lower than the threshold energy. However, there could be a complete opposite behaviour for which the cross-section is very large at low energies. A typical example is the neutron capture cross-section such as the neutron capture by hydrogen $n + p \rightarrow D + \gamma$ for which the cross-section at low energies behave like $\sigma \sim 1/\upsilon \sim E^{-1/2}$.

On the other hand, the high energy cross-section – if there are no resonances – will behave similarly to the geometrical cross-section. It will fall as $\sigma \sim E^{-1}$ until it becomes approximately constant at very high energies.

To sum all up, the lowest integration limit E_1 is affected by the lowest temperature T_1 and the low energy cross-section – especially the neutron capture ($\sigma \sim E^{-1}$). On the other hand, the highest integration limit E_2 is affected by the highest temperature T_2 and the high energy cross-section.

By combing this with the integration of eq. (2.1) and the notation in eq. (C.1) we obtain:

$$\int_{E_1}^{\infty} dE\, \sigma_1\, E\, \exp\left(-\frac{E}{k_B T_1}\right) = (1-\varepsilon) \int_{0}^{\infty} dE\, \sigma_1\, E\, \exp\left(-\frac{E}{k_B T_1}\right) \tag{C.3}$$

$$\int_{0}^{E_2} dE\, \sigma_2\, E\, \exp\left(-\frac{E}{k_B T_2}\right) = (1-\varepsilon) \int_{0}^{\infty} dE\, \sigma_2\, E\, \exp\left(-\frac{E}{k_B T_2}\right) \tag{C.4}$$

Here I have simplified the calculations by considering that $E_1 \ll E_2$. This allows that when we calculate E_1 we can consider E_2 as very big "∞". Recall that $[E_2, \infty)$ integration is by definition very small. The same happen when we calculate the E_2 for which E_1 is considered as "0". Recall that the $[0, E_1]$ is by definition very small.

By taking the extremes, $\sigma_1 \sim E^{-1/2}$ and $\sigma_2 =$ constant and then by integrating eq. (C.3) and eq. (C.4), we obtain:

$$\operatorname{erf}\left(\sqrt{\frac{E_1}{k_B T_1}}\right) - \sqrt{\frac{E_1}{\pi\, k_B T_1}} \times \exp\left(-\frac{E_1}{k_B T_1}\right) \equiv \varepsilon \tag{C.5}$$

$$\left(1 + \frac{E_2}{k_B T_2}\right) \times \exp\left(-\frac{E_2}{k_B T_2}\right) \equiv (1-\varepsilon) \tag{C.6}$$

For $\varepsilon = 1$ % the solutions are $E_1 \approx 3 \times 10^{-4} \times k_B T_1$ and $E_2 \approx 6.6 \times k_B T_2$. For $\varepsilon = 5$ % the $E_1 \approx 8 \times 10^{-3} \times k_B T_1$ and the $E_2 \approx 4.7 \times k_B T_2$. Whereas for $\varepsilon = 10$ % the solutions are $E_1 \approx 0.03 \times k_B T_1$ and $E_2 \approx 3.9 \times k_B T_2$.

Thus in the worst case $\varepsilon = 10$ % accuracy, the limits of energy for a temperature that varies between $T \in (1,\ 100)$ MeV are in $E \in (0.01,\ 400)$ MeV.

Note, however, that the boundaries $[E_1, E_2]$ were taken to be all inclusive; therefore, they form the largest energy interval we need to know about all critical cross-sections, i.e. the cross-sections that become large at low or

high energies. Most of the cross sections have a threshold value which is $E > 1$ MeV; making the calculations of even lower temperatures much more accurate. At high energies however, we do not know with accuracy the behaviour of all channels. For most of the channels we do not have data at all which makes the high temperature calculations very difficult. In section 2.2.2 I will impose a general assumption that the cross-section behaviour for energies higher than $E > 250$ MeV is $\sigma \sim E^{-1}$. This will allow us to calculate higher temperature rates.

Note once more that ε is the error that the rate $\langle \sigma \upsilon \rangle$ has at the temperature boundaries T_1 and T_2; for the intermediate temperatures the accuracy is much higher.

D The capture reaction γ-ray spectra

Different from nuclear de-excitation γ-ray lines that are result of nuclear transition between two levels with definite energy, the γ-rays that are produced through capture reaction such as $1 + 2 \rightarrow 3 + \gamma$ have a kinematic photon. This means that γ-ray energy depends on the energy of the two interacting particles 1 and 2.

Let we define the γ-ray energy emitted per unit volume and time by the capture reaction at photon energy E_γ, to be:

$$d\,\epsilon_\gamma(E_\gamma) = E_\gamma * d\,\dot{n}_\gamma(E_\gamma) = E_\gamma \frac{d\,\dot{n}_\gamma(E_\gamma)}{d\,E_\gamma} d\,E_\gamma \tag{D.1}$$

where the $\dot{n}_\gamma$ is the number of photons emitted at the energy E_γ per unit volume and time.

The production rate of photons ($\dot{n}_\gamma$) is a function of the reaction $1 + 2 \rightarrow 3 + \gamma$ rate. If particles 1 and 2 have two distributions f_1 and f_2 which we assume to be Maxwellian distributions then we obtain:

$$d\,\dot{n}_\gamma = n_1\, n_2\, d\,(< \sigma\, v >) \tag{D.2}$$

$$d\,(< \sigma\, v >) = f(\mathbf{v}_1)\, \sigma_{12}\, |\mathbf{v}_1 - \mathbf{v}_2|\, f(\mathbf{v}_2)\, d^3\mathbf{v}_1\, d^3\mathbf{v}_2 \tag{D.3}$$

Where $f(\mathbf{v}_1)$ and $f(\mathbf{v}_2)$, n_1 and n_2, $\mathbf{v}_1$ and $\mathbf{v}_2$ are the Maxwellian distribu-

tions, number densities and the speeds of particle species 1 and 2, respectively. The σ_{12} is the cross-section of 1+2 reaction.

As it is commonly used to arrive at the rate formula eq. (2.1), one changes the variables. Instead of $\mathbf{v}_1$ and $\mathbf{v}_2$ the$\mathbf{V}_1$ and $\mathbf{u}_2$ are used, which define the center-of-mass speed and collision speed respectively:

$$(m_1 + m_2)\mathbf{V} = m_1\mathbf{v}_1 + m_2\mathbf{v}_2 \tag{D.4}$$

$$\mathbf{u} = \mathbf{v}_1 - \mathbf{v}_2 \tag{D.5}$$

The Jacobian of this transformation is one, thus by transforming the variables we obtain:

$$\mathbf{v}_1 = \mathbf{V} + \frac{m_2}{m_1 + m_2}\mathbf{u} \tag{D.6}$$

$$\mathbf{v}_2 = \mathbf{V} - \frac{m_1}{m_1 + m_2}\mathbf{u} \tag{D.7}$$

$$d^3\mathbf{v}_1\, d^3\mathbf{v}_2 \equiv d^3\mathbf{V}\, d^3\mathbf{u} \tag{D.8}$$

If we replace the distribution with Maxwellian distribution and transform the variables; moreover, if we call μ the reduced mass of the interacting system 1+2, the $E = \mu\, u^2/2$ the collision energy (or CM-frame energy) and if $d^3\mathbf{u} = 4\pi u^2\, d\, u$, then we obtain:

$$d\,(<\sigma\, v>) = \frac{(m_1 m_2)^{3/2}}{\pi^2\mu^2(k_B T)^3}\left\{\sigma(E)\, E \exp\left(-\frac{E}{k_B T}\right) d\, E\right\}\times \\ \times\left\{\exp\left(-\frac{(m_1 + m_2)\mathbf{V}^2}{2k_B T}\right) d^3\mathbf{V}\right\} \tag{D.9}$$

As we see, the differential rate $d\,(<\sigma\, v>)$ depends on the collision energy E and the velocity $\mathbf{V}$ (or the center-of-mass motion). By integrating the eq. (D.9) with respect to the CM-velocity $\mathbf{V}$ we get $[2\pi k_B T/(m_1 + m_2)]^{3/2}$, then by integrating through the energy E, we obtain the well know formula we wrote in the eq. (2.1).

From the kinematics of the reaction $1 + 2 \rightarrow 3 + \gamma$ also by neglecting the recoil of nuclei 3 (i.e. $E_\gamma^{cm} \ll m_3\, c^2$), the γ-ray energy in the center-of-mass system is given by:

$$E_\gamma^{cm} = E + Q \tag{D.10}$$

where $Q = (m_1 + m_2 - m_3)\, c^2$ is the Q-value of the reaction. By changing the variables from collision energy E to the CM-frame γ-ray energy E_γ^{cm} we then obtain the CM-frame $d < \sigma\, v > /dE_\gamma^{cm}$ (or CM-frame emissivity $d\,\epsilon_\gamma/dE_\gamma^{cm}$ as it is described in eq. (D.1))

For a LAB-frame observer, the center-of-mass (CM-frame) of the two colliding particles 1 and 2 is moving with velocity $\mathbf{V}$; therefore the γ-rays that are emitted in CM-frame of the 3 and γ system, will be Doppler-broadened to

the LAB-frame observer. Let the line of sight be for instance the z-direction. Every photon observed in the z-direction will be Doppler-broadened and it is related with the V_z component in accordance to:

$$\frac{m_3}{m_1+m_2}\left(1-\frac{E_\gamma^{cm}}{E_\gamma}\right)=\frac{m_3}{m_1+m_2}\left(1-\frac{E+Q}{E_\gamma}\right)=\frac{V_z}{c}=\beta \tag{D.11}$$

$$\frac{m_3}{m_1+m_2}\,\frac{E+Q}{E_\gamma^2}\,dE_\gamma=d\beta \tag{D.12}$$

Note that this equation is calculated for a fixed collision energy E.

By substituting eq. (D.11) to eq. (D.9) and integrate over V_x and V_y degrees of freedom – they play no role to broadening the z-direction photons – then we obtain:

$$\begin{aligned} d\,(<\sigma\,v>) = c\,\sqrt{\frac{8}{\pi\mu(k_BT)^3}\left(\frac{m_1+m_2}{2\pi k_BT}\right)}\left\{\sigma(E)\,E\,\exp\left(-\frac{E}{k_BT}\right)dE\right\}\times \\ \times\left\{\exp\left(-\frac{m_3^2c^2}{(m_1+m_2)2k_BT}\left(1-\frac{E+Q}{E_\gamma}\right)^2\right)\frac{m_3}{m_1+m_2}\,\frac{E+Q}{E_\gamma^2}\,dE_\gamma\right\} \end{aligned} \tag{D.13}$$

Therefore, the rate to emit a photon with energy E_γ in the LAB-frame per unit energy interval is given by:

$$\frac{d<\sigma\,v>}{dE_\gamma}(E_\gamma)=\left(\frac{2\,m_3\,c}{\pi\,(m_1m_2)^{1/2}\,(k_BT)^2}\right)\times\mathcal{I}(E_\gamma,T) \tag{D.14}$$

where we have denoted with $\mathcal{I}(E_\gamma)$ the integral

$$\mathcal{I}(E_\gamma,T)=\int dE\,\frac{E\,(E+Q)\,\sigma(E)}{E_\gamma^2}\exp\left(-\frac{m_3^2c^2}{2(m_1+m_2)k_BT}\left(1-\frac{E+Q}{E_\gamma}\right)^2-\frac{E}{k_BT}\right) \tag{D.15}$$

Hence the emissivity in the LAB-frame is:

$$\Phi(E_\gamma,T)=\frac{d\,\epsilon_\gamma}{dE_\gamma}=n_1\,n_2\times\left(\frac{2\,m_3\,c}{\pi\,(m_1m_2)^{1/2}\,(k_BT)^2}\right)E_\gamma\times\mathcal{I}(E_\gamma,T) \tag{D.16}$$

E

Cross sections and reaction rates for some typical nuclei

E.1 Total nonelastic and inelastic cross sections with their corresponding rates

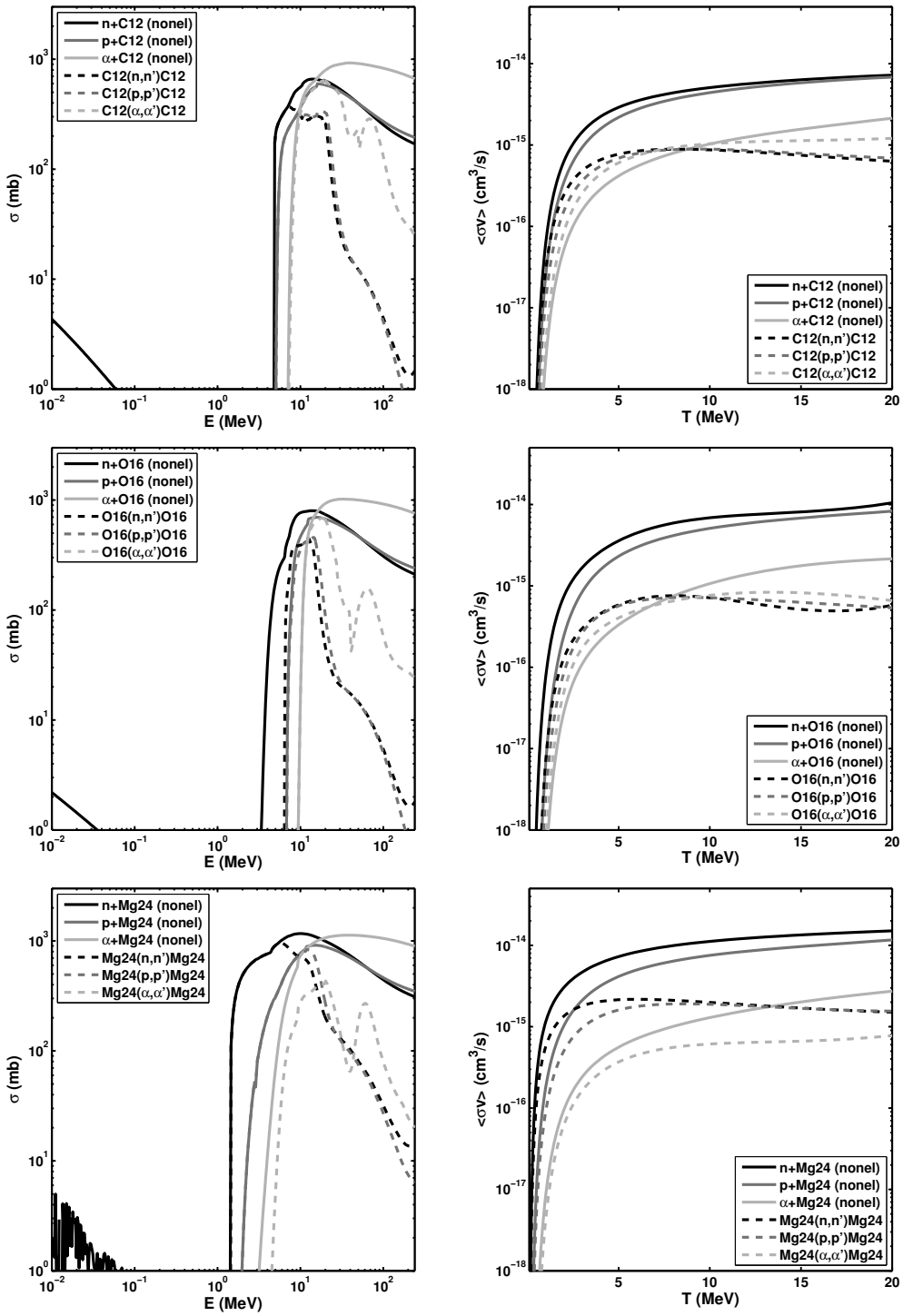

Figure E.1: Nonelastic and inelastic cross-sections and the respective Maxwellian average rates for three projectiles n, p and α-particle and for the ^{12}C, ^{16}O, ^{24}Mg nuclei.

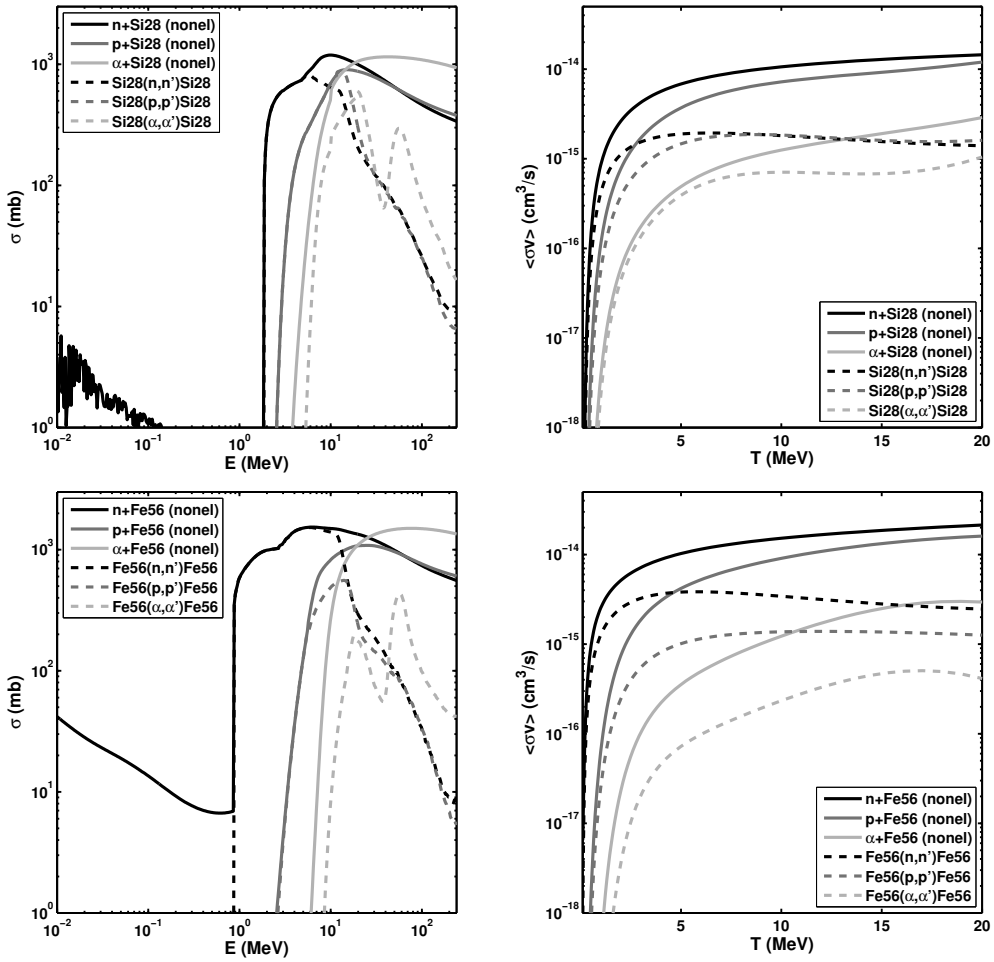

Figure E.2: Nonelastic and inelastic cross-sections and the respective Maxwellian average rates for three projectiles n, p and α-particle and for the ^{28}Si, ^{56}Fe nuclei.

E.2 Production of γ-ray lines for some elements

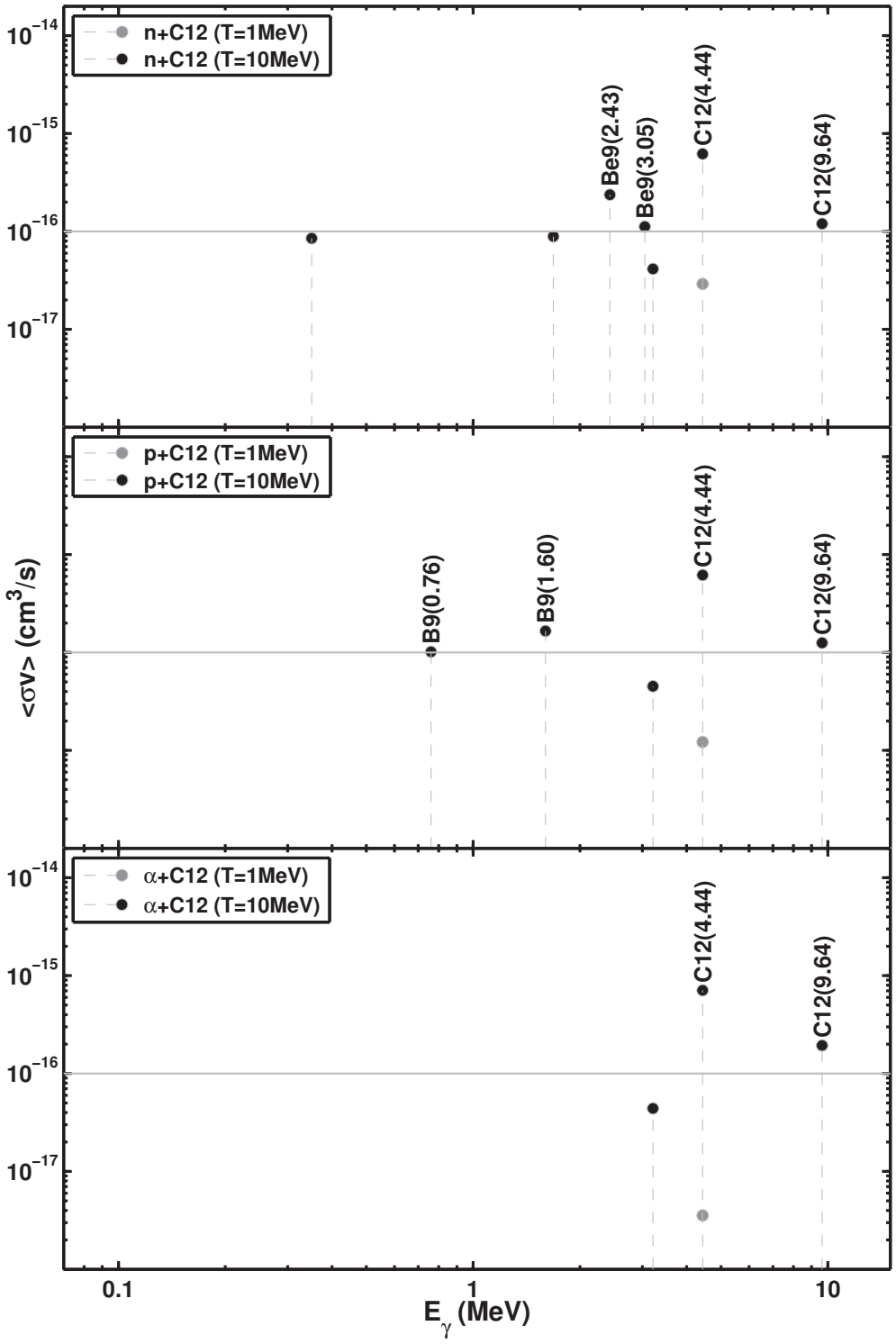

Figure E.3: The Maxwellian average rates for temperature $k_BT = 1$ and 10 MeV, for the most important γ-ray lines of ^{12}C interaction with n, p and α-particles.

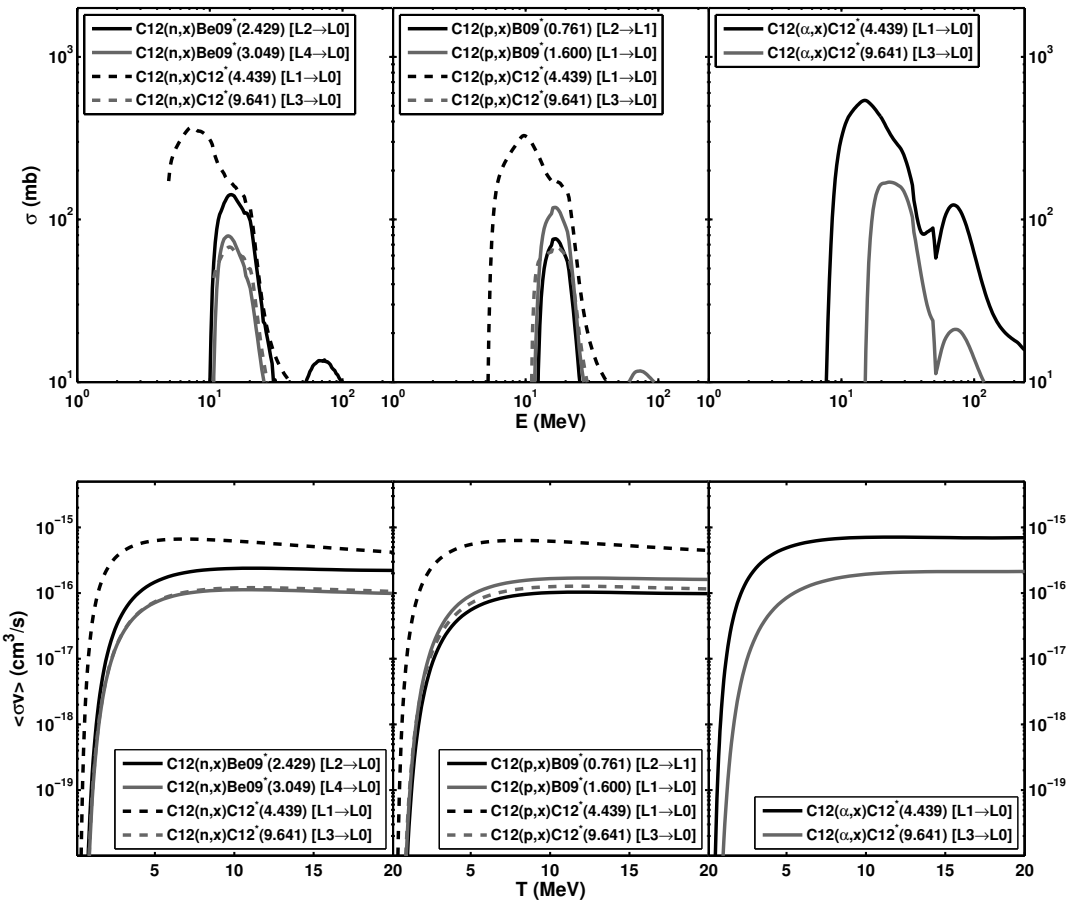

Figure E.4: The cross section for the most important γ-ray lines of ^{12}C interaction with n, p and α-particles.

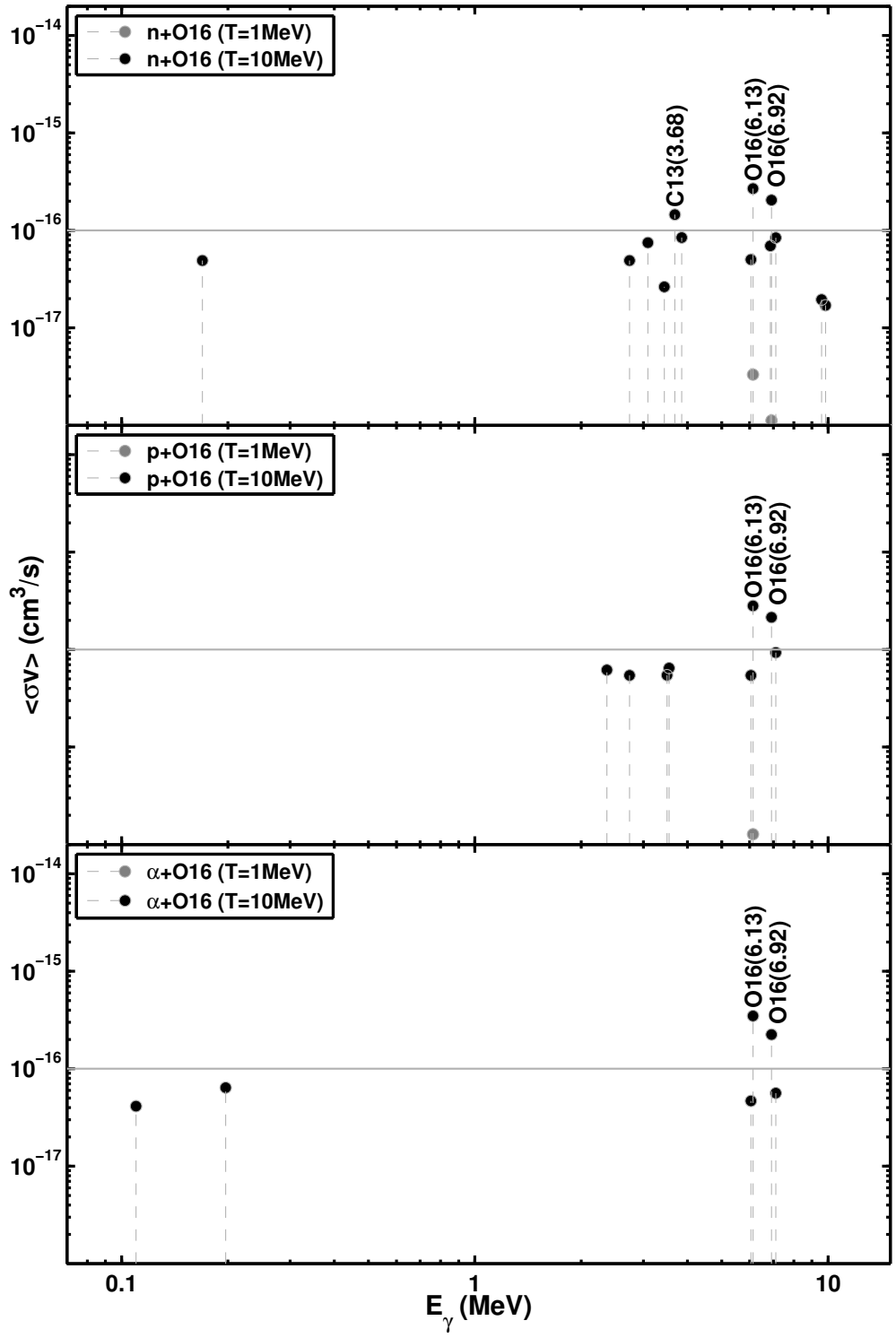

Figure E.5: The Maxwellian average rates for temperature k_BT = 1 and 10 MeV, for the most important γ-ray lines of ^{16}O interaction with n, p and α-particles.

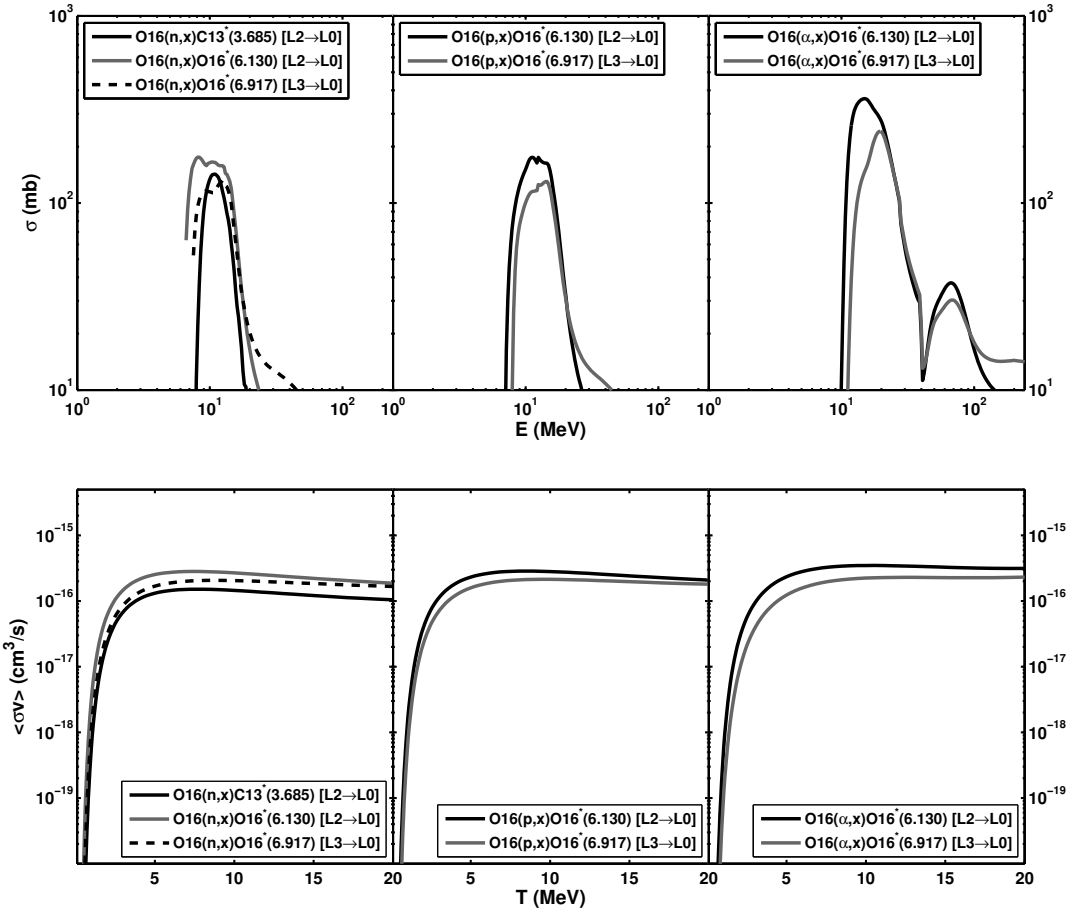

Figure E.6: The cross sections for the most important γ-ray lines of ^{16}O interaction with n, p and α-particles.

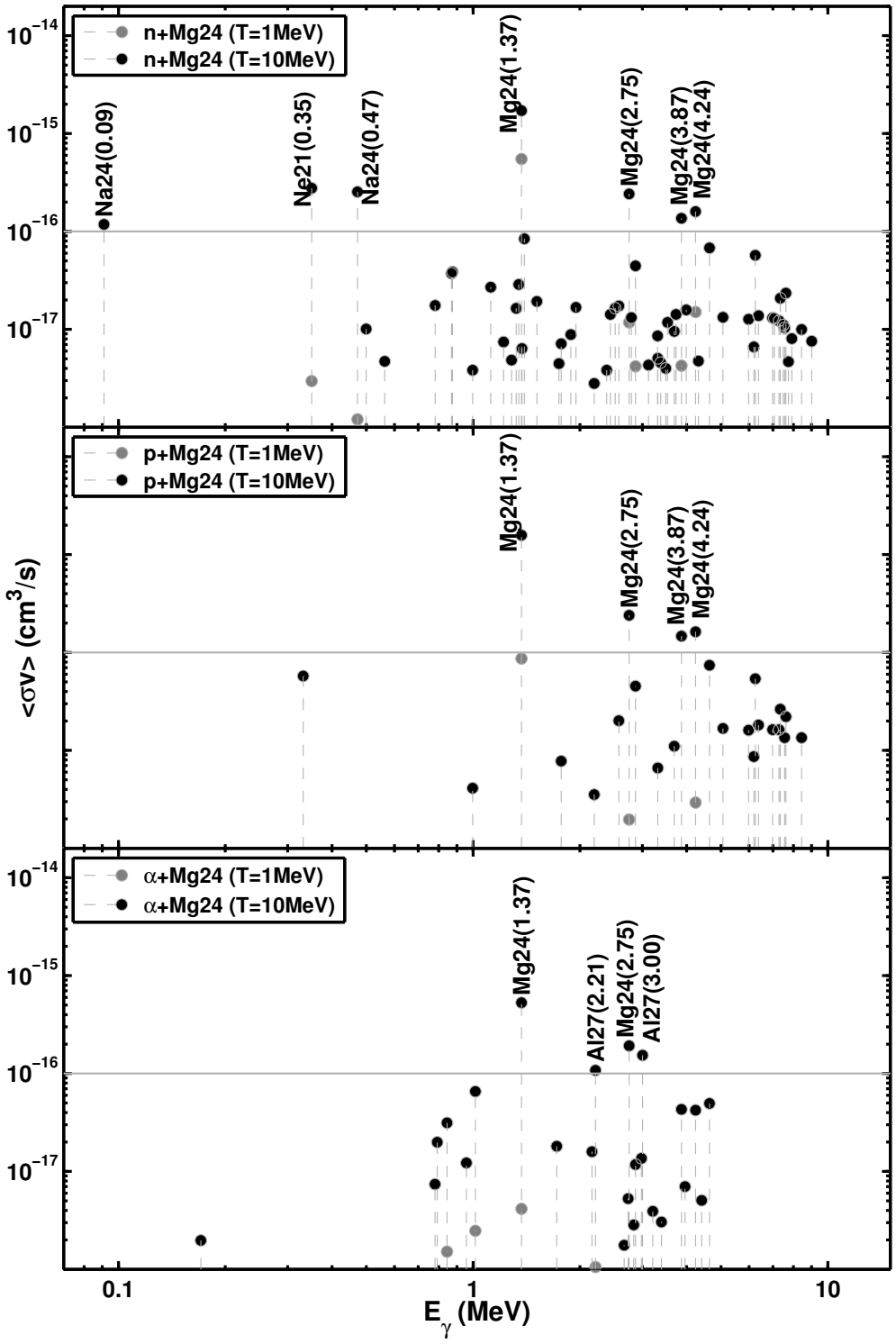

Figure E.7: The Maxwellian average rates for temperature k_BT = 1 and 10 MeV, for the most important γ-ray lines of ^{24}Mg interaction with n, p and α-particles.

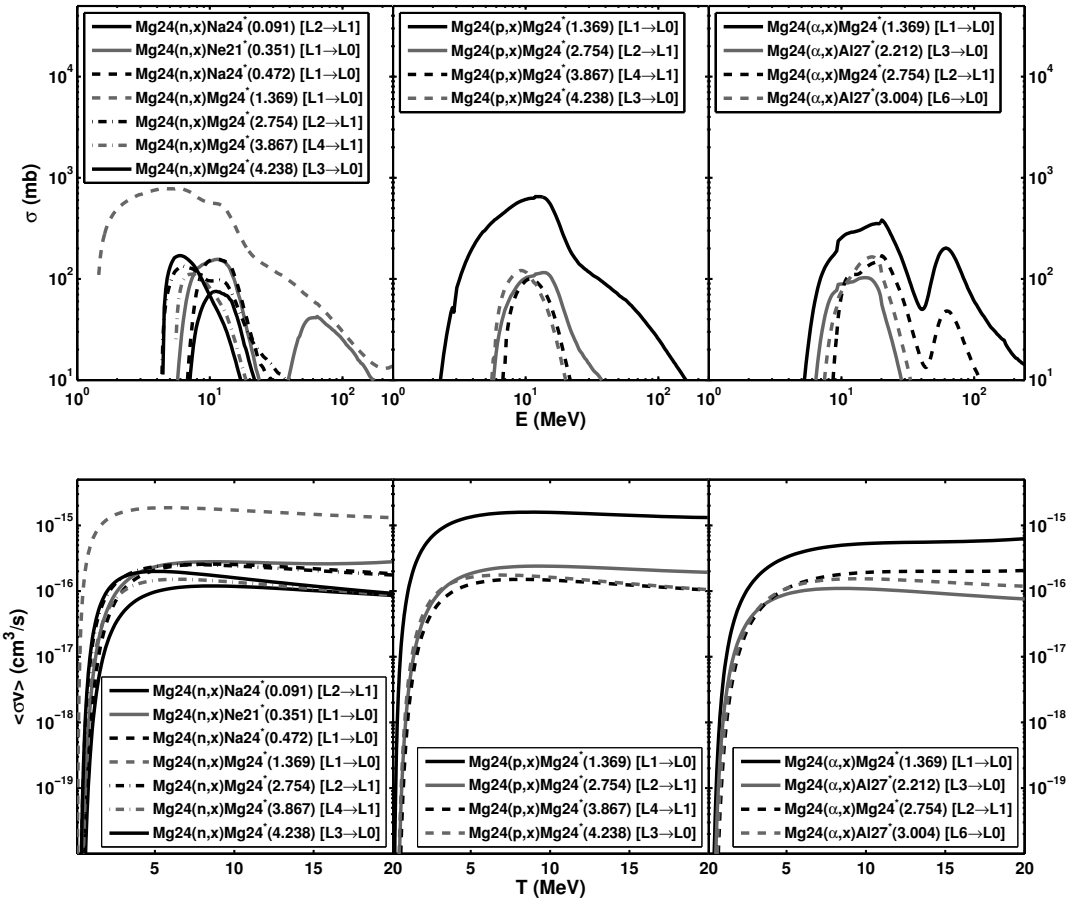

Figure E.8: The cross sections for the most important γ-ray lines of ^{24}Mg interaction with n, p and α-particles.

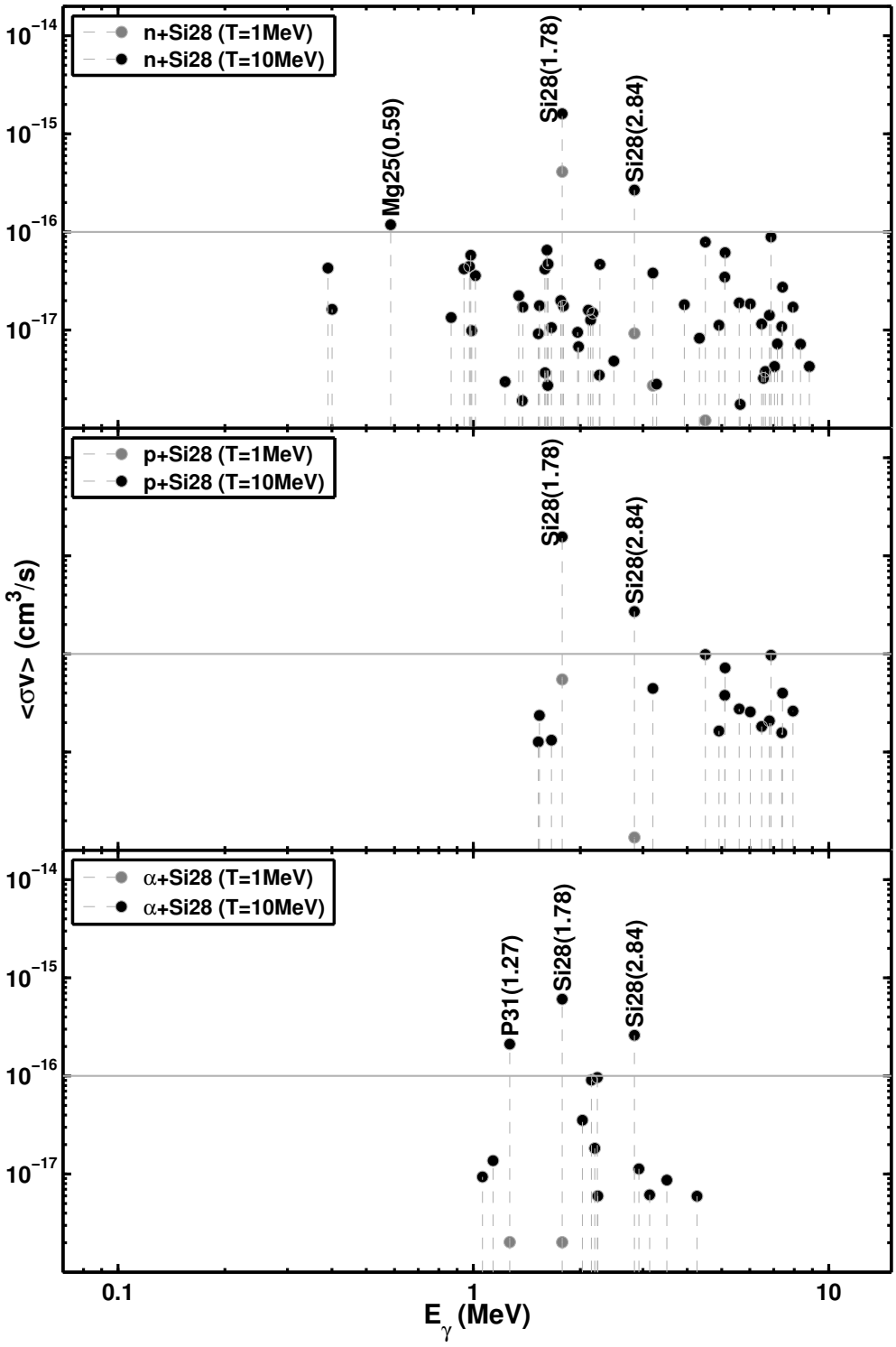

Figure E.9: The Maxwellian average rates for temperature k_BT = 1 and 10 MeV, for the most important γ-ray lines of ^{28}Si interaction with n, p and α-particles.

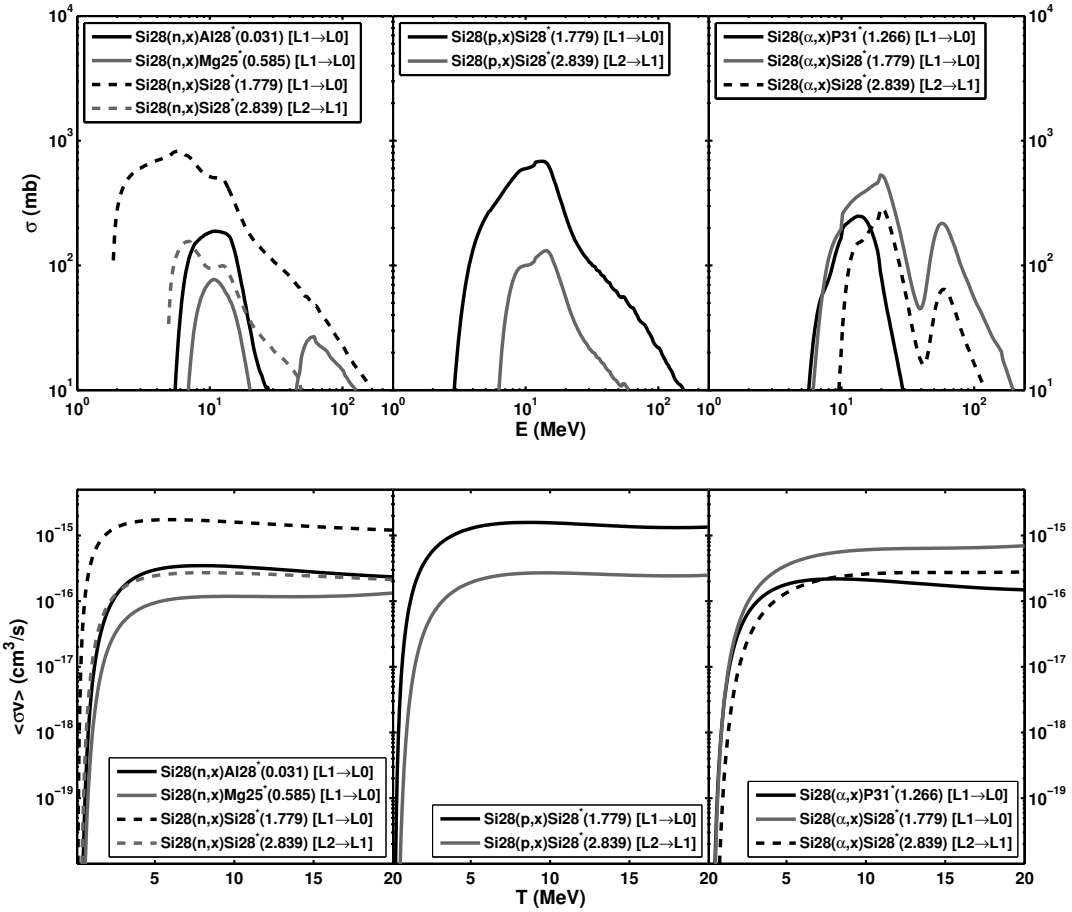

Figure E.10: The cross sections for the most important γ-ray lines of ^{28}Si interaction with n, p and α-particles.

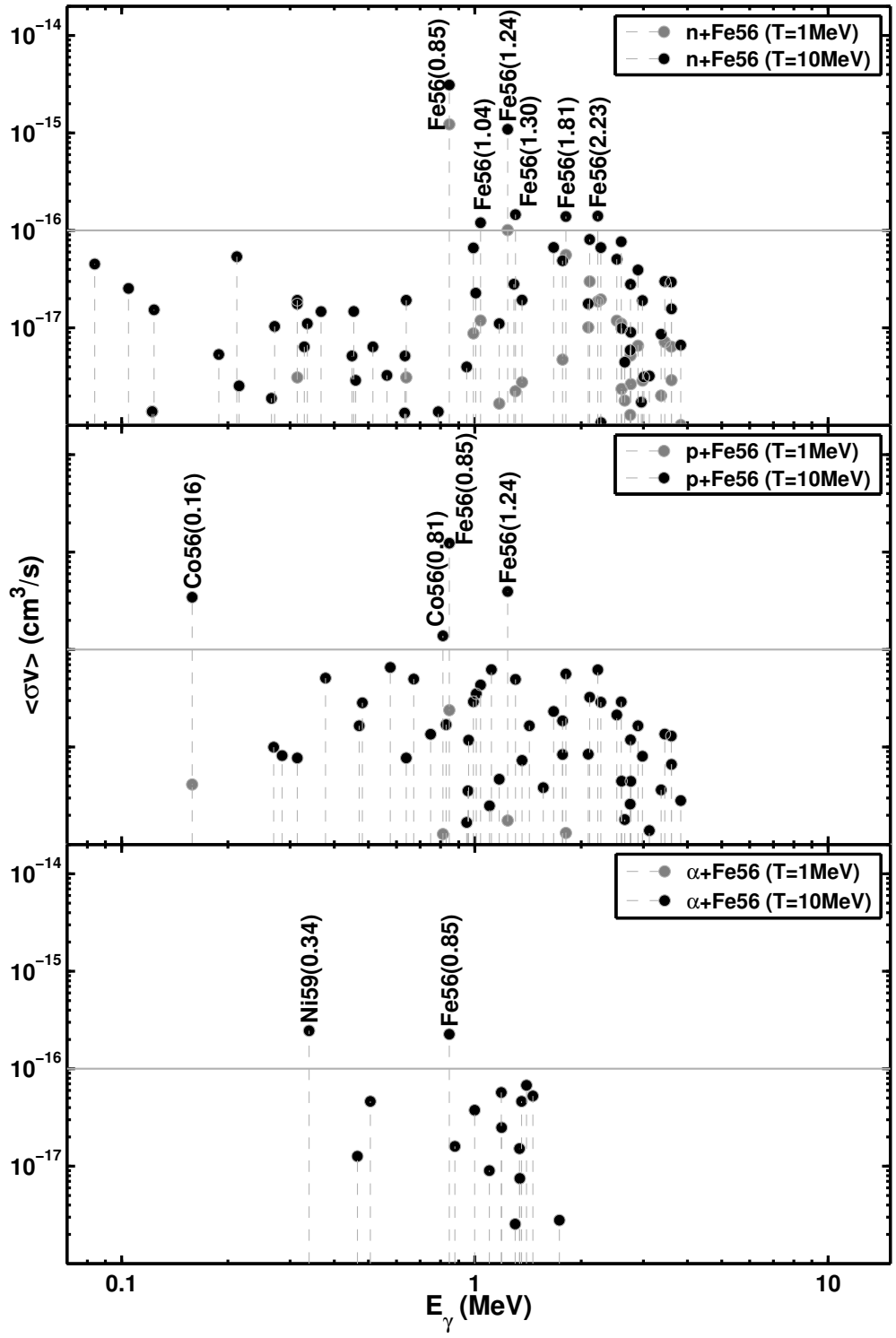

Figure E.11: The Maxwellian average rates for temperature $k_BT = 1$ and 10 MeV, for the most important γ-ray lines of ^{56}Fe interaction with n, p and α-particles.

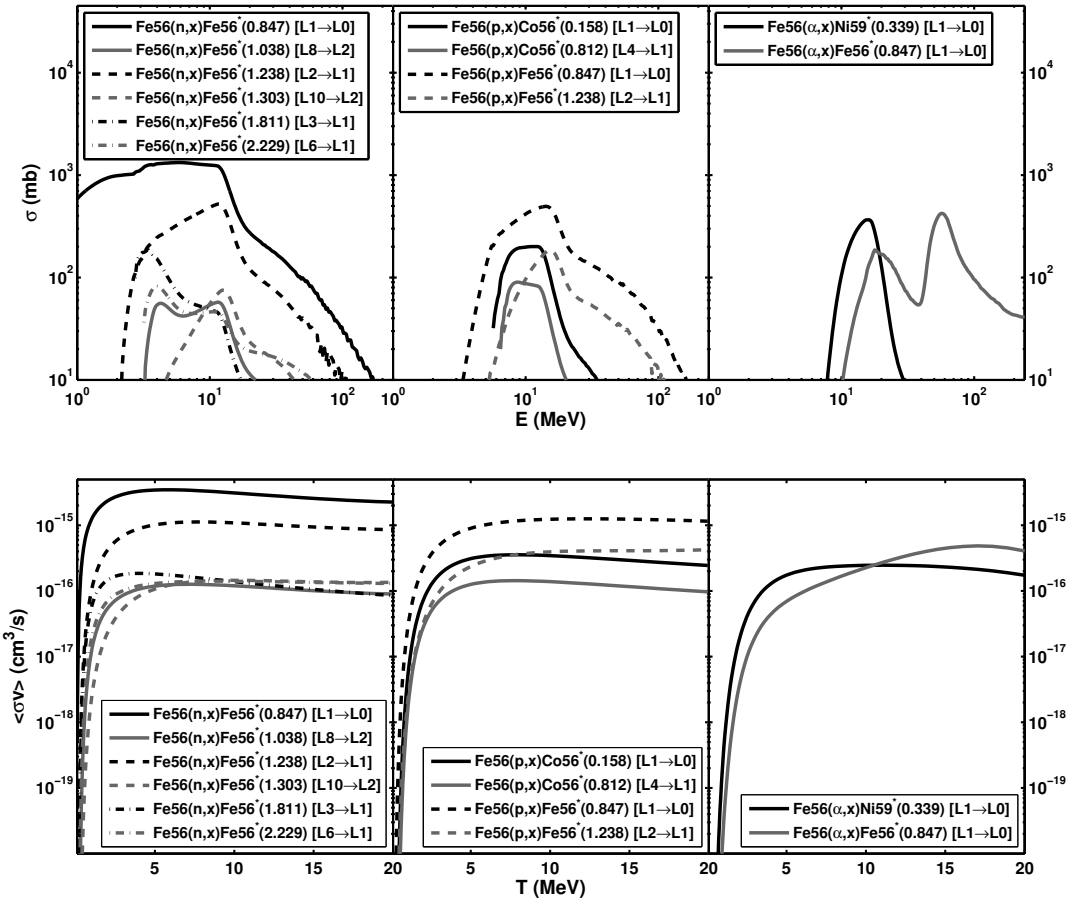

Figure E.12: The cross sections for the most important γ-ray lines of ^{56}Fe interaction with n, p and α-particles.

Acknowledgements

It would not have been possible to finish this doctoral thesis without the help and support of the kind people around me, to only some of whom it is possible to give particular mention here.

This thesis would not have been possible without the help, support, patience and exciting ideas of my supervisor, Prof. Felix Aharonian. Dear Felix, it was great working with you. Thank you for your patience and your help.

I would like to thank Prof. Stefan Wagner for accepting to be my second thesis referee, and I would also like to thank Prof. Karlheinz Meier and Prof. Andreas Quirrenbach for accepting to be my thesis examiners.

I am grateful to Maxim Barkov, Frank Rieger and Gabi Weese that have been always helpful and very friendly to me.

Warm thanks to all my friends and colleagues from the Institute. Especially, Eva, Iwona, Anton, Dave, Mytia, Meiert, Ellen, Giovanni.

Above all I thank my mother for her unequivocal support for which my mere expression of thanks does not suffice.